Tampere University

Santeri Saariokari

CALIBRATION OF LUMINOMETERS AT COMPACT MUON SOLENOID EXPERIMENT

Master's Thesis
Faculty of Engineering and Natural Sciences
Examiners: Res. Asst. Prof. Francesco Romeo
Prof. Esa Räsänen
August 2022

ABSTRACT

Santeri Saariokari: Calibration of luminometers at Compact Muon Solenoid experiment
Master's Thesis
Tampere University
Science and Engineering
August 2022

Measuring luminosity, a quantity related to the amount of collected data, is essential in high energy physics experiments. It is used in measuring the absolute cross section of physical processes and in searches for new physics. In order to achieve precise results at the Large Hadron Collider (LHC) at the European Organisation for Nuclear Research (CERN), luminosity must be measured with high precision, which motivates studies to minimise all systematic effects that dominate the uncertainty of this measurement. The state-of-the-art studies are carried out using luminometers, which record a fraction of the number of collisions taking place at the LHC experiments. The rate recorded by these devices has to be normalised through a factor given by the visible cross section σ_{vis}, to provide an estimate for the absolute luminosity. The Compact Muon Solenoid experiment (CMS) contains several luminometers capable of producing a real-time estimate of luminosity per colliding particle bunch. Three luminometers have been considered in this work: the Fast Beam Condition Monitor (BCM1F), the Pixel Luminosity Telescope (PLT), and the Forward Hadron Calorimeter (HF). The BCM1F and PLT detectors are operated entirely by the BRIL group, which also provides the software used to derive the calibration of the rates for the luminosity measurement.

The established calibration method used at LHC requires a specific scanning procedure, where the two particle beams are moved over each other producing a way to determine the beam overlap width, which in turn can be used to estimate σ_{vis} of a luminometer. This scanning procedure is called a van der Meer scan. The methods used to measure this calibration factor and the luminosity during the commissioning period for Run 3 are discussed.

The software used for analysing van der Meer scans is called the vdM framework. It is capable of rapidly estimating the σ_{vis} after a vdM scan is performed, and also applying a set of sophisticated corrections in the offline analysis to mitigate systematic effects and minimise the total uncertainty of the measurement. It has been updated throughout the long shutdown 2, a maintenance period between Run 2 (years 2015 – 2018) and Run 3 (from 2022 on) data taking periods. The most recent updates that have been implemented as a part of this thesis are described in detail and an overview of the current features of the program are presented. Recent improvements include establishing an automated testing procedure, automated figures, and a centralised versioning & documentation system implemented in GitLab. These new features upgrade the software tool to render it faster and simple to use.

A case study to correct for a source of inaccuracy of the σ_{vis} measurement caused by time evolution of the beam overlap of colliding particle beams is considered. The data collected during the fill 6868 from Run 2 is studied, and it is found that the convoluted beam widths as well as the peak detector rate evolve in a linear fashion over time. This finding suggests that a multiplicative factor should be applied, in order to correct the effect of this phenomenon. The impact of this factor has been found to vary between 0.0 to 0.2% in fill 6868, and has to be taken into account considering the luminosity measurement aims to achieve an inaccuracy of no more than 2%.

Keywords: CERN, Compact Muon Solenoid, CMS, luminosity, van der Meer

TIIVISTELMÄ

Santeri Saariokari: Luminometrien kalibrointi Compact Muon Solenoid -kokeessa
Diplomityö
Tampereen yliopisto
Teknis-luonnontieteellinen DI-ohjelma
Elokuu 2022

Luminositeetin, tuotetun datan määrään liittyvän suureen, mittaaminen on välttämätöntä korkeaenergisen fysiikan kokeissa. Absoluuttista luminositeettia voidaan käyttää fysikaalisten prosessien absoluuttisen poikkipinta-alan mittaamiseen sekä uuden fysiikan tutkimuksiin. Tarkkojen tulosten saamiseksi Large Hadron Collider (LHC) -hiukkaskiihdyttimen kokeissa Euroopan hiukkasfysiikan tutkimuskeskuksessa (CERN), luminositeetti tulee mitata suurella tarkkuudella. Tämä luo vahvan motivaation tutkimuksille, jotka minimoivat luminositeetin mittaamisen virhelähteet. Tarkimmat mittaukset suoritetaan luminometreillä, jotka tallentavat vakio-osan LHC:n kokeissa tapahtuvien törmäysten lukumäärästä. Luminometrien lukema törmäyksille tulee normalisoida asettamalla niille laitekohtainen normalisointikerroin, efektiivinen poikkipinta-ala σ_{vis}, jonka avulla lukema voidaan muuntaa absoluuttiseksi luminositeetiksi. Compact Muon Solenoid (CMS) -kokeessa on kolme luminometriä, jotka pystyvät tuottamaan reaaliaikaisen lukeman yksittäisen hiukkaskimpun luminositeetista. Nämä ovat Fast Beam Condition Monitor (BCM1F), Pixel Luminosity Telescope (PLT) ja Forward Hadron Calorimeter (HF). BCM1F- ja PLT-ilmaisimet on suunnitellut ja rakentanut BRIL-ryhmä, joka myös ylläpitää luminositeettimittausten analysointiin käytettävää ohjelmistoa.

Kalibrointimenetelmä, jota käytetään LHC-hiukkaskiihdyttimen kokeissa sisältää prosessin, jossa hiukkassäteet siirretään toistensa yli, jolloin luminometerien lukemasta voidaan määrittää hiukkassäteiden päällekkäisyyden leveys. Leveyksien avulla voidaan määrittää luminometrikohtainen σ_{vis}. Tätä menettelyä kutsutaan van der Meer -skannaukseksi. BRIL-projektin luminometrien σ_{vis} sekä luminositeetin määrittäminen esitellään käyttäen mittauksia Run 3:n käyttöönottokaudelta.

Van der Meer -skannausten analysointiin käytetään ohjelmistotyökalua nimeltä vdM framework. Sen avulla luminometrien normeerauskerroin pystytään määrittämään nopeasti vdM-skannauksen jälkeen, ja se tarjoaa myös mahdollisuuden korjata skannauksessa esiintyviä systemaattisia epätarkkuuksia osana jälkianalyysiä, vähentäen mittauksessa esiintyvää systemaattista epävarmuutta. Kyseistä ohjelmistoa on parannettu ylläpitoajanjaksolla long shutdown 2, datankeruuperiodien Run 2 (2015 – 2018) ja Run 3 (2022 – 2025) välissä. Viimeisimmät päivitykset esitellään yksityiskohtaisesti, ja katsaus ohjelman nykyisistä ominaisuuksista on esitetty yleisellä tasolla. Viimeaikaisiin parannuksiin kuuluu automatisoidun testausketjun käyttöönotto, sekä keskitetty versiointi- ja dokumentointijärjestelmä, joka on toteutettu GitLab-ympäristössä. Näiden parannusten tavoitteena on parantaa kyseisen työkalun nopeutta sekä helppokäyttöisyyttä.

Lopuksi tutkitaan systemaattista virhettä luminometrien σ_{vis} määrittämisessä, joka aiheutuu hiukkassäteiden päällekkäisyyden aikariippuvuudesta. Tutkimus suoritetaan käyttäen Run 2:n täyttöperiodia 6868, josta havaitaan sekä hiukkassäteiden päällekkäisyyksien leveyksien, että huippujen muuttuvan lineaarisesti ajan myötä. Havainto viittaa mahdollisuuteen korjata normeerauskerroin kertoimella, joka määritetään sovitteista ajan funktiona muuttuviin parametreihin. Kertoimen vaikutus täyttöperiodille 6868 on suuruudeltaan 0.0 – 0,2 %, ja se tulee ottaa huomioon mittauksessa, jonka tavoitteena on saavuttaa alle 2% epätarkkuus.

Avainsanat: CERN, Compact Muon Solenoid, CMS, luminositeetti, van der Meer

PREFACE

I would like to thank everyone involved

in Geneva, 4th August 2022

Santeri Saariokari

CONTENTS

1. Introduction 1
1.1 Large Hadron Collider 2
1.1.1 CERN accelerator complex and particle beams 2
1.2 Compact Muon Solenoid 5
1.3 Detectors used for luminosity measurements at CMS 7
1.3.1 Pixel Luminosity Telescope 8
1.3.2 Fast Beam Condition Monitor 9
1.3.3 Hadronic Calorimeter 11
1.3.4 Other systems used for luminosity measurement at CMS 11
2. Measurement of luminosity 13
2.1 Concept of luminosity 13
2.2 Luminosity at particle accelerator experiments 14
2.3 Calibration of luminometers 16
2.4 Van der Meer scan methodology 17
2.5 Zero counting method 19
2.6 Luminosity corrections 19
2.6.1 Peak correction 20
2.6.2 Background correction 22
2.6.3 Beam-Beam deflection 23
2.6.4 Dynamic-beta correction 25
2.6.5 Orbit drift correction 27
2.6.6 Length scale correction 27
2.6.7 Beam current calibration and ghost & satellite correction 27
3. VdM framework 29
3.1 Software used for the analysis of vdM scans 29
3.1.1 Structure of the program 29
3.1.2 Improvements for Run 3 30
3.1.3 Gitlab pipeline 40
3.2 BRIL data acquisition system 43
3.3 BRIL data aggregation system 45
4. Luminosity measurement using October 2021 beam test data 49
4.1 The vdM scans 49

4.2 Measurement of visible cross-section for luminosity calibration 50
4.3 PLT channel timing 53
4.4 BCM1F µTCA commissioning 57
4.5 Beam test conclusions. 58
5. Time evolution of convoluted beam width 59
5.1 VdM scans used for studying convoluted beam width effect 59
5.2 Methods to evaluate the effect 59
5.3 Results 62
6. Conclusions 65
References 67
Appendix A: October 2021 beam test results 72
Appendix B: Fits to convoluted beam width and peak over time 76
Appendix C: Effect of convoluted beam width time evolution to visible cross section,
no framework corrections 88

LIST OF FIGURES

1.1 Operation schedule for the Large Hadron Collider, last updated in January 2022 with Long Shutdown 3 to start at the end of 2025 and last throughout 2028. Figure adapted from Ref. [1]. 1

1.2 CERN accelerator complex, highlighting the large number of interconnected systems. The four large experiments are marked with yellow dots. Proton path to the Large Hadron Collider can be traced along marks LINAC4, BOOSTER, PS, SPS, LHC . Figure from Ref. [6]. 3

1.3 Particle bunch occupying an RF bucket while being accelerated by electrical field in an RF cavity. 4

1.4 Schematic picture of the Compact Muon Solenoid detector displaying it's cylindrically symmetric layers. The beam pipe is visible passing through the centre of the detector. Figure adapted from Ref. [9]. 5

1.5 Illustration of the elementary particles interacting in the Compact Muon Solenoid subdetector and how they are detected. Figure adapted from [10]. 6

1.6 Systems operated by BRIL group at the Compact Muon Solenoid experiment. Green text indicates, that the instrumentation has been rebuilt for Run 3. 7

1.7 **Left**: Schematic image of the Pixel Luminosity Telescope (PLT) showing eight sets of three pixel detectors forming eight *telescopes*. Figure from Ref. [15]. **Right**: Photo of four PLT telescopes ordered to a *quadrant* with mounting support and connections to the readout electronic visible. Figure from Ref. [17]. 8

1.8 Three planes of a PLT telescope, displaying the formation of a triple coincidence. Figure from Ref. [18]. 9

1.9 Fast Beam Condition Monitor front-end electronics with installed ASICs, golden coloured mounting points visible. Figure from Ref. [21]. 10

2.1 Particle flux through a cylinder. 14

2.2 Two particle beams colliding. 15

2.3 Nominal LHC beam positions displaying the van der Meer scan sequence first in x- and then in y-axis. 18

2.4 Detector hit rates of a normal van der Meer (red lines) and an offset scan (blue lines) as functions of beam separation in x and y directions, highlighting the difference between the nature of the two scan types. Figure from Ref [32]. 20
2.5 Illustration of measured detector hit rates during a van der Meer scan performed along μ_2. 21
2.6 Magnitudes of corrections for electromagnetic repulsion of the beams, calculated using nominal beam separations from a scan in fill 4954. **Left:** Beam-beam deflection calculated using Bassetti-Erskine formula. **Right:** Correction for dynamic-β effect. Figures from Ref. [26]. 26
2.7 Longitudinal profile of the LHC beam measured with Longitudinal Density Monitor (LDM), displaying the nominally filled bucket (middle), satellite charges close to the centre and ghost charges further out. Figure from Ref. [38]. 28

3.1 Single Gaussian fit to detector hit rates normalised by the product of beam currents, with values of fit parameters visible in top right. **Left:** Pixel Luminosity Telescope, with added indications of fit parameters, **Right:** Fast Beam Condition Monitor. 31
3.2 Structure of the vdM framework with some innermost sub-folders with self-explanatory names left out for clarity. 33
3.3 Ratio plots of quantities between x and y directions, including the average (Avg.), standard error of the mean (SEM) and the number of colliding bunches (NBCID). **Top**: Peak of fit. **Bottom**: Head-on rate. 35
3.4 **Top**: Distribution of reduced χ^2 values (χ^2 divided by the numbers of degree of freedom) of fits including theoretical distribution individually for each detector. **Bottom**: Combined χ^2 values of all detectors. The title includes the set of corrections and fit function written using shorthand notation. . . . 36
3.5 **Top**: Ratio of beam current measured with FBCT and summed over all bunches, and beam current measured with DCCT. **Bottom**: Calculated magnitude of correction for beam-beam deflection, is the corresponding correction is enabled. The target BCID is visible in the title along scan axis. 37
3.6 An estimation of detector visible cross section done by fitting a plane to $\mathrm{peak} - \Sigma_x - \Sigma_y$ triplets. 38
3.7 GitLab pipeline of the vdM framework. 41
3.8 Relations of systems essential to BRILDAS. 45

4.1 Time difference between beams recorded by the Beam Pickup Transformer during cogging adjustment, viewed from the BRIL web monitor. Value of -0.99 is displayed when no beam is present. 50
4.2 Initial values for the visible cross section of the Fast Beam Condition Monitor. 52
4.3 Initial values for the visible cross section of the Pixel Luminosity Telescope. 53
4.4 Fraction of hits detected by the Pixel Luminosity Telescope that are produced by colliding and non-colliding filled bunches (R_{f}). 54
4.5 Channel offsets of the Pixel Luminosity Telescope. Channels with a misalignment of least one full BCID are coloured red. 55
4.6 Fraction of hits detected by the Pixel Luminosity Telescope that are caused by colliding and non-colliding filled bunches (R_{f}) after correcting channel alignments using algorithm 4.1. 56
4.7 Visible cross section of the Pixel Luminosity Telescope, after correcting for timing misalignment by multiplying the hit rates by the ratio between corrected and uncorrected values of rate in colliding bunches. 57
4.8 Comparison of the visible cross section of the Fast Beam Condition Monitor, calculated with data from different backend systems. *BCM1F* stands for the RHU readout system and *BCM1FUTCA* the μTCA readout. 58

5.1 Time evolution of convoluted beam width including linear fits, determined from rates measured using the Forward Hadron Calorimeter utilising the transverse energy algorithm (HFET). 61
5.2 Time evolution of fit peak including linear fits, determined from rates measured using the Forward Hadron Calorimeter utilising the transverse energy algorithm. 62

A.1 Single bunch instantaneous luminosity (SBIL) for the Fast Beam Condition Monitor (BCM1F) and Pixel Luminosity Telescope (PLT). 72
A.2 Convoluted beam width in x-axis. 73
A.3 Peak of fit for Pixel Luminosity Telescope (PLT). 74
A.4 Peak of fit for the Fast Beam Condition Monitor (BCM1F). 75

B.1 Time evolution of convoluted beam width including linear fits, HFET luminometer, all corrections applied. 76
B.2 Time evolution of convoluted beam width including linear fits, HFOC luminometer, all corrections applied. 77
B.3 Time evolution of convoluted beam width including linear fits, PLT luminometer, all corrections applied. 78

B.4 Time evolution of convoluted beam width including linear fits, HFET luminometer, no corrections applied. 79
B.5 Time evolution of convoluted beam width including linear fits, HFOC luminometer, no corrections applied 80
B.6 Time evolution of convoluted beam width including linear fits, PLT luminometer, no corrections applied. 81
B.7 Time evolution of peak including linear fits, HFET luminometer, all corrections applied. 82
B.8 Time evolution of peak including linear fits, HFOC luminometer, all corrections applied. 83
B.9 Time evolution of peak including linear fits, PLT luminometer, all corrections applied. 84
B.10 Time evolution of peak including linear fits, HFET luminometer, no corrections applied. 85
B.11 Time evolution of peak including linear fits, HFOC luminometer, no corrections applied. 86
B.12 Time evolution of peak including linear fits, PLT luminometer, no corrections applied. 87

LIST OF TABLES

3.1 Contents of `dip/acc/LHC/Beam/AutomaticScanIP5` relevant to vdM analysis and file creation. 44
3.2 Quantities available in the scan database. 46
3.3 Quantities available in "*Fill Summary*" tab of CMS OMS. 47

4.1 Scan conditions at the CMS experiment during October 2021 beam test. . 51

5.1 Visible cross section σ_{vis} determined using the vdM framework with all available corrections ("original") and its relative error $\Delta\sigma_{\mathrm{vis}}$ [%], visible cross section obtained by propagating the convoluted beam widths Σ to the mid point between planes ("corrected") and its relative error $\Delta\sigma_{\mathrm{vis}}$ [%], systematical uncertainty in visible cross section caused by peak and Σ evolution discrepancy $\Delta_{\mathrm{x/y}}$, and the difference between the corrected and uncorrected visible cross sections. 63

C.1 Visible cross section σ_{vis} determined using the vdM framework with no corrections ("original"), visible cross section obtained by propagating the convoluted beam widths Σ to the mid point between planes ("corrected"), systematical uncertainty in visible cross section caused by peak and Σ evolution discrepancy $\Delta_{\mathrm{x/y}}$, and the difference between the corrected and uncorrected visible cross sections. 88

LIST OF ACRONYMS

ASIC	Application-specific integrated circuit
ATLAS	A Toroidal LHC Apparatus
BCID	Bunch Crossing IDentifier
BCM1F	Fast Beam Condition Monitor
BPM	Beam Position Monitor
BPTX	Beam Pickup Transformer
BRIL	Beam Radiation, Instrumentation and Luminosity project
BRIL DAQ	BRIL Data Acquisition System
CERN	European Organisation for Nuclear Research (derived from French: *Conseil Européen pour la Recherche Nucléaire*)
CI/CD	Continous Integration / Continous Delivery
CMS	Compact Muon Solenoid
CMS OMS	CMS Online Monitoring System
CVD	Chemical vapor deposition
CVMFS	CERN Virtual Machine File System
DCCT	DC Current Transformers
DIP	Data Interchange Protocol
DT	Drift Tube
EOS	EOS Open Storage
FBCT	Fast Beam Current Transformers
HCAL	Hadronic calorimeter
HEP	High Energy Physics
HF	Forward Hadronic calorimeter
HFET	Hadronic Forward E_t
HFOC	Hadronic Forward Occupancy
IAM	Inducted Activity Monitor

IP	Interaction Point
LEIR	Low Energy Ion Ring
LEP	Large Electron–Positron Collider
LHC	The Large Hadron Collider
LHCb	LHC Beauty
MB	Muon Barrel
MicroTCA/µTCA	Micro Telecommunications Computing Architecture
PCC	Pixel Cluster Counting
PIP	Package Installer for Python
PLT	Pixel Luminosity Telescope
PS	Proton Synchrotron
PSB	Proton Synchrotron Booster
QGP	Quark-Gluon Plasma
RAMSES	Radiation Monitoring System for the Environment and Safety
RCMS	Run Control and Monitor System
REMUS	Radiation and Environment Monitoring Unified Supervision
SBIL	Single Bunch Instantaneous Luminosity
SM	The Standard Model
SPS	Super Proton Synchrotron
vdM	van der Meer, a beam scanning procedure named after it's inventor
VME	Versa Module Europa

LIST OF SYMBOLS

L	Integrated luminosity
$R(t)$	Number of particle hits as a function of time
R_f	Number of particle hits in nominally colliding bunches
Δ	Beam separation
Σ	Convoluted beam width
η	Pseudorapidity
$\mathcal{L}$	Instantaneous luminosity
σ	Cross section / beam width (context dependant)
σ_{vis}	Visible cross section
f_{LHC}	Revolution frequency of the LHC
c	Speed of light
h	Planck constant

1. INTRODUCTION

Particle physics studies the fundamental nature of particles that form our universe. Some of the most important instruments in particle physics are particle colliders that produce interactions between elementary particles. These interactions can be studied by using particle detectors to record the remnants of their interactions. The performance of particle accelerators relies to their collision energy and their ability to produce abundant interactions between particles to collect more data. The latter of these quantities is related to the so-called *luminosity*, defined as number of particles passing through a surface area per time unit. Having a particle accelerator with high luminosity is essential to be able to produce a statistically significant amount of data for physics searches and measurements, as the number of produced events is directly proportional to luminosity. For the same reason, measuring luminosity accurately is of utmost importance to achieve very precise results for the studied processes.

At the time of writing this thesis, CERN is preparing for the new data taking period called *Run 3*, which has started with a test period in late 2021, followed by a commissioning period and physics operation in 2022. Figure 1.1 shows the LHC schedule for Run 3, which was last updated in January 2022.

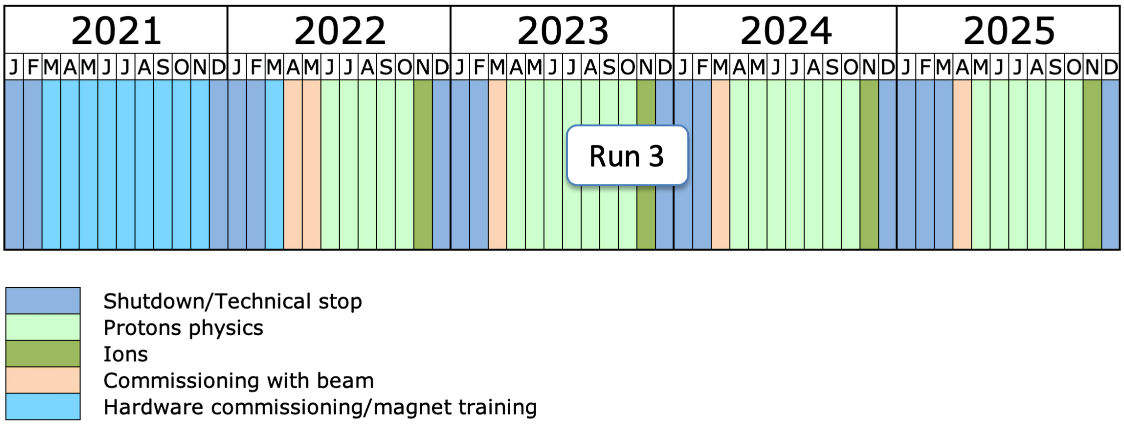

Figure 1.1. *Operation schedule for the Large Hadron Collider, last updated in January 2022 with Long Shutdown 3 to start at the end of 2025 and last throughout 2028. Figure adapted from Ref. [1].*

The shutdown period visible at the end of year 2025 marks the beginning of Long Shutdown 3 (LS3), and the same time the end of Run 3.

1.1 Large Hadron Collider

The Large Hadron Collider (LHC) is a particle accelerator operated by CERN, which stands for *Conseil Européen pour la Recherche Nucléaire*, or European Council for Nuclear Research. Its purpose is to accelerate two beams of protons or heavy ions travelling at relativistic velocities in opposite directions, one clockwise and one counter-clockwise, and to collide them at some of the four experiments located around the accelerator ring at an energy up to 14 TeV in the centre-of-mass frame. The four main experiments are the following:

- ALICE (A Large Ion Collider Experiment) studies collisions of heavy ions. Its main goal is to characterise the physical properties of the Quark-Gluon Plasma (QGP), a state of matter created under the extremely high temperatures and energy densities.
- ATLAS (A Toroidal LHC ApparatuS) is one of the two general purpose experiments, which is designed to discover the Higgs boson, carry out precision measurements, and search for new physics phenomena.
- CMS (Compact Muon Solenoid) is the second general purpose detector, with the same physics program, located exactly on the opposite side of the LHC compared to ATLAS.
- LHCb (Large Hadron Collider beauty) investigates the properties of the beauty quark in order to study the differences between matter and antimatter, namely the charge conjugation parity symmetry (CP-symmetry).

LHC first began it's physics operation in 2009, and has since been the key to several achievements in particle physics, most notably the discovery of the Higgs boson in 2012 [2, 3].

1.1.1 CERN accelerator complex and particle beams

The accelerator complex of the LHC (figure 1.2) consists of several separate particle accelerators, that are used sequentially to accelerate particles to their collision energy. Protons are provided by the linear accelerator Linac4 [4], which accelerates H^--ions (hydrogen atoms with an additional electron) to 160 MeV preparing them to enter the Proton Synchrotron Booster (PSB). H^--ions are created from hydrogen plasma in Linac4 ion source [5]. Linac4 uses radio frequency (RF) cavities to charge a series of conductors alternatively positive and negative, causing the particles to be accelerated. H^--ions are focused to a tight beam using quadrupole magnets after being pulsed through the accelerator. The ions are injected from Linac4 into the Proton Synchrotron Booster, removing the two electrons from the ions during the process and leaving only protons which are further accelerated to energy of 2 GeV for injection into the Proton Synchrotron (PS).

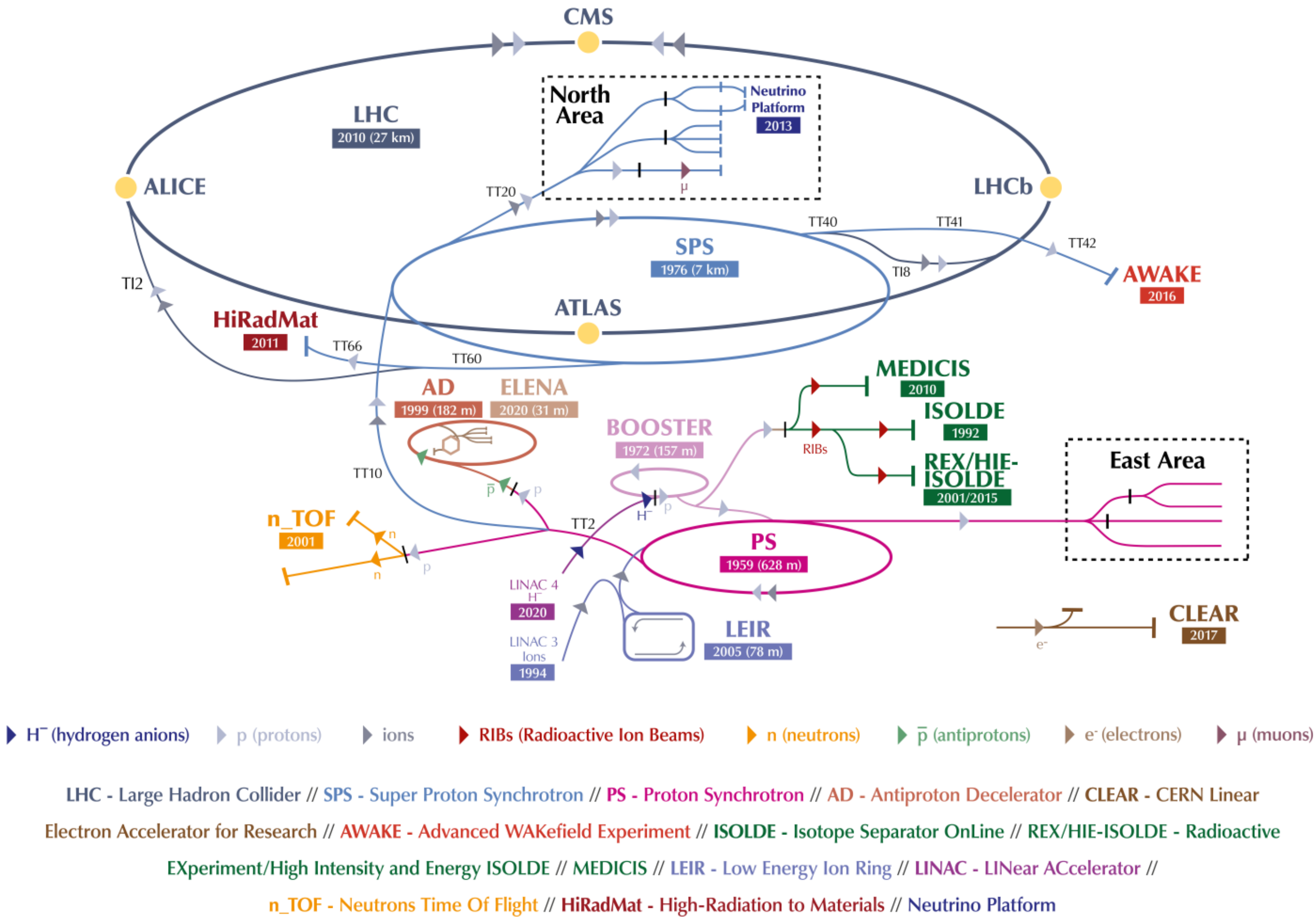

Figure 1.2. *CERN accelerator complex, highlighting the large number of interconnected systems. The four large experiments are marked with yellow dots. Proton path to the Large Hadron Collider can be traced along marks LINAC4, BOOSTER, PS, SPS, LHC . Figure from Ref. [6].*

Protons injected into the PS are then accelerated to 26 GeV energy and further injected into the Super Proton Synchrotron (SPS). SPS is a large synchrotron with almost 7 kilometres in circumference, and it was previously used as a proton-antiproton collider in discovery of W and Z particles. SPS accelerates the particles to 450 GeV before transferring them to the two beam pipes of LHC. The protons' energy is then increased up to 7 TeV in the LHC, making them ready for collisions at centre-of-mass energy of 14 TeV. Run3 will operate at a centre-of-mass energy of 13.6 TeV, while the higher energy of 14 TeV will be reached in a subsequent data taking period.

It is also possible to use heavy ions instead of protons at the LHC, namely, lead and xenon cores. Ions are provided by Linac 3, which removes electrons from atoms inside plasma, and accelerates them to 4.2 MeV. These ions are then injected into the Low Energy Ion Ring (LEIR), which accelerates them to 72 MeV and forms suitable sized bunches by splitting the bunches delivered by Linac 3. The ions can then be injected to PS in a similar manner to protons, where they follow the same chain of accelerators to the LHC.

Particles in the LHC are grouped into bunches and are accelerated by RF cavities. A typical bunch population (the amount of protons in a single bunch) is $1.15 \cdot 10^{11}$ at the start of a proton physics fill. Figure 1.3 contains an illustration of a particle bunch being accelerated by an oscillating electric field in a RF cavity.

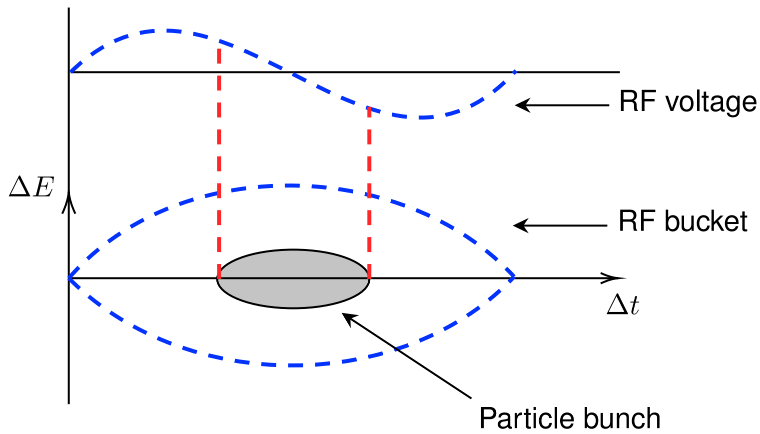

Figure 1.3. *Particle bunch occupying an RF bucket while being accelerated by electrical field in an RF cavity.*

These bunches travel very close to the speed of light in the LHC, which has a circumference $p_{\mathrm{LHC}} \approx 26\ 659\ \mathrm{m}$, and have an orbit frequency of $f = c/(p_{\mathrm{LHC}}) \approx 11245\ \mathrm{Hz}$. Knowing the frequency of the oscillating electric field in RF cavities $f_{\mathrm{RF}} = 400\ \mathrm{MHz}$, we can calculate the corresponding harmonic number

$$h = \frac{f_{\mathrm{RF}}}{f} = \frac{f_{\mathrm{RF}} \cdot p_{\mathrm{LHC}}}{c} \approx 35640 \tag{1.1}$$

This means, that there are 35640 so called *buckets* available for particles to be located in. The time difference between buckets can be calculated as

$$\Delta_{\mathrm{t}} = \frac{1}{f \cdot h} \approx 2.5\ \mathrm{ns} \tag{1.2}$$

which is small enough to set demanding requirements for resolution of detectors measuring quantities per individual bucket. The particle bunches are located in *bunch slots*, which are formed of ten RF buckets where only the first bucket is nominally filled with particles, such that two bunches are separated by 25 ns. The bunch slots are assigned a number from 1 to 3564, which is called the Bunch Crossing IDentifier (BCID). Having multiple filled bunches in a row is referred to as a *bunch train*, where the first bunch is further called a *leading bunch* and following bunches *train bunches*. The differences in response to leading and train bunches is often studied when studying detector properties, such as luminosity calibration non-linearity with respect to a given single bunch luminosity [7].

1.2 Compact Muon Solenoid

The Compact Muon Solenoid (CMS) [8] is one of the two general purpose detectors at the LHC. An overview of the CMS detector is shown in figure 1.4, where different parts of the detector are labelled.

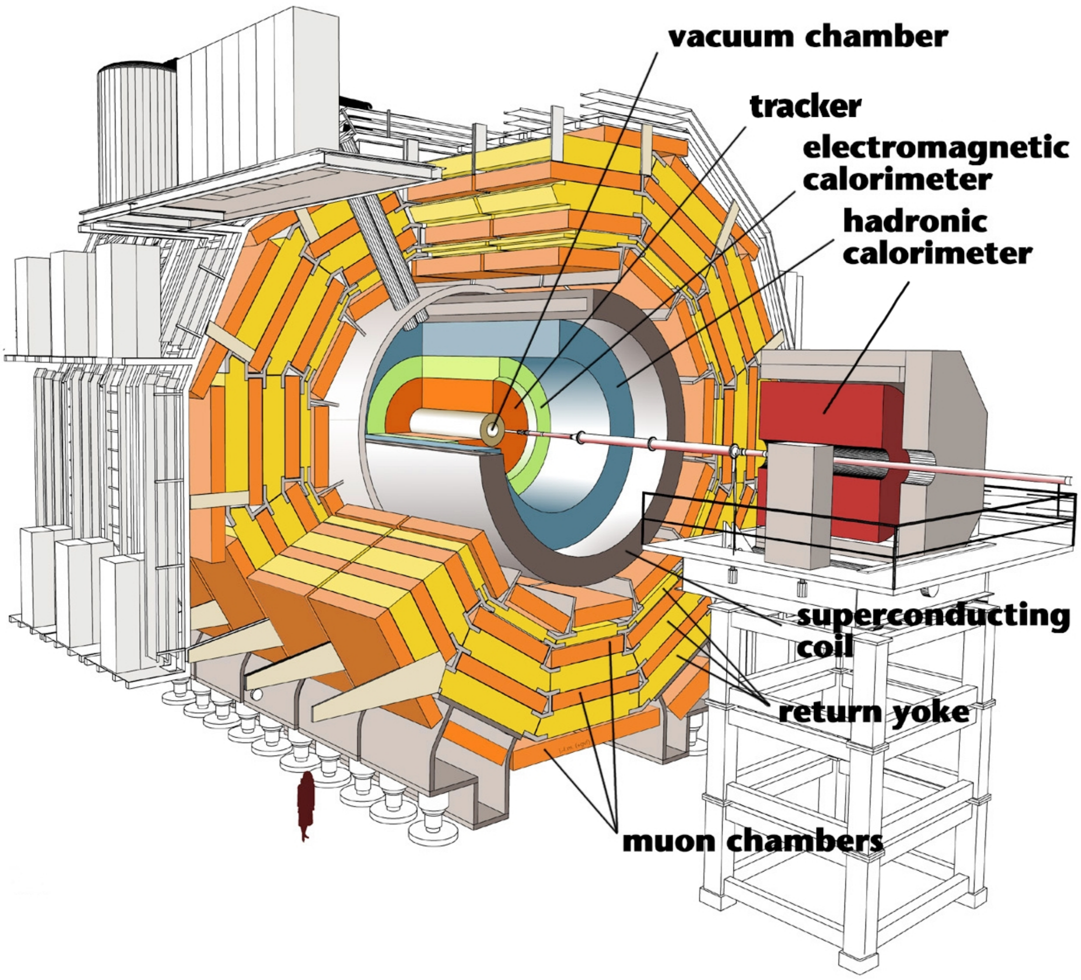

Figure 1.4. *Schematic picture of the Compact Muon Solenoid detector displaying it's cylindrically symmetric layers. The beam pipe is visible passing through the centre of the detector. Figure adapted from Ref. [9].*

The CMS physics program focuses on the discovery of the Higgs boson particle and determining its features, to verify its compatibility with the Standard Model of particle physics, on precision measurements to test the Standard Model of particle physics at unprecedented luminosities, and on investigations about the possible existence of new physics phenomena at new energy scales. The CMS detector is built of several layers, each dedicated to a certain type of measurement to identify and characterise the decay products of beam particle collisions. A schematic image showing the interactions of particles with different layers of the CMS detector is displayed in figure 1.5 and explained below.

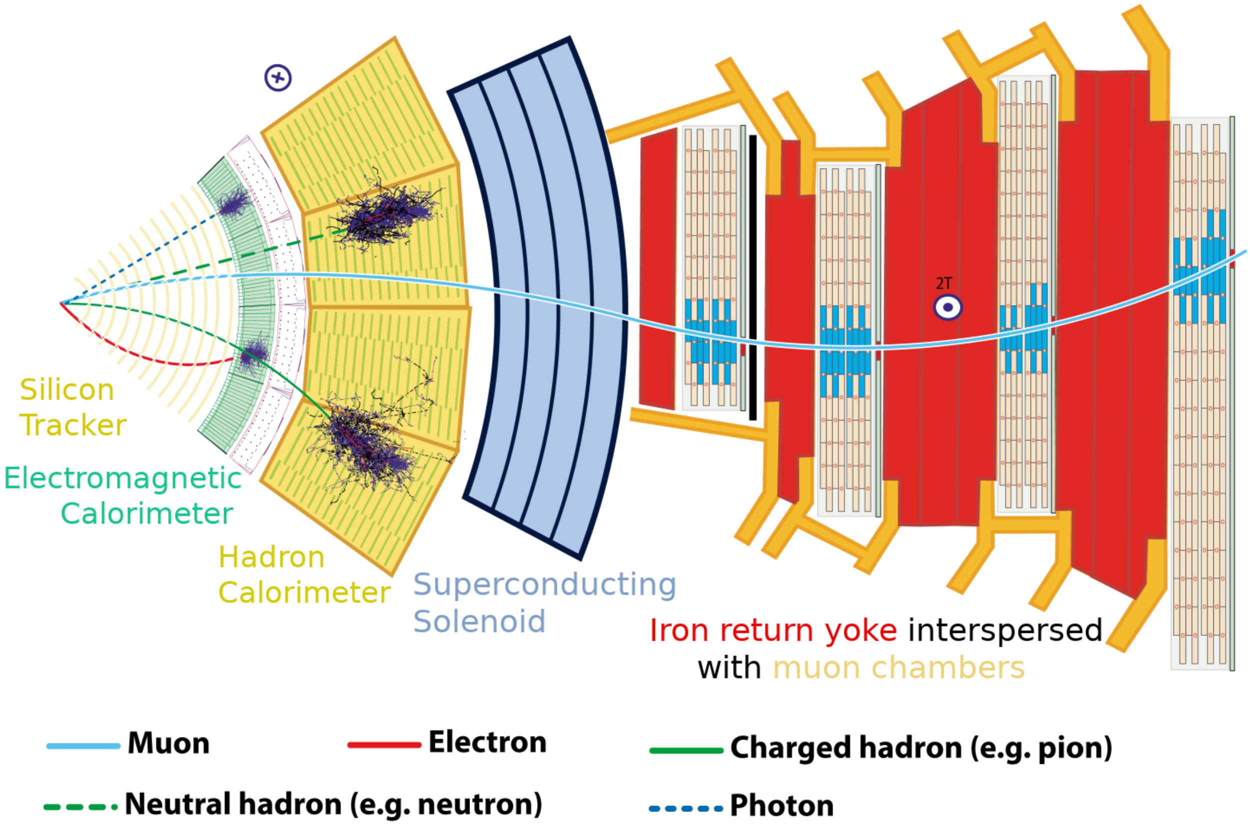

Figure 1.5. *Illustration of the elementary particles interacting in the Compact Muon Solenoid subdetector and how they are detected. Figure adapted from [10].*

The innermost part of the detector, *Tracker*, consists of silicon pixel and silicon strip detectors which trace the position of passing charged particles. The CMS magnet bends the trajectories of said particles, and measuring their position allows estimation of their momenta using the curvature of their paths. The two layers outside tracker are called calorimeters, which measure the energy of incoming particles. Light particles interacting electromagnetically, like electrons and photons, are stopped by the Electromagnetic Calorimeter (ECAL). Also *jets* or bursts of particles produced by quarks are perceived with ECAL. The next layer is another calorimeter which measures hadron's properties, called Hadronic Calorimeter (HCAL). The most important task of the HCAL [11] is to measure the energy of hadronic jets and neutral hadrons, which interact through the strong force. It is built from alternating layers of scintillators and absorbers, and consists of a barrel (HB), an outer part (HO), end-caps (HE) and forward calorimeter (HF) installed as a separate component to the very end of CMS. The usage of HF as a luminometer is discussed in Sec. 1.3.3. Particles that pass through HCAL are either heavy in mass or weakly interacting. Muons can reach and are tracked using the outermost layer of CMS, the muon chamber. The muon chamber measures the curvature of muons that pass through alternating layers of *muon stations* and iron *return yoke* plates. It is worth noting that the CMS detector cannot directly measure neutrinos, them having such low rest mass and rather feeble interaction. However, combining the transverse momentum of all perceived particles allows to infer the presence of neutrinos, relying on the energy conservation and the fact that the initial transverse energy of the beam particles is null.

1.3 Detectors used for luminosity measurements at CMS

The luminosity at CMS is measured by the BRIL (Beam Radiation Instrumentation and Luminosity) group, which is also responsible for monitoring beam-induced background, monitoring dangerous beam loss events that can trigger a beam abort, beam timing and minimum bias triggers for data taking, and monitoring/simulation of radiation environment in the CMS cavern. The BRIL group performs luminosity measurements exploiting several CMS sub-detectors and some dedicated luminometers. BRIL luminometers function independently from the CMS data taking, and can provide instantaneous per-bunch measure on luminosity. Figure 1.6 shows all systems operated by BRIL group.

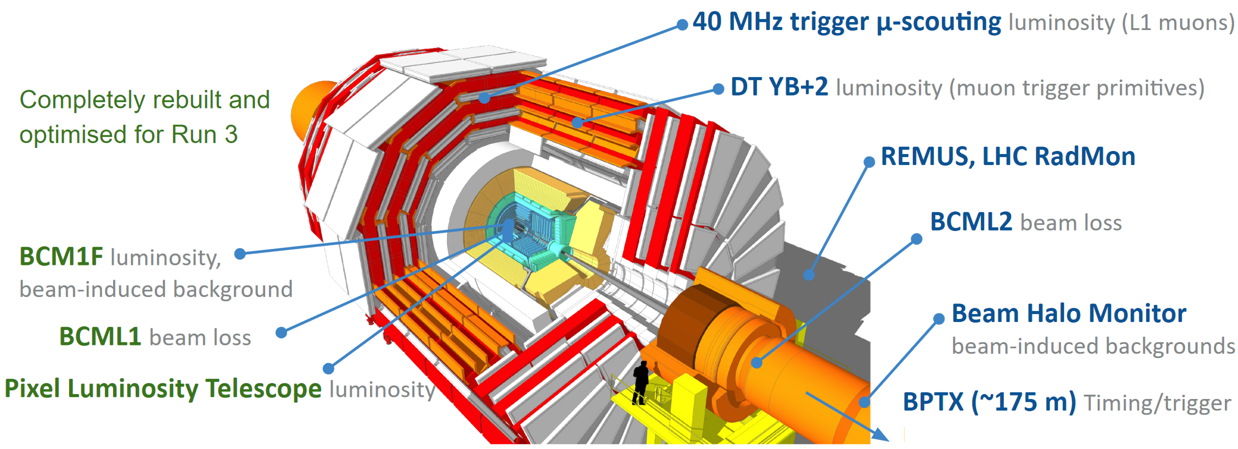

Figure 1.6. *Systems operated by BRIL group at the Compact Muon Solenoid experiment. Green text indicates, that the instrumentation has been rebuilt for Run 3.*

Both BRIL luminometers have been rebuilt with improvements during LS2. Below, the two luminometers operated by BRIL and the usage of Forward Hadronic Calorimeter as a luminometer are described in detail, as they are more relevant for the topic of this thesis.

1.3.1 Pixel Luminosity Telescope

The Pixel Luminosity Telescope (PLT) [12, 13, 14] is one of the dedicated systems used to measure luminosity at the CMS experiment. It uses silicon pixel detectors arranged into sets of three, each set forming a telescope, in the longitudinal direction corresponding to that of the beam pipe. There are a total of eight *telescopes* on both sides of the interaction point (IP), for a total of 16 effective readout channels, one for each telescope. [15] Figure 1.7 shows the structure of the PLT device. The silicon detectors in PLT are bump bonded to an advanced PSI46v2 readout chip [16], which is capable of operating in so-called *fast-or* mode, a special mode that can read signal at full bunch crossing rate of 40 MHz.

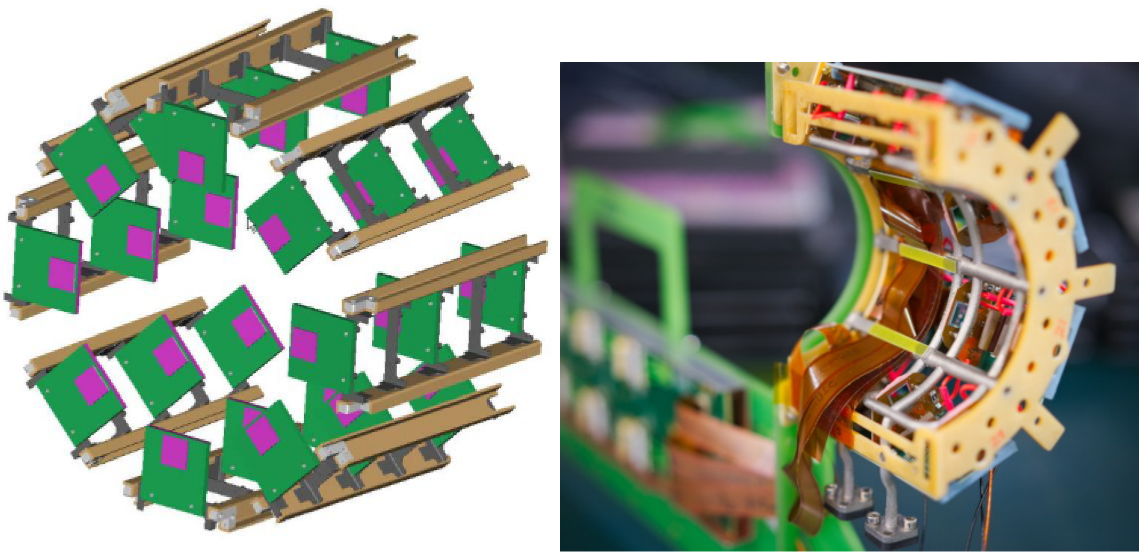

Figure 1.7. Left*: Schematic image of the Pixel Luminosity Telescope (PLT) showing eight sets of three pixel detectors forming eight telescopes. Figure from Ref. [15].* ***Right****: Photo of four PLT telescopes ordered to a quadrant with mounting support and connections to the readout electronic visible. Figure from Ref. [17].*

In the PLT a signal is recorded when a particle releases energy above the readout chip threshold (hit) sequentially in all three pixel sensors of a telescope, which is referred to as a *triple coincidence*. This allows to intercept real tracks and greatly reduces the contribution of noise, which makes the PLT capable to mitigate sources of background. Figure 1.8 displays the process of registering a triple coincidence.

The luminosity measurement is obtained from the fast-or rate using a *zero-counting* technique [15]. Specifically, if the fraction of collisions with no triple coincidences in a given telescope is given by f_0, then the mean number of triple coincidences per collision μ for that telescope is given by $\mu = -\ln f_0$. A more detailed description of the method is pro-

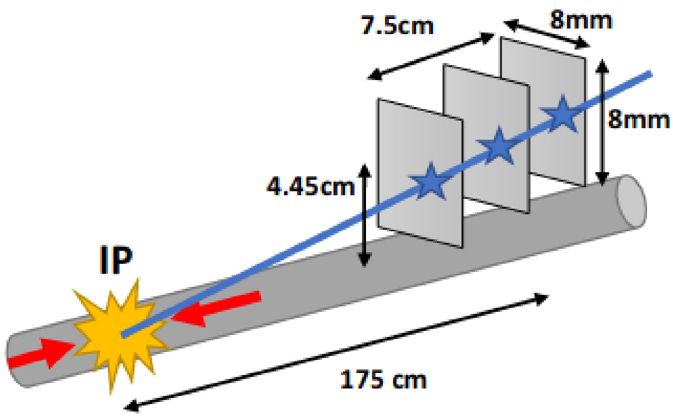

Figure 1.8. *Three planes of a PLT telescope, displaying the formation of a triple coincidence. Figure from Ref. [18].*

vided in Sec. 2.5. The use of the zero-counting method eliminates possible systematic effects due to hits from multiple tracks overlapping, or events with more tracks than can be distinguished in the fast-or readout. The main drawback of the zero-counting method is the potential for *zero starvation*, if f_0 is so low that the uncertainties become extremely large. However, the typical PLT occupancy is on the order of 0.1–0.2 triple coincidences per telescope per colliding BX at typical physics luminosities, so this is typically not a concern. Each channel can measure the luminosity separately from the other channels and their arithmetic average is taken to provide the entire PLT luminosity measurement. The system is capable of filtering out undesired channels if any exhibits malfunctioning during the data taking, and saving the registered hit histograms separately for each channel for offline processing.

1.3.2 Fast Beam Condition Monitor

The Fast Beam Condition Monitor (BCM1F) [19] is used at CMS to measure instantaneous bunch-by-bunch luminosity and also beam-induced-background rates. The detector consists of four half circles, referred to as C-shapes, which are installed in pairs on both sides of the IP at a distance of 1.8 m, 7.2 cm from the beam line. There are a total of 48 readout channels in BCM1F, which are analysed using the zero-counting method described in Sec. 2.5. The distance from IP allows for separation of incoming and outgoing particles, as it corresponds to time-of-flight of 6.25 ns for relativistic particles. This introduces a way to separate signals originating from collisions, machine induced background (MIB), and noise caused by activation of nearby material, as the time difference between "in-going and out-going" bunches is 13 ns (approximately half of the bunch crossing rate). [20]

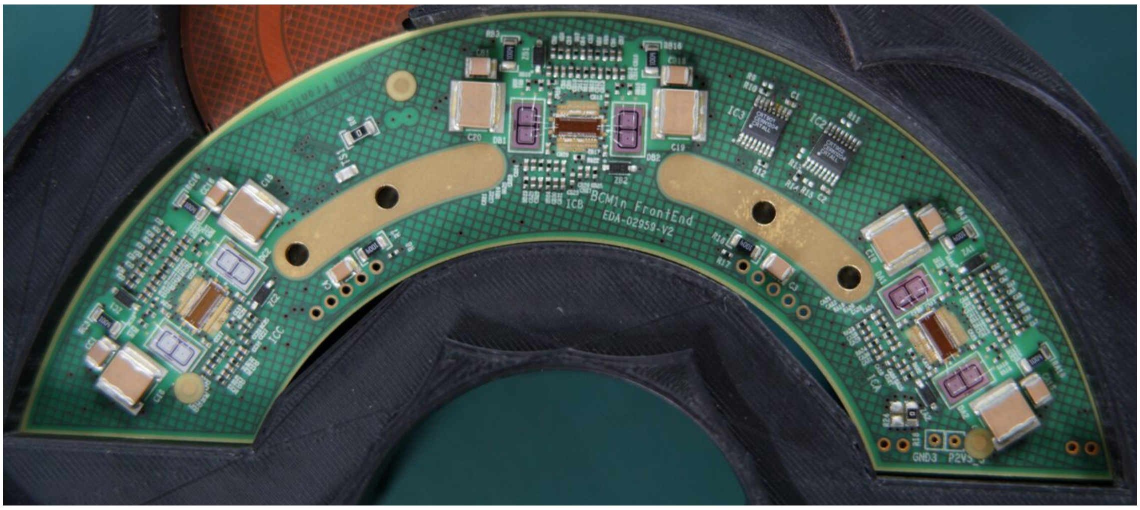

Figure 1.9. *Fast Beam Condition Monitor front-end electronics with installed ASICs, golden coloured mounting points visible. Figure from Ref. [21].*

The system was first commissioned in 2014, and operated between 2015 - 2016 using 500 μm thick single-crystalline chemical vapour deposition (sCVD) diamond sensors. Diamond was chosen over commonly used silicon because of almost five times wider band gap (distance between the electron valence band and the conduction band), which causes diamond sensors to have a lower response to ionising particle hits, while having lower *dark current* or noise signal being generated by thermal excitation when no particles enter the sensor. This allows operation without an active cooling solution, a highly desirable feature in tight spaces. Diamond also has high charge carrier mobility, which allows higher response speed than silicon. These sensors were found to show unstable behaviour after a relatively low dose of radiation, and had to have their operative high voltage (HV) lowered to compensate for the instability, which in turn greatly reduced the charge collection efficiency of the detector. In 2016, the sCVD sensors were replaced with poly-crystalline diamond sensors (pCVD) in the new version of the device [22]. The pCVD sensors were used until the end of Run 2, and were replaced with upgraded silicon sensors during LS2. The new sensors have AC-coupled silicon-pad detectors in radiation hard silicon substrate, and have an active cooling solution. These factors combat the downsides of silicon, while providing the stability of established silicon sensor technology.

Signal detected in the sensors is currently read with two parallel systems. The older back-end system utilises Versa Module Europa (VME) standard and has been used as the main system during Run 2, and beside it a newer µTCA-based system is intended to be used for Run 3 [23]. The µTCA unit will integrate both analog-to-digital converter and the Real-time Histogramming Unit (RHU) currently in use. The new system is currently in commission and both back-ends can be used in parallel. During the commissioning period, µTCA system is not integrated with CMS systems, but the data can be read with

BRIL systems. Results from the beam test period are compared using data from the µTCA and VME back-ends in Sec. 4.

1.3.3 Hadronic Calorimeter

The outermost calorimeter at CMS, HF (visible in foreground in figure 1.4), has been connected to BRIL data taking system for online luminosity measurement. The HF is a calorimeter that extends the CMS hadron calorimeter to small scattering angles and is located 11.2 meters from the CMS IP on both sides, covering the pseudorapidity range $3 < |\eta| < 5$, or approximately 5.7 to to 0.8 degrees from the beam pipe. The HF is constructed from quartz scintillators in steel absorber, which collect Cherenkov radiation. Only a subset of the detector is used for luminosity measurements, specifically rings 31 and 32 that cover pseudorapidity $3.15 < |\eta| < 3.50$. Data from HF is read using 36 separate channels, referred to as *boards*, and analysed using two different algorithms. The *HFET* method calculates the recorded transverse energy E_t to estimate the amount of arriving particles using the assumption, that the amount of arriving particles is proportional to the measured energy. The other method *HFOC* utilises the zero-counting algorithm 2.5 by tracking the fraction of bunch crossings with energy lower than a set threshold. The HF is prone to the afterglow effect, where the signal from a single colliding bunch produces a signal in one or more following bunches and introduces a falsely increased rate reading to train bunches [24]. This effect can be corrected with post-processing [25].

1.3.4 Other systems used for luminosity measurement at CMS

Other systems used by BRIL that are capable of measuring luminosity are described briefly below.

Tracker

The CMS tracker is capable of measuring paths of individual particles. The primarily used method to extract luminosity from this data is called pixel cluster counting (PCC), which counts the number of groups of adjacent hit pixels. Assuming a single cluster corresponds to a single elementary particle, one can extract a hit rate similar to one obtained from previously described luminometers. PCC is proven to provide a remarkably good linearity [26], but for the time being, the results are not obtained in real time, making it unsuitable for online luminosity estimation.

Muon system

The muon system is capable of estimating the number of muons produced as collision products. The drift tube (DT) is a sub-system of the muon barrel (MB) that provides an estimate for the number of muon tracks produced by the the Barrel Muon Track Finder (BMTF) algorithm [27]. The number of measured tracks can be assumed to be proportional to luminosity, enabling treating it as luminometer hit rate. The DT is capable of providing a real-time estimation of instantaneous luminosity.

RAMSES

The RAMSES (Radiation Monitoring System for the Environment and Safety) [28] is part of the wider REMUS (Radiation and Environment Monitoring Unified Supervision) system, and it is primarily responsible for radiation monitoring at the LHC. During Run 3, the LHC will be equipped with 12 inducted activity monitor (IAM) type RAMSES monitors, with two of them being placed in a location optimised for luminosity stability studies. These monitors are designed primarily to measure radiation levels when the LHC is not operational, but they are capable of providing a meaningful hit rate also during collisions, as a result of their large dynamic range.

2. MEASUREMENT OF LUMINOSITY

In this chapter we first discuss the concept of luminosity and describe it for the physics case at particle accelerator experiments. We then summarise on a given method to effectively measure the luminosity and the main systematic effects that affect the luminosity measurement in general.

2.1 Concept of luminosity

The probability for given processes in particle physics to happen are described by their cross section σ. The rate of events per time unit $\mathrm{d}R/\mathrm{d}t$ is proportional to σ and is given by multiplying it by the luminosity $\mathcal{L}$, which is instead an experimental feature and represent a system capability to produce interactions:

$$\frac{\mathrm{d}R}{\mathrm{d}t} = \mathcal{L} \cdot \sigma. \tag{2.1}$$

Having σ the dimension of a geometrical [area], the dimension of the luminosity is therefore $[\mathrm{area}]^{-1} \cdot [\mathrm{time}]^{-1}$, and most often $\mathrm{cm}^{-2}\mathrm{s}^{-1}$ or $\mathrm{fb}^{-1}\mathrm{s}^{-1}$ are chosen ($1\ \mathrm{b} = 1\ \mathrm{barn} = 10^{-28}\ \mathrm{m}^2$).

A useful quantity related to luminosity is the integrated luminosity

$$L = \int_{T_1}^{T_2} \mathcal{L}\mathrm{d}t, \tag{2.2}$$

as, on the other hand, it can be used to extract the cross section for a process knowing instead the number of events measured between T_1 and T_2:

$$\sigma = \frac{\text{Number of events}}{L}. \tag{2.3}$$

Looking at Eq. (2.1), luminosity can be understood as rate of particles passing through a surface area. Consider a particle flux

$$\Phi = \frac{N}{s} \tag{2.4}$$

passing through a target with cross section σ, density ρ and length l. This is displayed in figure 2.1.

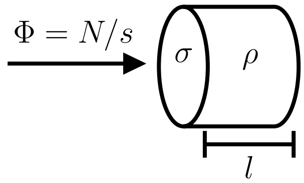

Figure 2.1. *Particle flux through a cylinder.*

The corresponding rate of interaction is

$$\frac{dR}{dt} = \Phi\rho l\sigma = \mathcal{L} \cdot \sigma. \tag{2.5}$$

2.2 Luminosity at particle accelerator experiments

At high-energy accelerators, the particle beams cross the beam pipe. For convenience, it is customary to adopt a natural coordinate frame with a right-handed cartesian system with the z-axis running tangent to the beam axis (in the direction of the Jura mountains for the CMS experiment). At CMS, the x-axis points radially inward-towards the centre of the LHC, which defines the direction of the y-axis to point vertically upward. Below, the particle densities are described in the x,y plane.

Let's consider two bunches of particles with densities $\rho_{1,2}$ having $N_{1,2}$ particles each. Integrating over their density at a given point in time results in

$$A = N_1 N_2 \iiint_{-\infty}^{\infty} \rho_1(x,y,s)\,\rho_2(x,y,s)\,\mathrm{d}x\mathrm{d}y\mathrm{d}s. \tag{2.6}$$

Including the time dependence as distance from the collision point as s_0 (approximately $c \cdot t$ in the LHC), we get

$$A' = N_1 N_2 \iiiint_{-\infty}^{\infty} \rho_1(x,y,s,-s_0)\,\rho_2(x,y,s,s_0)\,\mathrm{d}x\mathrm{d}y\mathrm{d}s\mathrm{d}s_0, \tag{2.7}$$

which is displayed in figure 2.2.

Noting, that there are two beams moving towards each other at relativistic speeds, we should include the Møller luminosity factor [29]

$$K = \sqrt{(\overline{v}_1 - \overline{v}_2)^2 - (\overline{v}_1 \times \overline{v}_2)^2 / c^2}. \tag{2.8}$$

In the case of beams colliding head on with same velocity $\overline{v}_1 = -\overline{v}_2$, we see that the

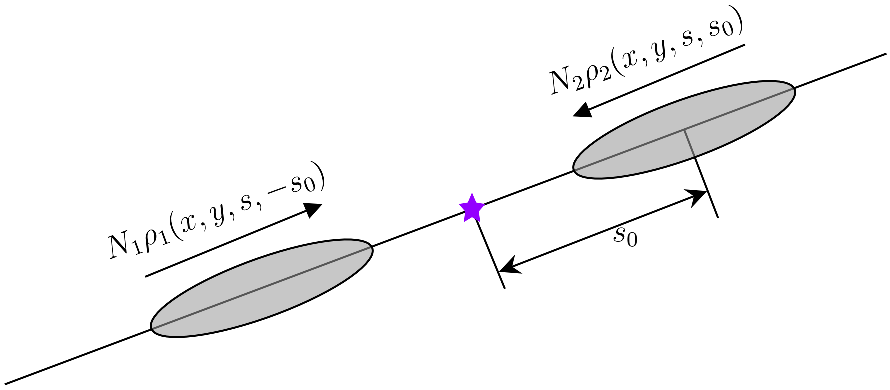

Figure 2.2. *Two particle beams colliding.*

Møller factor reduces to 2, as the cross product of opposing vectors is $\overline{0}$.

In the LHC, there are several colliding bunches during normal operation. This introduces a multiplier N_b to the total amount of interactions per time unit, equal to the number of bunches. These colliding bunches circle the LHC at approximate frequency f = 11 246Hz, which introduces a second multiplier to the total formula for interactions. Putting together Eq (2.7), Eq. (2.8) and the two remarks about multipliers, we arrive at

$$\mathcal{L} = 2fN_1N_2N_b \iiiint_{-\infty}^{\infty} \rho_1\left(x,y,s,-s_0\right)\rho_2\left(x,y,s,s_0\right)\mathrm{d}x\mathrm{d}y\mathrm{d}s\mathrm{d}s_0, \tag{2.9}$$

which is the simple formula for luminosity of head-on colliding beams.

Typically, it is possible to assume uncorrelated density distributions and factorise them as

$$\begin{aligned}\rho_1(x,y,s,s_0) &= \rho_{1x}(x)\rho_{1y}(y)\rho_{1s}(s-s_0)\\ \rho_2(x,y,s,s_0) &= \rho_{2x}(x)\rho_{2y}(y)\rho_{2s}(s+s_0).\end{aligned} \tag{2.10}$$

Combining Eq. (2.9) with Eq. (2.10), we get

$$\mathcal{L} = 2N_1N_2fN_b \iiiint_{-\infty}^{\infty} \rho_{1x}(x)\rho_{1y}(y)\rho_{1s}\left(s-s_0\right)\rho_{2x}(x)\rho_{2y}(y)\rho_{2s}\left(s+s_0\right)\mathrm{d}x\mathrm{d}y\mathrm{d}s\mathrm{d}s_0. \tag{2.11}$$

Assuming further that the distributions are Gaussian with mean $\mu_{1j} = \mu_{2j} = 0$ and standard deviation $\sigma_{1j} = \sigma_{2j}$ for $j = x,y,s$, we can use an analytical form for beam $i = 1,2$ in dimension $z = x,y$ as

$$\rho_{iz}(z) = \frac{1}{\sigma_z\sqrt{2\pi}}\exp\left(-\frac{z^2}{2\sigma_z^2}\right) \tag{2.12}$$

and in dimension s as

$$\rho_s\left(s \pm s_0\right) = \frac{1}{\sigma_s \sqrt{2\pi}} \exp\left(-\frac{\left(s \pm s_0\right)^2}{2\sigma_s^2}\right). \tag{2.13}$$

Using Eq. (2.12) and Eq. (2.13), and separating the integrals of Eq. (2.11), we get

$$\mathcal{L} = \frac{2fN_1N_2N_b}{(\sqrt{2\pi})^6 \sigma_s^2 \sigma_x^2 \sigma_y^2} \cdot$$
$$\int_{-\infty}^{\infty} \exp\left(-\frac{x^2}{\sigma_x^2}\right) \mathrm{d}x \int_{-\infty}^{\infty} \exp\left(-\frac{y^2}{\sigma_y^2}\right) \mathrm{d}y \int_{-\infty}^{\infty} \exp\left(-\frac{s^2}{\sigma_s^2}\right) \mathrm{d}s \int_{-\infty}^{\infty} \exp\left(-\frac{s_0^2}{\sigma_s^2}\right) \mathrm{d}s_0. \tag{2.14}$$

Noting that

$$\int \exp\left(-\frac{j^2}{\sigma_j^2}\right) \mathrm{d}j = \sigma_j \sqrt{\pi}, \tag{2.15}$$

we get for $j = x, y, s, s_0$

$$\mathcal{L} = \frac{fN_1N_2N_b}{4\pi^3 \sigma_x^2 \sigma_y^2 \sigma_s^2} \cdot \sigma_x \sigma_y \sigma_s^2 \pi^2 = \frac{fN_1N_2N_b}{4\pi \sigma_x \sigma_y}. \tag{2.16}$$

We see from this result, that the longitudinal deviation (bunch length) does not affect the luminosity.

In the case of beams having unequal deviations in the transverse plane, we can make a substitution for beams 1,2

$$\sigma_j = \sqrt{\frac{\sigma_{1j}^2 + \sigma_{2j}^2}{2}} \tag{2.17}$$

yielding

$$\mathcal{L} = \frac{fN_1N_2N_b}{2\pi \sqrt{\sigma_{1x}^2 + \sigma_{2x}^2} \sqrt{\sigma_{1y}^2 + \sigma_{2y}^2}}. \tag{2.18}$$

This is the common formula for determining instantaneous luminosity.

2.3 Calibration of luminometers

The hit rates recorded by luminometers can be converted into luminosity by multiplying them with a luminometer-specific calibration factor. It is assumed, that the luminometer perceives a constant fraction of collisions, which is ideally independent of beam parameters. This coefficient is referred to as visible cross section σ_{vis}, which has to be determined each time detector specifications are changed. Looking at Eq. (2.18), we can solve

$$\sigma_{vis} = \frac{R}{\mathcal{L}} = \frac{R2\pi\sqrt{\sigma_{1x}^2 + \sigma_{2x}^2}\sqrt{\sigma_{2y}^2 + \sigma_{2y}^2}}{fN_1N_2N_b}. \tag{2.19}$$

Beam sizes cannot be measured separately by colliding the beams together, instead what is measured are effective beam sizes (referred to as *CapSigmas* in literature) $\Sigma_i = \sqrt{\sigma_{1i}^2 + \sigma_{2i}^2}$ in dimensions $i = x, y$. These can be substituted to Eq. (2.19), yielding

$$\sigma_{vis} = \frac{R2\pi\Sigma_x\Sigma_y}{fN_1N_2N_b}. \tag{2.20}$$

It is worth noting that the normalisation done here per bunch as the number of bunches, N_b, is present in the denominator. This convention is not used in all cases, and should be distinguished from normalisation over LHC orbit.

2.4 Van der Meer scan methodology

The van der Meer scan or vdM scan method [30] was originally developed by Simon van der Meer for luminosity measurements at the Intersecting Storage Rings (ISR) particle accelerator at CERN. The same method is used in current times by the LHC experiments to measure the integral over the bunch particle densities in Eq. (2.21) and to determine the overall calibration of the luminometers. Using the notation introduced above, the instantaneous luminosity of a colliding particle bunch pair separated by (Δx, Δy) is given by

$$\mathcal{L}(\Delta x, \Delta y) = N_1N_2f\int \rho_1(x,y)\rho_2(x+\Delta x, y+\Delta y)\,\mathrm{d}x\,\mathrm{d}y, \tag{2.21}$$

assuming the beams collide with no crossing angle. In the vdM scan method, it is assumed that the two bunch particle densities are factorisable in x and y directions as

$$\int \rho_1(x,y)\rho_2(x+\Delta x, y+\Delta y)\,\mathrm{d}x\,\mathrm{d}y = \int \rho_1(x)\rho_2(x+\Delta x)\,\mathrm{d}x \cdot \int \rho_1(y)\rho_2(y+\Delta y)\,\mathrm{d}y. \tag{2.22}$$

Both sides of Eq. (2.22) can be integrated independently with relation to Δx and Δy while the other respective separation is kept fixed, yielding for x

$$N_1N_2f\int \rho_1(y)\rho_2(y+\Delta y_0)\,\mathrm{d}y = \int \mathcal{L}(\Delta x, \Delta y_0)\,d(\Delta x) \tag{2.23}$$

and further

$$\int \rho_1(x)\rho_2(x+\Delta x_0)\,\mathrm{d}x = \frac{\mathcal{L}(\Delta x_0, \Delta y_0)}{\int \mathcal{L}(\Delta x, \Delta y_0)\,d(\Delta x)}, \tag{2.24}$$

and likewise for y. The integration over Δx and Δy is implemented experimentally by scanning the two beams against each other by colliding the beams at altering beam-beam separations. The integral on the right hand side of Eq. (2.23) is evaluated by measuring the luminometer rate as function of beam separation used in the scan. After replacing the beam overlap integrals in x and y according to Eq. (2.24) for a head-on point (Δx_0, Δy_0), Eq. (2.21) becomes

$$\mathcal{L}(\Delta x_0, \Delta y_0) = N_1 N_2 f \frac{R(\Delta x_0, \Delta y_0) \cdot R(\Delta x_0, \Delta y_0)}{\int R(\Delta x, \Delta y_0)\, d(\Delta x) \cdot \int R(\Delta x_0, \Delta y)\, d(\Delta y)}, \tag{2.25}$$

where luminosity is replaced now by the rate $R(\Delta x, \Delta y)$ when the two beams are separated by $(\Delta x, \Delta y)$. Since the van der Meer procedure is a convolution of the two beams, it is common to write the integrals over the rate scan curves using the convoluted beam widths Σ_x and Σ_y of the two beams

$$\mathcal{L}(\Delta x_0, \Delta y_0) = \frac{N_1 N_2 f}{2\pi \Sigma_x \Sigma_y}, \tag{2.26}$$

which causes the final formula for the visible cross sections to be

$$\sigma_{vis} = \frac{2\pi \Sigma_x \Sigma_y R(\Delta x_0, \Delta y_0)}{f N_1 N_2 N_b}. \tag{2.27}$$

All quantities on the right hand side of Eq. (2.27) can be measured, where Σ_x and Σ_y are determined from fits of the scan curves based on luminometer rate measurements during the VdM scans. While the measurements of convoluted beam widths should be the same for all luminometers, the peaks of the corresponding scan curves depend on the luminometer in case: this is simply a consequence of luminometers having a different σ_{vis}. The comparison of the beam widths estimated from the scan curves provides an effective consistency check between luminometers.

Figure 2.3 illustrates the introduced beam separation as a function of time.

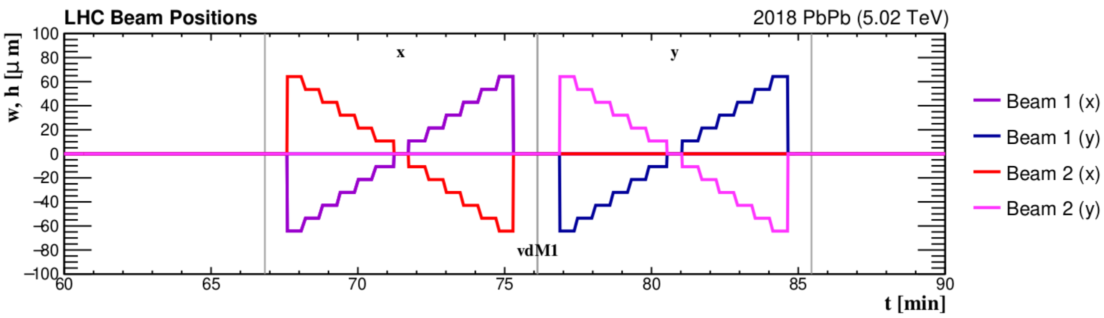

Figure 2.3. *Nominal LHC beam positions displaying the van der Meer scan sequence first in x- and then in y-axis.*

The scan in the figure above is done symmetrically with respect to the central axis, but more exotic scans are also performed. These include moving only one beam but keeping the one stationary in the middle, or introducing an offset in one direction producing a so called offset scan.

2.5 Zero counting method

Because of technical limitations of the read-out electronics of the luminometers, there exists a possibility that multiple particle hits taking place simultaneously are registered as a single hit. This calls for a more sophisticated method of hit counting. The number of hits may be assumed to follow Poisson distribution [31], such that we can write luminosity as

$$\mathcal{L} = \frac{\mu N_b f}{\sigma}, \tag{2.28}$$

where μ is the average number of inelastic collisions, and other variables follow the same convention as earlier. We can therefore determine the relative (uncalibrated) luminosity if μ is known. Assuming μ is a random variable following the Poisson distribution with x being the number of observed hits,

$$p(x;\mu) = \frac{\mu^x}{x!}\mathrm{e}^{-\mu}. \tag{2.29}$$

Noting the number of collisions without registered hits as $x = 0$ and calculating the corresponding probability $p(0)$, μ can be determined as

$$\mu = -\ln\left[p(0)\right] = -\ln\left[1 - \overline{p(0)}\right], \tag{2.30}$$

where $\overline{p(0)}$ is simply the amount of hits recorded, without the assumption of hits being created by a single particle.

2.6 Luminosity corrections

Various systematic effects that take place during vdM scans are compensated by applying a set of corrections to the measured rates and beam current. The inaccuracies stem from electromagnetic interaction between the beams, detector limitations, and other undesired effects like background noise. Magnitudes of these corrections are typically in the order of sub-percent, and rarely over one percent, and should be taken into account in order to provide a very precise luminosity measurement. These corrections are explained in this section.

2.6.1 Peak correction

In the event of a scan happening off centre of the designated beam overlap, the measured rate at zero nominal separation is not an actual measure of the head-on rate. The effect is illustrated in figure 2.4, where rate for a typical scan as well as a so called "offset scan" is displayed. Offset scan includes a deliberately introduced offset to the beams, which prevents them from colliding head on.

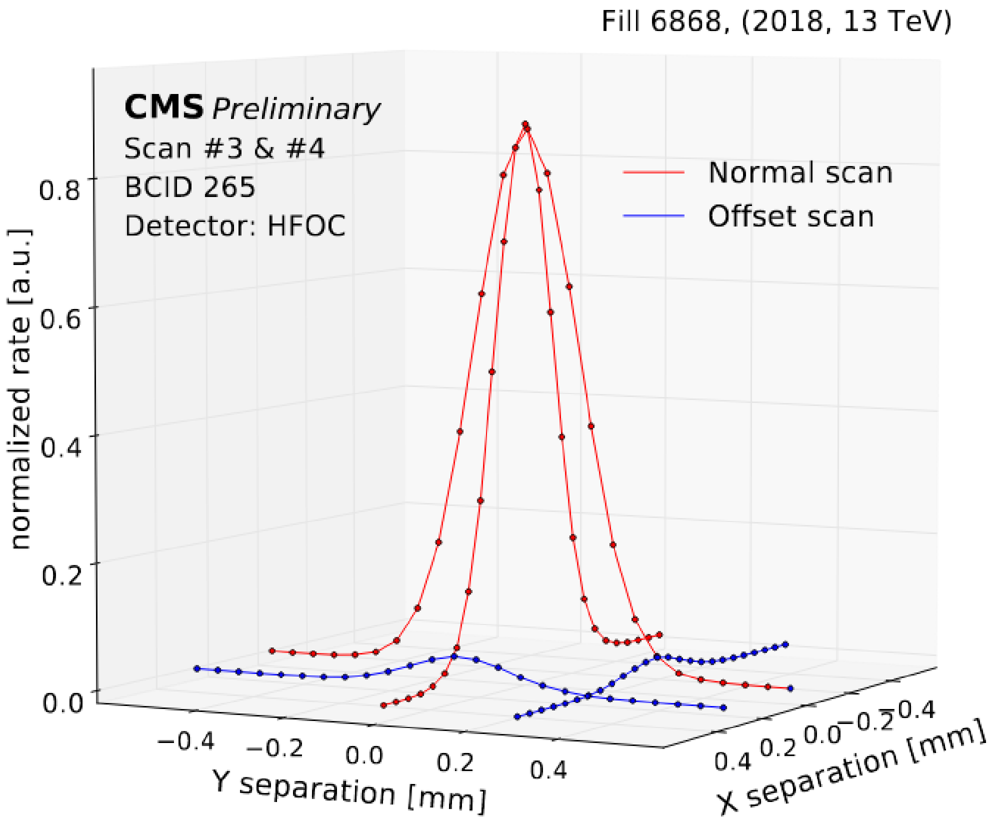

__Figure 2.4.__ Detector hit rates of a normal van der Meer (red lines) and an offset scan (blue lines) as functions of beam separation in x and y directions, highlighting the difference between the nature of the two scan types. Figure from Ref [32].

Let's consider a scan with a small, unintentional offset between the beams. This is shown in figure 2.5, the scan direction being towards / away from the reader. Scanning off centre the underlying distribution with mean of μ_1 and peak of $peak_1$, we instead have a distribution with peak $peak_2$. The incorrect peak can be corrected using reasonable assumptions of the beam overlap, most importantly the overlap following Gaussian distribution. Let's assume the underlying distribution in case is $X \sim \mathcal{N}(\mu_1, \Sigma)$ and the assumed mean is

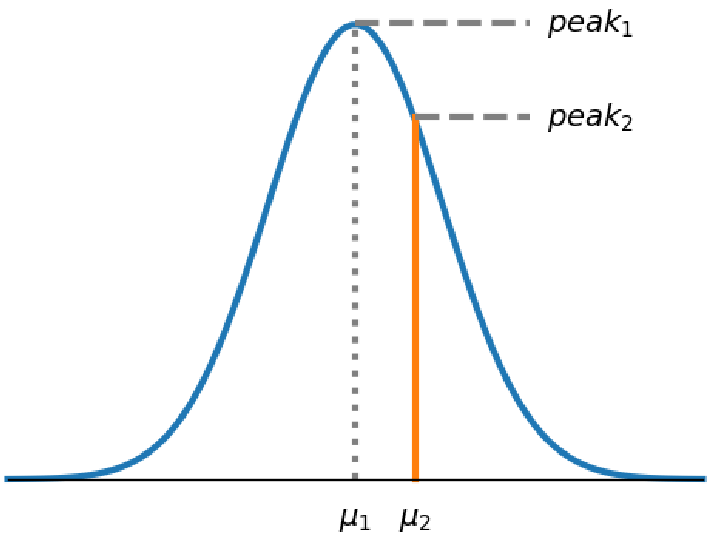

Figure 2.5. *Illustration of measured detector hit rates during a van der Meer scan performed along μ_2.*

μ_2. We can correct the peak by assigning a corrective factor of

$$\begin{aligned} p = \frac{X(\mu_1)}{X(\mu_2)} &= \frac{1}{\Sigma\sqrt{2\pi}} \exp\left[-\frac{1}{2}\left(\frac{\mu_1-\mu_1}{\Sigma}\right)^2\right] \cdot \frac{\Sigma\sqrt{2\pi}}{1} \exp\left[\frac{1}{2}\left(\frac{\mu_2-\mu_1}{\Sigma}\right)^2\right] \\ &= \exp\left[\frac{1}{2}\left(\frac{\mu_2-\mu_1}{\Sigma}\right)^2\right]. \end{aligned} \tag{2.31}$$

The scan is done along the primary axes of our coordinate system, so in our case $\mu_2 = 0$ and therefore

$$p = \exp\left(\frac{\mu_1^2}{2\Sigma^2}\right). \tag{2.32}$$

In the case of a scan being performed perfectly over the peak of the distribution, the correction evaluates to unity as $\mu_1 = 0$. The correct value for μ_1 can be determined from the scan in the orthogonal direction, as μ_1 is simply the location where maximal rate is measured. This can be accurately evaluated from the fit performed to the other plane.

Uncertainty associated to the correction can be estimated with propagation of error. The uncertainties $\Delta(\mu)$ and $\Delta(\Sigma)$ can be estimated reasonably well from the systematical uncertainties of the fitting procedure. Therefore

$$\Delta(p)^2 = \left(\frac{\partial p}{\partial \mu}\right)^2 \Delta(\mu)^2 + \left(\frac{\partial p}{\partial \Sigma}\right)^2 \Delta(\Sigma)^2, \tag{2.33}$$

where partial derivatives are

$$\begin{aligned}\frac{\partial p}{\partial \mu} &= \frac{\mu}{\Sigma^2}\exp\left(\frac{\mu^2}{2\Sigma^2}\right) = \frac{\mu}{\Sigma^2}p\\ \frac{\partial p}{\partial \Sigma} &= -\frac{\mu^2}{\Sigma^3}\exp\left(\frac{\mu^2}{2\Sigma^2}\right) = -\frac{\mu^2}{\Sigma^3}p\end{aligned} \tag{2.34}$$

and hence

$$\begin{aligned}\Delta(p) &= p\sqrt{\frac{\mu^2}{\Sigma^4}\Delta(\mu)^2 + \frac{\mu^4}{\Sigma^6}\Delta(\Sigma)^2}\\ &= p\sqrt{\frac{\mu^2}{\Sigma^6}\left[\Sigma^2\Delta(\mu)^2 + \mu^2\Delta(\Sigma)^2\right]}\\ &= p\frac{\mu}{\Sigma^3}\sqrt{\Sigma^2\Delta(\mu)^2 + \mu^2\Delta(\Sigma)^2}.\end{aligned} \tag{2.35}$$

Peak correction is taken into account in luminosity measurement and is implemented in the *vdM framework*, the framework used in CMS to measure the luminosity calibration with its corrections, as a multiplicative factor to the resulting σ_{vis}, as it is evident from Eq. (2.27) that σ_{vis} is directly proportional to the head-on rate. The typical magnitude of the correction is relatively small, especially in special van der Meer fills, where beams with large width are used.

2.6.2 Background correction

Rate measurements typically include a background signal caused by beam induced background, detector noise, and to a small extent the activation of nearby material. Background correction is performed by calculating a constant term describing the contribution from these sources, and subtracting it from rate measurements at each scan point. There are several ways to estimate background contribution, and two of those are described in this section. First described method is to measure the luminometer rates at a large beam separation (typically six times the nominal beam width in both x- and y-axes), where the contribution from collision products is negligible. This method provides a direct and accurate estimation for background rates, but involves dedicating beam time for the measurement. A more accessible method is to estimate rates associated with non-colliding bunches. This method can be applied to all scans done with a filling scheme that includes non-colliding bunches, but involves calculating the background indirectly with some assumptions in the following way:

$$BKG = 2 \cdot BIB + n, \tag{2.36}$$

where BIB refers to the beam induced background caused by a single beam and n detector noise. BIB is determined from rate of non-colliding filled bunches as

$$\begin{aligned} R_{\mathrm{NC}} &= BIB + n \\ \Leftrightarrow BIB &= R_{\mathrm{NC}} - n. \end{aligned} \tag{2.37}$$

BIB for only one beam is therefore measured, but during collisions there are two sources of beam induced background. This method requires the assumption, that the beam intensities are roughly equivalent and is therefore problematic if this is not the case. Detector noise n is assumed to be independent from beam induced background and can be estimated as the mean rate measured from two unfilled bunches "colliding". This is typically done using rate measured from the beam *abort gap* R_{AG}. Abort gap refers to the bunches with largest BCIDs, which are always kept empty to allow the beam to be directed to the beam dump when a fill needs to be terminated. BCIDs used for background estimation are 3444 – 3564 for luminometers other than BCM1F, where BCIDs 3421 – 3535 are used instead. BCM1F utilises the abort gap to include a special test pulse for internal operation, which should be excluded from background determination. Combining Eq. (2.36) and Eq. (2.37) yields for background

$$\begin{aligned} BKG &= 2 \cdot (R_{\mathrm{NC}} - R_{\mathrm{AG}}) + R_{\mathrm{AG}} \\ &= 2 \cdot R_{\mathrm{NC}} + R_{\mathrm{AG}} \end{aligned} \tag{2.38}$$

with corresponding statistical uncertainty estimated using propagation of uncertainty being

$$\Delta(BKG) = \sqrt{\frac{4\sigma(R_{\mathrm{NC}})^2 + \sigma(R_{\mathrm{AG}})^2}{N}}, \tag{2.39}$$

where N is the sample count. Both described background estimation methods are implemented in the vdM framework. The former is favoured in special van der Meer fills, where beam time can be allocated for background measurements, and the latter is used in *emittance scans* typically performed in the beginning and end of every fill. The magnitude of this corrections depends heavily on the detector it's being applied to, as the magnitude of background signal is detector dependent.

2.6.3 Beam-Beam deflection

During collisions of charged particles, the electromagnetic force between the colliding particles repels and attracts them to each other. This is the case also in proton-proton collision, where particles are affected by these forces in a way dependent on beam separation, which introduces a bias for results obtained with van der Meer scans. There are two separate effects caused by electromagnetic interaction. The first is the deflection between beams, described in this sub-section, the second is the dynamic beta correction, described in the next section.

The beam-beam deflection shifts the beams' orbital position, which distorts the measured beam overlap profile to be different than the true one in the case of head-on collisions. The effect can be compensated by introducing corrective factors to hit rates at each scan point, which are calculated using the Bassetti-Erskine formula [33].

Consider the Gaussian transverse charge density function

$$\rho(x,y) = \frac{Q}{2\pi\Sigma_x\Sigma_y} e^{-\left(\frac{x^2}{2\Sigma_x^2}+\frac{y^2}{2\Sigma_y^2}\right)}, \tag{2.40}$$

where Q is the bunch charge and Σ stands for convoluted beam width. Expression for the electric potential between deflecting beams has to satisfy equation based on the Poisson equation for electrostatic potential of Gaussian charge densities

$$\nabla^2\phi = \frac{\rho}{\epsilon_0}, \tag{2.41}$$

which has a solution

$$\phi(x,y) = \frac{Q}{4\pi\epsilon_0}\int_0^\infty \frac{e^{-\left[\frac{x^2}{2\Sigma_x^2+s}+\frac{y^2}{2\Sigma_y^2+s}\right]}}{\sqrt{2\Sigma_x^2+s}\sqrt{2\Sigma_y^2+s}}\mathrm{d}s. \tag{2.42}$$

The components of electric field E_x and E_y are

$$E_x + iE_y = -\frac{\partial\phi}{\partial x} + i\frac{\partial\phi}{\partial y}, \tag{2.43}$$

meaning in case of $\Sigma_x > \Sigma_y$, the electric field created on the probe beam by the opposite beam is

$$\begin{aligned} E_x &= \frac{Q}{2\epsilon_0\sqrt{2\pi(\Sigma_x^2-\Sigma_y^2)}}\,\mathrm{Im}\left[w\left(\frac{x+iy}{\sqrt{2(\Sigma_x^2-\Sigma_y^2)}}\right) - e^{-\left(\frac{x^2}{2\Sigma_x^2}+\frac{y^2}{2\Sigma_y^2}\right)} w\left(\frac{x\frac{\Sigma_y}{\Sigma_x}+iy\frac{\Sigma_x}{\Sigma_y}}{\sqrt{2(\Sigma_x^2-\Sigma_y^2)}}\right)\right] \\ E_y &= \frac{Q}{2\epsilon_0\sqrt{2\pi(\Sigma_x^2-\Sigma_y^2)}}\,\mathrm{Re}\left[w\left(\frac{x+iy}{\sqrt{2(\Sigma_x^2-\Sigma_y^2)}}\right) - e^{-\left(\frac{x^2}{2\Sigma_x^2}+\frac{y^2}{2\Sigma_y^2}\right)} w\left(\frac{x\frac{\Sigma_y}{\Sigma_x}+iy\frac{\Sigma_x}{\Sigma_y}}{\sqrt{2(\Sigma_x^2-\Sigma_y^2)}}\right)\right] \end{aligned} \tag{2.44}$$

and in case of $\Sigma_y > \Sigma_x$

$$E_x = \frac{Q}{2\epsilon_0\sqrt{2\pi(\Sigma_y^2 - \Sigma_x^2)}} \mathrm{Re}\left[w\left(\frac{y+ix}{\sqrt{2(\Sigma_y^2-\Sigma_x^2)}}\right) - e^{-\left(\frac{y^2}{2\Sigma_y^2}+\frac{x^2}{2\Sigma_x^2}\right)} w\left(\frac{y\frac{\Sigma_x}{\Sigma_y}+ix\frac{\Sigma_y}{\Sigma_x}}{\sqrt{2(\Sigma_y^2-\Sigma_x^2)}}\right)\right]$$
$$E_y = \frac{Q}{2\epsilon_0\sqrt{2\pi(\Sigma_y^2 - \Sigma_x^2)}} \mathrm{Im}\left[w\left(\frac{y+ix}{\sqrt{2(\Sigma_y^2-\Sigma_x^2)}}\right) - e^{-\left(\frac{y^2}{2\Sigma_y^2}+\frac{x^2}{2\Sigma_x^2}\right)} w\left(\frac{y\frac{\Sigma_x}{\Sigma_y}+ix\frac{\Sigma_y}{\Sigma_x}}{\sqrt{2(\Sigma_y^2-\Sigma_x^2)}}\right)\right], \tag{2.45}$$

where $w(z) = e^{-z^2}\left[1 + \frac{2i}{\sqrt{\pi}}\int_0^z e^{\zeta^2}\mathrm{d}\zeta\right]$ is the complex error function. [33] The deflection angles caused by electrostatical repulsion derived in [34] are

$$\begin{aligned}\theta_t &= \frac{2r_p}{\gamma}N_p E_x(x,y)\\ \theta_t &= \frac{2r_p}{\gamma}N_p E_y(x,y),\end{aligned} \tag{2.46}$$

where r_p is the classical radius of a proton, Np is the number of protons in the opposing bunch, and γ is the relativistic factor for proton. The orbitals shifts averaged over all particles in the bunch are

$$\begin{aligned}\delta x &= \frac{\langle\theta_x\rangle\beta^*}{2\tan(\pi Q_x)}\\ \delta y &= \frac{\langle\theta_y\rangle\beta^*}{2\tan(\pi Q_y)},\end{aligned} \tag{2.47}$$

where β^* is the β-function at the CMS interaction point, a beam optics parameter specific to the each experiment and charge densities Q_x and Q_y are the betatron tunes. Both of these parameters are obtainable directly from the CMS monitoring systems. The rates are corrected using a factor $\delta z_1 + \delta z_2$ separately for dimensions $z = x, y$, where 1 and 2 stand for beams 1 and 2.

2.6.4 Dynamic-beta correction

The second effect caused by electrostatic forces between the beam particles is the defocusing of the beam, which distorts the beam overlap shape when a scan is performed. To compensate this effect, corrective multipliers are introduced to rates in all scan points analogous to beam-beam correction. This procedure is called the dynamic-β correction.

Defocusing quadrupole effect of the beams changes the β-parameter of the system, distorting the charge distribution of the probe bunch. The β-parameter including the beam-

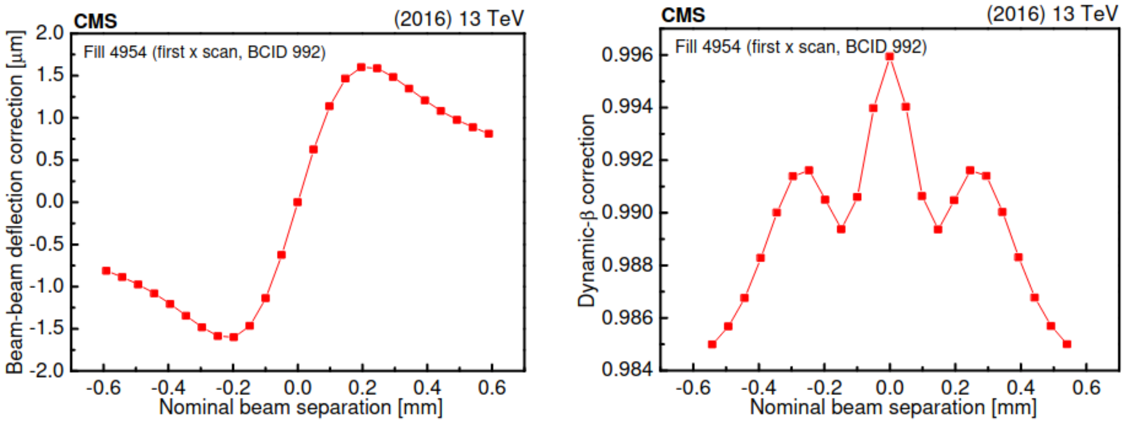

Figure 2.6. *Magnitudes of corrections for electromagnetic repulsion of the beams, calculated using nominal beam separations from a scan in fill 4954.* ***Left:*** *Beam-beam deflection calculated using Bassetti-Erskine formula.* ***Right:*** *Correction for dynamic-β effect. Figures from Ref. [26].*

beam interaction in dimensions $i = x, y$ is

$$\frac{\beta^*_{i0}}{\beta_i} = \sqrt{1 - (2\pi\xi_z)^2 + 4\pi\xi_z \cot(2\pi Q_i)}, \tag{2.48}$$

where β^*_{z0} is the nominal value, Q_z is the corresponding tune and ξ_z is another beam parameter defined as

$$\begin{aligned} \xi_x &= \frac{\beta^*_{x0} N r_p}{2\pi\gamma\sigma_x(\sigma_x + \sigma_y)} \\ \xi_y &= \frac{\beta^*_{y0} N r_p}{2\pi\gamma\sigma_y(\sigma_y + \sigma_x)}, \end{aligned} \tag{2.49}$$

where constants follow the same conventions as in Sec. 2.6.3. The rates at each scan point with separation Δ are corrected by multiplying them using a factor of

$$\frac{R_{\mathrm{corr}}(\Delta_x)}{R_{\mathrm{orig}}(\Delta_x)} = \sqrt{\frac{\beta^*_x(\Delta_x)}{\beta^*_{\mathrm{x,ref}}}} \sqrt{\frac{\beta^*_y(\Delta_y)}{\beta^*_{\mathrm{y,ref}}}} \exp\left[-\frac{1}{2}\left(\frac{\Delta_x}{\Sigma_x}\right)^2 \left(1 - \frac{\beta^*_{\mathrm{x,ref}}}{\beta^*_{\mathrm{x}}(\Delta_x)}\right)\right], \tag{2.50}$$

where R_{orig} is the rate measured by the luminometer and R_{ref} is a reference rate fixed to rate at $\Delta_x = \Delta_y = 0$.

Both corrections to beam-beam interactions can be applied using the vdM framework which utilises the formulas presented above. No supplementary data is therefore required in the analysis. Correction for beam-beam effects is typically in the order of -0.6% to +0.4% increase to the visible cross section [26].

2.6.5 Orbit drift correction

It is possible for the beam position to evolve during a vdM scan. This causes the beam separation to deviate from the nominal value, which can be corrected using measurements from the two beam position monitors (BPMs): the ones located in the LHC arcs adjacent to CMS (referred to as *arc BPMs* [26]) and the Diode ORbit and OScillation System (DOROS) [35]. Instead of fixed steps using nominal beam separations, the value from these devices is used providing a way to introduce a gradually changing value for the beam separation.

2.6.6 Length scale correction

Beam separation at CMS is determined using magnets, which set the beams to a specific position using a target value. The actual beam separation might however differ systematically from the nominal value. This effect can be measured using dedicated length scale scans, typically performed as a part of a vdM scan campaign. A length scale scan involves moving the beams at a straight line the same time, and measuring the actual beam separation using BPMs. A corrective multiplier to rates is then introduced to compensate the systematic offset in beam position. Length scale correction can be quite significant. To give an idea, it contributed to a reduction of -1.3% in visible cross section in year 2016 [26].

2.6.7 Beam current calibration and ghost & satellite correction

The beam current used in determining the visible cross section is measured with two sets of devices. The Fast Beam Current Transformer (FBCT) is capable of measuring the beam current with bunch-slot granularity (25 ns), while the other device Direct-Current Current Transformer (DCCT) [36] provides only the sum over all bunches. DCCT is however considered to be more accurate as FBCT [37], which invites to utilise both detectors for accurate per-bunch currents. The established method involves reading the bunch-by-bunch variation using FBCT, and normalising those values so that their sum equals to the DCCT value. This functionality is used by default in the vdM framework.

Particles may be erroneously located in non-colliding RF buckets. Particles in a non-colliding bucket in a colliding bunch slot are called *satellite charges*, while particles in nominally non-colliding bunch slots are referred to *ghost charges*. Contribution from these is included in the beam current measured by beam current transformers, which leads to overestimates the bunch intensities. Figure 2.7 displays the longitudinal beam profile

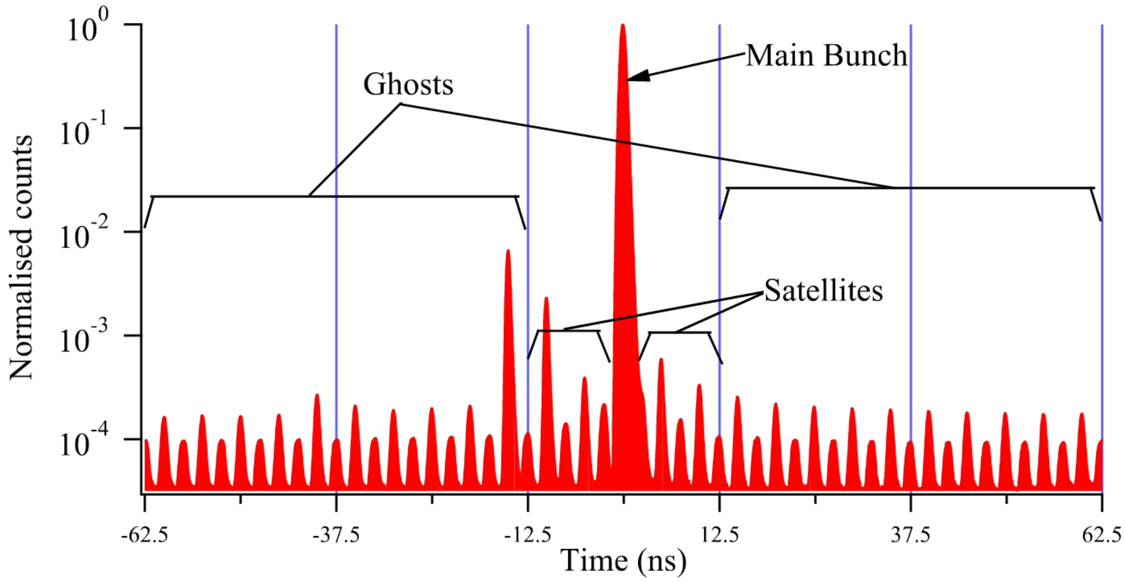

Figure 2.7. *Longitudinal profile of the LHC beam measured with Longitudinal Density Monitor (LDM), displaying the nominally filled bucket (middle), satellite charges close to the centre and ghost charges further out. Figure from Ref. [38].*

highlighting the contribution from ghost and satellite charges.

Contribution from these sources is measured with dedicated Longitudinal Density Monitor (LDM) devices, as well as the LHCb experiment [38]. A reductive multiplier may be added to the beam currents to compensate the increase in measured beam current caused by ghosts and satellites, equal to the fraction of these compared to the whole beam current. This effectively lowers the final normalisation done using beam current measured with DCCT.

3. VDM FRAMEWORK

In this chapter we present the van der Meer scan software that is used by the BRIL group to carry out the luminosity measurement used by the entire CMS collaboration. The focus is set on the original contribution I have brought to develop this tool with advanced programming techniques that render it effective and with new and improved functionalities. These new features allows to perform the data analysis in a more user-friendly fashion and very quickly to meet the prompt feedback required to perform such studies.

The *software stack* required to analyse van der Meer scans can be divided to online and offline systems. Data received from detectors and the central CMS systems is recorded using online systems. This data is then analysed with offline systems, which may include post-processing of the data. The most important software systems are described below.

3.1 Software used for the analysis of vdM scans

The vdM Framework [39] is a dedicated software tool used to analyse van der Meer scans at the CMS experiment. It was first commissioned as a self-contained tool in 2015, and it has been in use since then with new features being regularly added, while maintaining compatibility with data from previous data taking periods. The functionality of the newest version of the vdM Framework is covered in detail in this chapter. The most recent updates I have been working on are summarised in a comprehensive wiki [40] and include, among the other changes, an automatic code verification system implemented with GitLab's Continous Integration / Continous Delivery (CI/CD) tool.

3.1.1 Structure of the program

The newest version of the vdM framework is implemented in Python 3 and utilises a powerful data analysis framework, ROOT [41], developed at CERN. Data recorded by BRILDAQ 3.2 is given to the program in Hierarchical Data Format (HDF5/H5) [42] files. Data in these files used for vdM purposes are

- Luminometer rates for each luminometer in corresponding table. For example,for the case of the BCM1F detector they are in the table *bcm1flumi*.

- Beam currents N_1 and N_2 (also referred to as bunch intensities if it is given per bunch) in the table *beam*.
- Beam separations, scan step information and other scan-specific info in the table *vdmscan*.
- Optionally, beam lengths may be included. These are only used for determining beam emittance, which is not inherently related to detector calibration but can be performed by the vdM Framework.

The framework is capable of applying the several different types of corrections explained in 2.6.

The program progresses in the following steps:

- Read the H5 data file.
- Produce intermediate files of input quantities: separate files for scan info, beam current, rates and corrections.
- Apply corrections to rates and produce ROOT graph files of corrected rates.
- Fit a function to the rates. Typically a Gaussian. function, a Gaussian with an added constant, or a sum of two Gaussians are used. The possibly included constant term is not taken into consideration to the estimation of the peak of the fit, providing a way to address background signal.
- Compute the visible cross section σ_{vis} using peak rate and convoluted beam widths from the fits.

The overlap integral for an individual luminometer is measured from the rate normalised by the product of bunch currents, as a function of separation between beams. A Gaussian function is fitted to these values, where beam overlap width can then be read from. Two fits from different luminometers are displayed in figure 3.1, showing peaks of different magnitude but roughly same beam widths for both detectors.

Fit residuals are displayed in the figure below each fit, giving an insight on distribution of the residuals. Error bars in the residual plots are expressed in terms of one standard deviation of the measured hit rate (estimated as statistical error) from the residual mean.

3.1.2 Improvements for Run 3

The vdM framework has been actively used during period of accelerator and detector upgrade before the starting of Run 3, called long-shutdown (LS) 2 in order to analyse

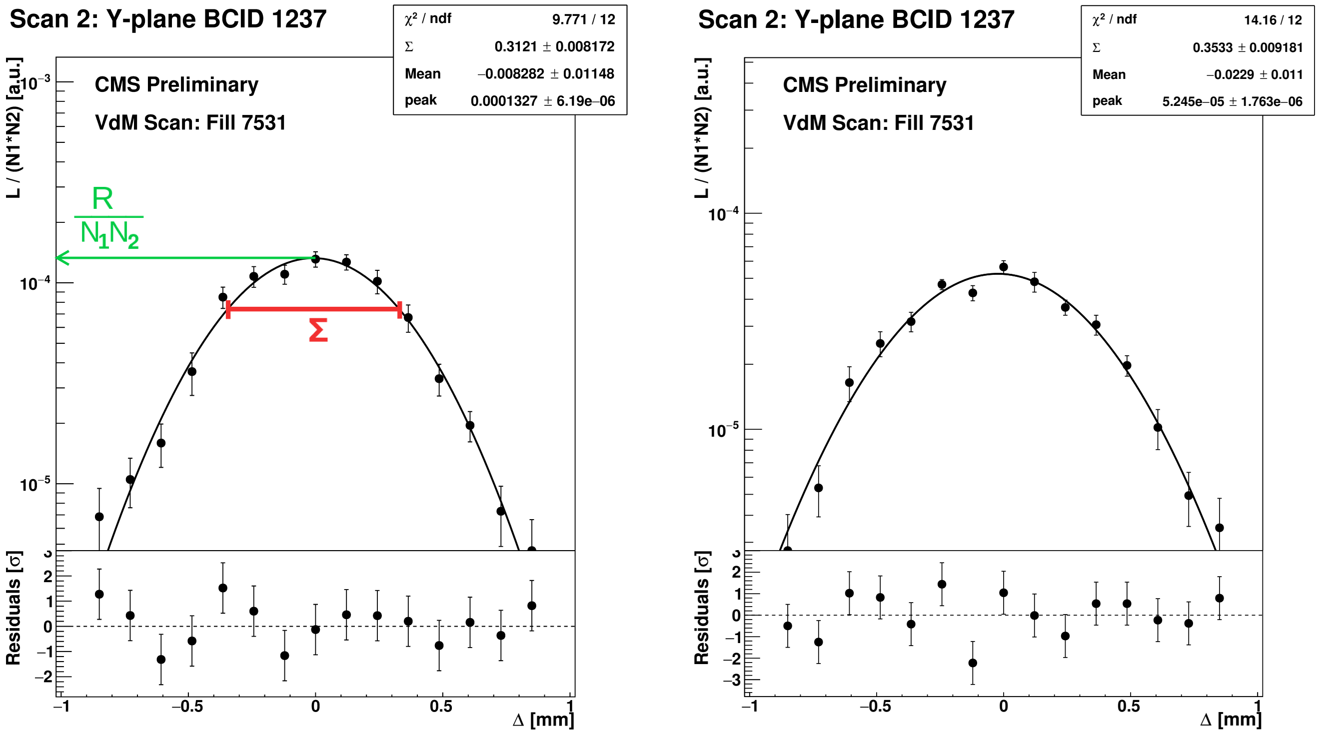

Figure 3.1. *Single Gaussian fit to detector hit rates normalised by the product of beam currents, with values of fit parameters visible in top right.* ***Left:*** *Pixel Luminosity Telescope, with added indications of fit parameters,* ***Right:*** *Fast Beam Condition Monitor.*

scans done in Run 2. During this period, several improvements have been made to the framework. These improvements include new features, performance updates and static updates to the program code (refactoring). A new version of the framework was created to Git branch "main", which is meant to surpass the current default branch while both preserving the current version, and following the naming scheme adapted by the two largest service providers for Git [43, 44]. The most important changes introduced in this branch are described here.

Usability

The method for running the framework has been improved in order to be easier to use. Previously the framework was configured using one JavaScript Object Notation (JSON) file, and three files with custom format, which would have to be parsed into valid JSON files by substituting "hard coded" variable names with their values. The largest configuration file was following this custom format and contained approximately 370 rows, bringing the total row count of configuration files to over 420. Experience has shown that using hard coded input and redundant code is not only ineffective and inelegant, but, more importantly, may easily induce in error. Because of this, a significant effort was devoted to improve and simply the usability by combining these configuration files into a single, readable document with as little redundancy as possible. A choice to use YAML format [45] was made, motivated by readable but concise layout and compliance with Python data types. The new configuration file is just over 100 lines, without counting empty rows and comments.

The directory and file structure of the program has been greatly changed. The framework is delivered with a set of utility scripts, all of which have not been updated alongside the core features, that are required by the scripts. Largely outdated files have not been transferred to the new branch. The project folder also contained several obsolete data files used in private analyses in the past, which also have not been propagated to the new edition. The directory structure did not follow best practices recommended for Python software, as files had to be imported from higher directory levels. In the past, this was made possible by including the whole project folder to system variable `PYTHONPATH`, which made dependency tracking difficult and effectively prevented import validation with static analysis tools. This setup was not ideal in terms of maintainability, which is an extremely important property for a project whose timescale would be order of 10-20 years. In order to solve this issue, the folder structure of the whole project was ameliorated by reorganising the files into sensible sub-folders. Lastly, the folder names are changed to follow a more uniform convention, favouring underscores instead of capitalisation to reflect the most recent Python Enhancement Proposal style convention (PEP-8). The new folder structure is displayed in figure 3.2.

The most important design philosophies with the new folder structure are separating source code, configuration files and data files. The division is done at the highest folder level with `config` containing the configuration files, `correction_data` data files and `src` source code. Folder `src` is further divided into sub-folders for rate file creation, corrections, fitting and plotting. There are two additional folders that are not essential for the core workflow: folder `scripts` contains scripts meant to be run independently, which are divided into "runners" that are used to call the program for a set of files, scripts used to test the program and "special scripts" which is a collection of utility scripts named after historical reasons. Folder `web` contains a file used to render the output folder to a format suitable for web environment using PHP.

Interaction with the user has been improved also by grouping printouts based on their im-

```
VdMFramework
├── config
│   ├── FOM
│   └── fits
├── correction_data
├── docs
├── external
└── src
    ├── correction
    │   └── correction_utils
    ├── correction_application
    ├── fits
    ├── plotting
    │   ├── plotting_config
    │   └── plotting_dependencies
    ├── ratefile
    ├── scripts
    │   ├── CICD
    │   ├── runners
    │   └── special
    └── web
```

Figure 3.2. *Structure of the vdM framework with some innermost sub-folders with self-explanatory names left out for clarity.*

portance. Previously the common convention was to forward the output of the program to a log file, which could easily exceed thousands of lines in size. A procedurally generated log file is now created in the output folder in a dedicated folder. Four levels of importance for logging messages are used (from least to most important): `DEBUG`, `INFO`, `WARNING` and `ERROR`. These are native types of the *logging* Python module, which has also support for a so far unused level `CRITICAL`. Specifying the level of logging can be done with a new flag `-v/--verbose`, which suppresses messages of lower priority while keeping the ones with priority of equal or higher. In addition to the created log file, messages with priority `WARNING` are printed to console in order to direct the user's attention to possible issues. The logging levels are described below.

DEBUG is the most verbose one and is supposed to be used for locating issues and as help for development. It may include printing values of variables for verification purposes and typically produces an extremely long log file. It is worth noticing that several Python libraries support this module natively, which allows them to display their own messages if this level is chosen.

INFO contains information about the run-time status of the program when no problems are detected. This is the default level and the recommended one to be used for offline analyses.

WARNING is an indication that the user has to do an action. Most often the program has triggered an automated functionality, and the user has to make sure it was intended to happen. This includes filtering out data points that are considered erroneous, or the data file containing multiple run numbers (this has been observed to cause minor problems with timestamps).

ERROR means the program was not able to continue after a certain point. This is most often caused by a data abnormality and always requires intervention.

The log messages are displayed in standardised format, which includes the file and line number where the message was printed. This has been proven to be useful for troubleshooting.

Performance of the program has been improved by altering the way multiprocessing is implemented. Historically the whole program was internally first ran for one luminometer to produce general files common for all luminometers, followed by running the program for remaining luminometers in parallel. Creating common files has been moved away from the multi-threaded section of the program to the previous step, allowing parallel processing of rates for all luminometers.

Automatic plotting functionality

Additional automatically generated plots have been added to complement the process of analysing large amounts of scans. This is a desired feature motivated by the need of the analysers to have quick and easy access to a set of key plots to understand the data that previously required more time before they were available. Automatically generated plots are implemented using the existing collection of scripts, with a new file `make_plots.py` been added to create required configurations. Automatic plots include the following plots described below.

Ratios of the peaks of the fits and rates at 0 separation are compared between x and y directions is displayed. The average of the ratio, the standard error on the mean and the number of bunches are also visible. An example set of figures is displayed in Fig. 3.3.

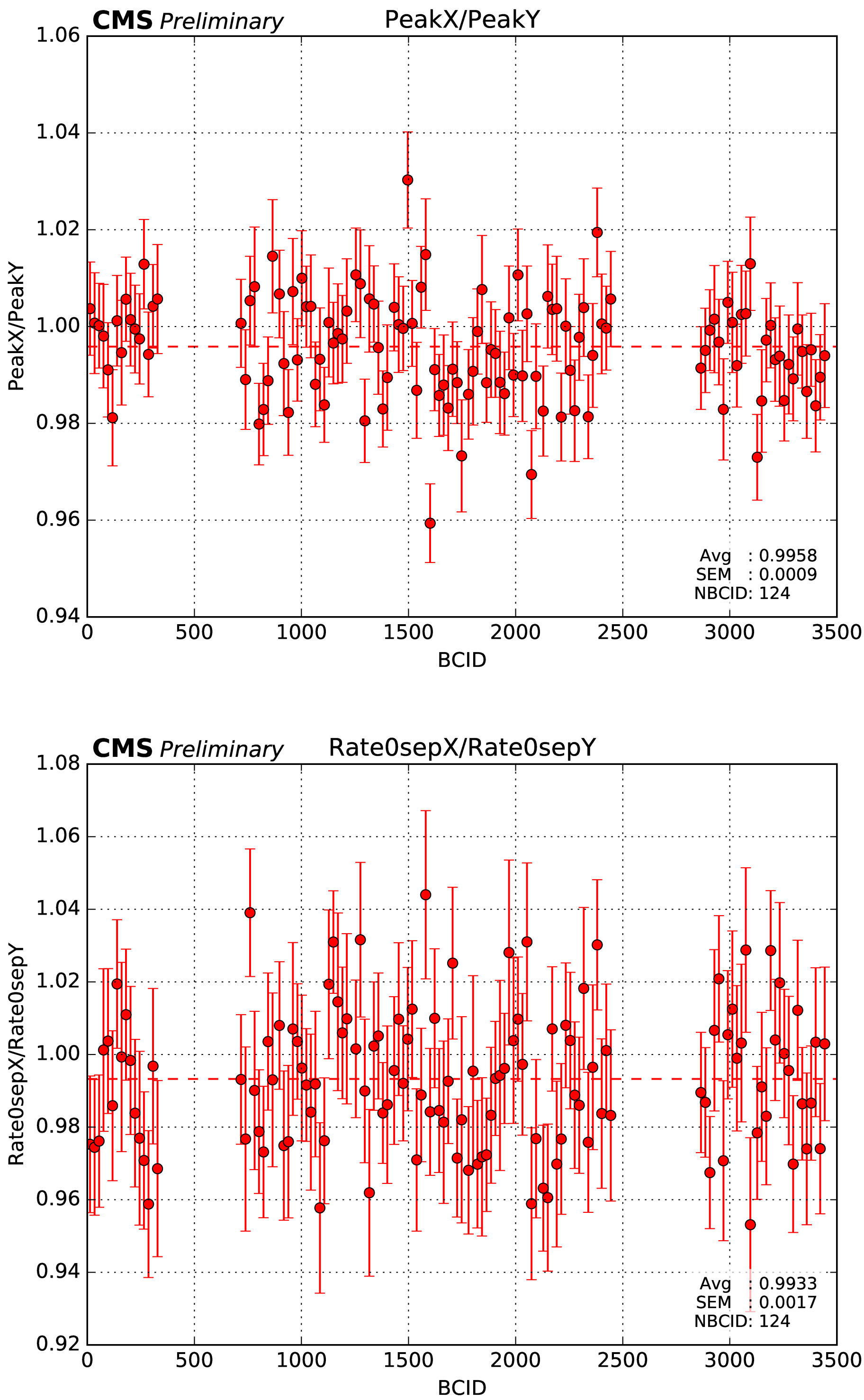

Figure 3.3. *Ratio plots of quantities between x and y directions, including the average (Avg.), standard error of the mean (SEM) and the number of colliding bunches (NBCID).* ***Top****: Peak of fit.* ***Bottom****: Head-on rate.*

Visualisation of normalised χ^2 values for a scan in x-axis is displayed in figure 3.4. The shorthand notation in the title of the bottom image stands for applied corrections and fit function, here the correction combination standing for "background, orbit drift separation, orbit drift rate, beam-beam deflection, dynamic-β, length scale and peak correction", and the fit notation standing for "single Gaussian". Also the year and centre-of-mass energy are displayed. A similar plot is also created for χ^2 in y-axis.

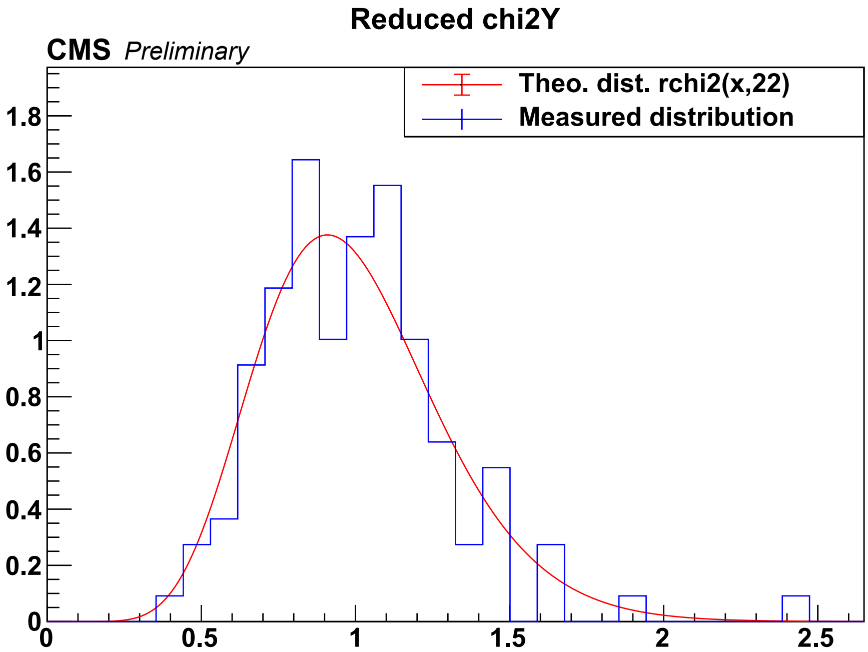

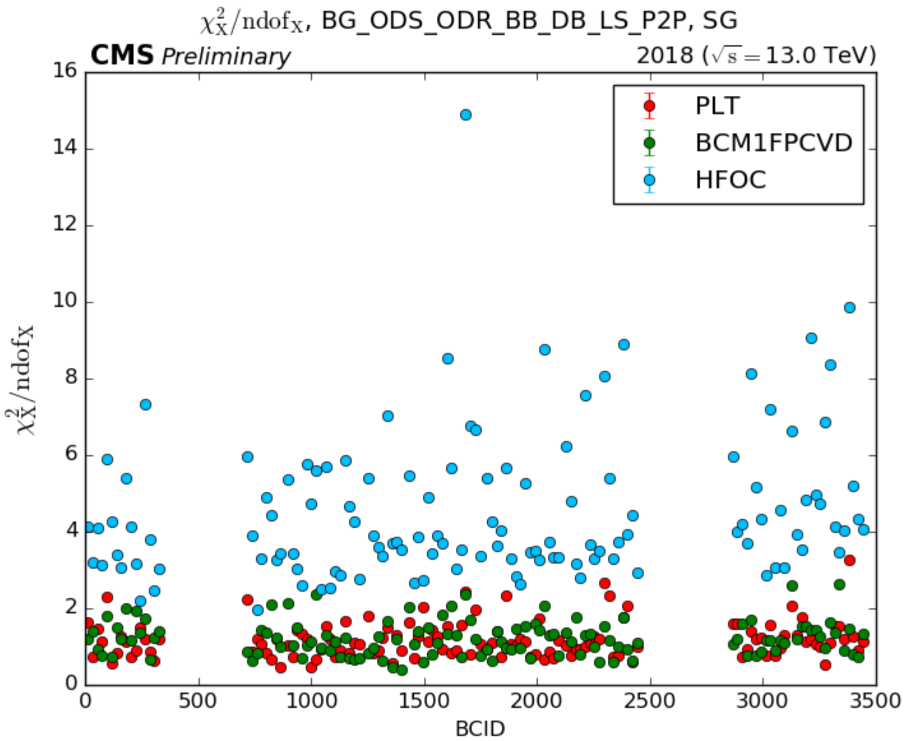

***Figure 3.4. Top**: Distribution of reduced χ^2 values (χ^2 divided by the numbers of degree of freedom) of fits including theoretical distribution individually for each detector. **Bottom**: Combined χ^2 values of all detectors. The title includes the set of corrections and fit function written using shorthand notation.*

The upper plot of figure 3.5 contains the ratio of beam current measured with FBCT summed over all bunches, and beam current measured with DCCT. The ratio provides info on possible bias of one of the beam current instruments. A constant function is fitted over all scan points to get a single estimate for the ratio. Fit parameters are included in the plot.

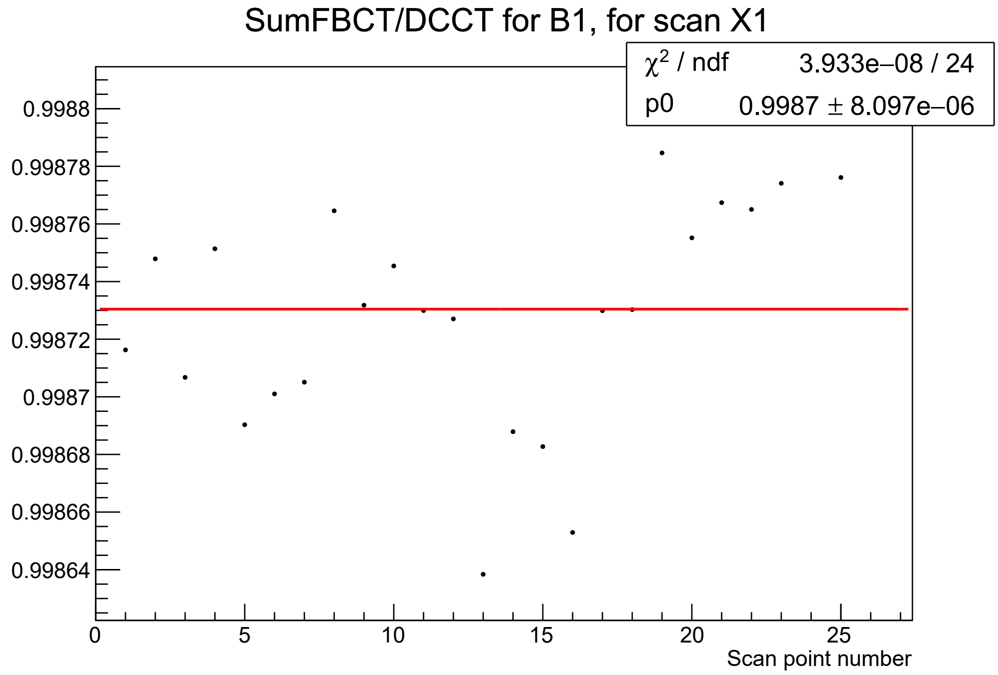

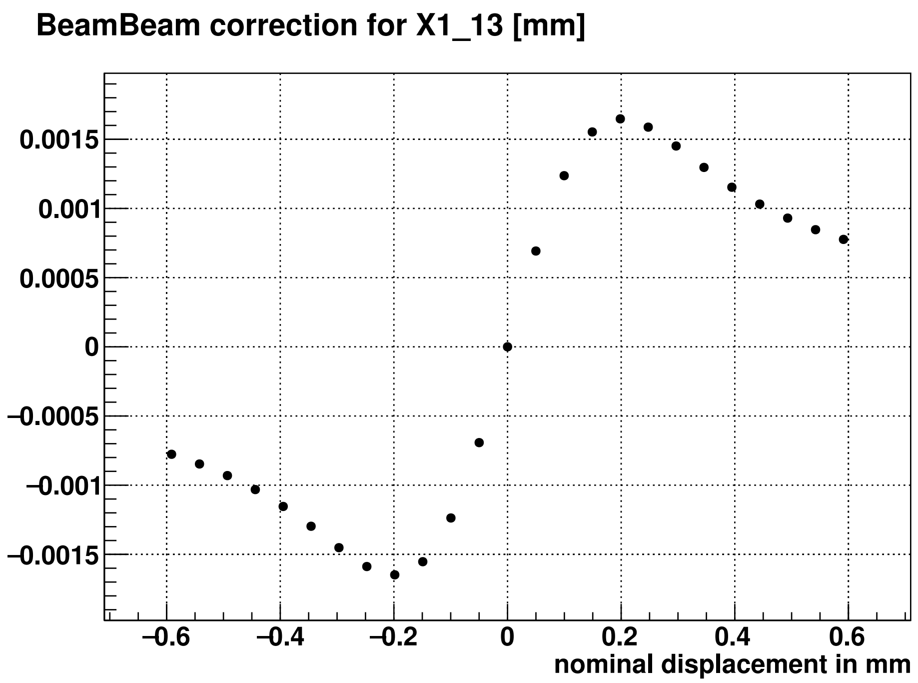

Figure 3.5. ***Top****: Ratio of beam current measured with FBCT and summed over all bunches, and beam current measured with DCCT.* ***Bottom****: Calculated magnitude of correction for beam-beam deflection, is the corresponding correction is enabled. The target BCID is visible in the title along scan axis.*

An estimation of detector visible cross section done by fitting a plane to $\mathrm{peak} - \Sigma_x - \Sigma_y$ triplets is shown in figure 3.6. Plot of Σ_x as a function of $\mathrm{peak} \cdot \Sigma_y$ is not displayed as it's qualitatively similar to the plot on the bottom.

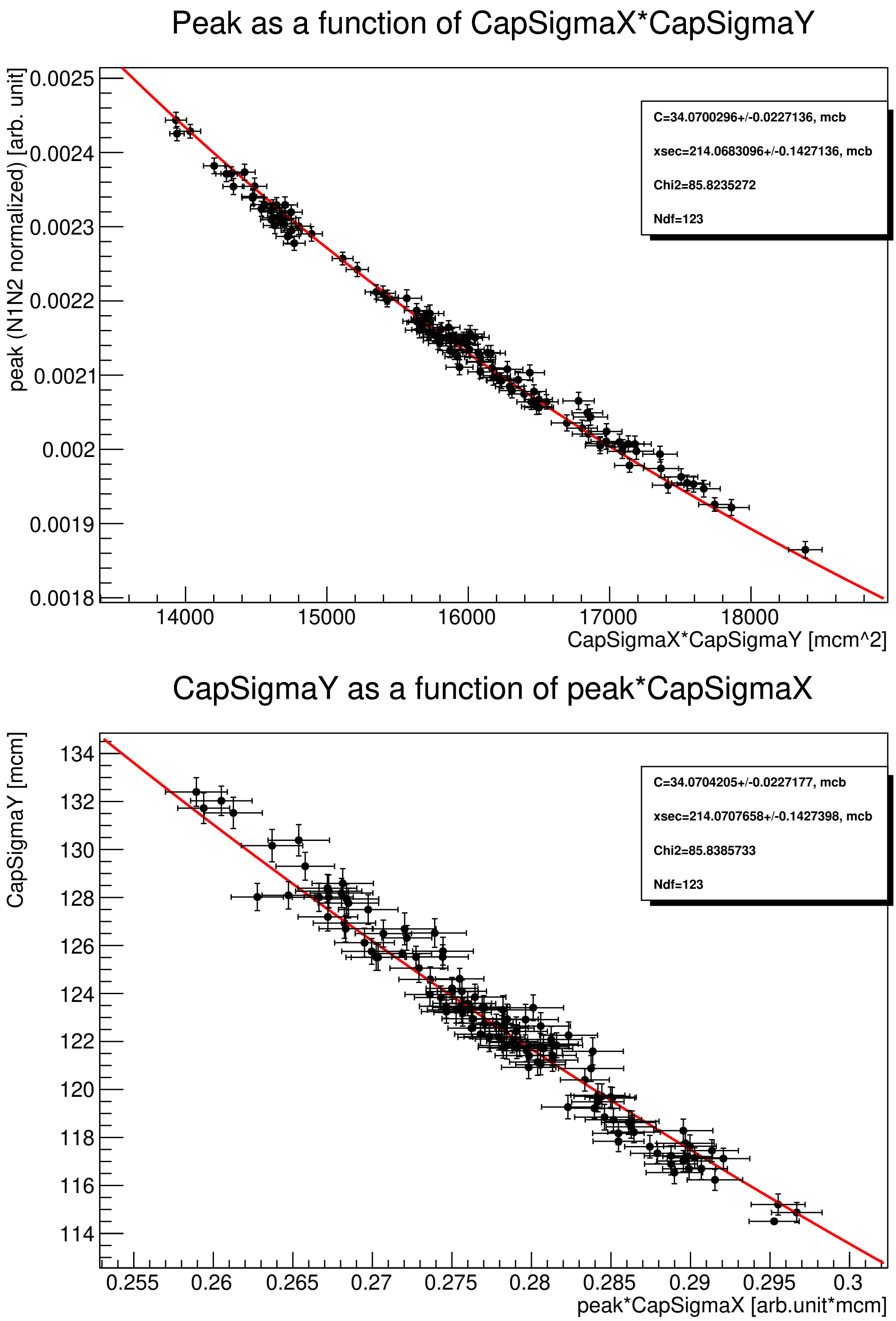

Figure 3.6. *An estimation of detector visible cross section done by fitting a plane to* $\mathrm{peak} - \Sigma_x - \Sigma_y$ *triplets.*

Framework execution flags have also been modified. The updated flags are presented below along with explanations.

-f / **--filename** Path to the H5 file to analyse

-f2 / **--filename2** Path to the file corresponding to the second scan pair, if not in the first file from -f

-ms / **--muscan** Set this flag if running on mu-scan data

-c / **--central** Folder to watch for automatic operation

-p / **--post** Post the analysis results to web server

-l / **--luminometers** Analyse a list of luminometers or leave out for default set of luminometers

-re / **--rateerror** Hit rate error formula (either *SEM* or *binomial*)

-fc / **--fitfunction** Fitting function. Use multiple fits by giving a space-separated list.

-pdf / **--pdf** Make pdf files of beam beam corrections and scan distribution fits

-s / **--summaryplots** Create some general plots about the run

--logs Save logs of the fitting procedure

-gs / **--ghostsatellite** Apply ghosts and satellites correction

-bkg / **--bkgmethod** Method to apply background correction choices.
none (default): Explicity turn off background correction
bg: Filled-unfilled and unfilled-unfilled bunch crossings
bgf: Super separation values (fixed background values)
bgfbun: Per bunch from super separation values
bgpb: Per bunch per scan point using rate of the previous bunch as background
bkskip: No background correction

-ods / **--orbitdriftsep** Apply orbit drift separation correction

-odr / **--orbitdriftrate** Apply orbit drift rate correction

-b / **--beambeam** Apply beam beam correction

-db / **--dynamicbeta** Apply dynamic beta correction

-ls / **--lscale** Apply length scale correction

-p2p / **--peaktopeak** Apply peak-to-peak correction

-xy / **--xyfactorizationbias** Create 2D graphs file of the 1D scans, used for xy factorization bias study

-fom / **--fom** Perform figure-of-merit analysis

-v / **--verbose** Set the logging verbosity

Documentation

Documentation is now centralised and distributed alongside the program code. Folder `doc` contains source code for documentation in Markdown format. Documentation is formed of three parts: a short tutorial on how to use the program, a comprehensive wiki and application programming interface (API) documentation created with Sphinx [46], a documentation tool for Python. These are proposed to replace the existing Gitlab Wiki and the tutorial now present in Google Docs service.

Serving the documentation as a part of the repository has several advantages. Most importantly, the documentation versioning now follows source code closely, and contributors are able to create a single *Merge Request* containing changes to both code and documentation. It is practical to make a separate branch of upstream code that is dedicated for a specific analysis. This allows to also have up-to-date documentation for the branched code, even though the upstream documentation is changed. Using this implementation, it is also possible to automate parts of documentation, mainly the entry points and "doc strings" of functions can be displayed to the reader, without the need to read source code. Sphinx is used to list the parameters of the main entry point of the framework, and also list the names and descriptions of all functions to a specific sub-area in the documentation. To prepare the document for viewing, it needs to be compiled using the script `scripts/CICD/buildDocs.sh`. The script is executable in LXPLUS and cmsusr environments, and it automatically installs needed packages to local folder `tmp`. Installing the dependencies to a local folder prevents the user's global Python installation from being affected. This procedure is done automatically for the latest version of the framework and is described in detail in Sec. 3.1.3.

Additionally, issue tracking is moved from the previously used Google Docs document to *Issues* tab in the GitLab repository. Issues-functionality allows linking topical discussion between GitLab users, Merge Requests and other issues while creating a valuable history for discussion about said topic, even after the issue is marked "closed".

3.1.3 Gitlab pipeline

Several challenges have been identified in the development of the vdM Framework, such as heterogeneous collection of contributors, large number of use cases and features, as well as growing number of users. An efficient development and testing workflow is highly desirable in these circumstances. During LS 2, an automated testing pipeline was implemented in GitLab alongside a documentation deployment system. The procedure is described in this chapter.

The Gitlab continuous integration and continuous deployment (CI/CD) pipeline is controlled by file `.gitlab-ci.yml`, which is located in the project root folder. Whenever changes are pushed to a protected branch in the repository, the pipeline is run automatically. This action is only triggered in protected branches, as the operations need access to various locations in the CERN network, which are provided by a CERN service account *vdmdata*. The credentials for this account are stored in protected GitLab environment variables, and unauthorised access to these should be denied. This includes running code from a third party in an environment, that has access to these credentials. Marking a branch as *protected* denies pushing changes directly to the branch, and instead a merge request is required. This prevents non-monitored code from accessing the service account credentials without acceptance from an author. Authorship is defined here as one's account having status *maintainer* or *owner* in the vdM Framework repository.

The structure of the pipeline is illustrated in figure 3.7 and explained in detail below.

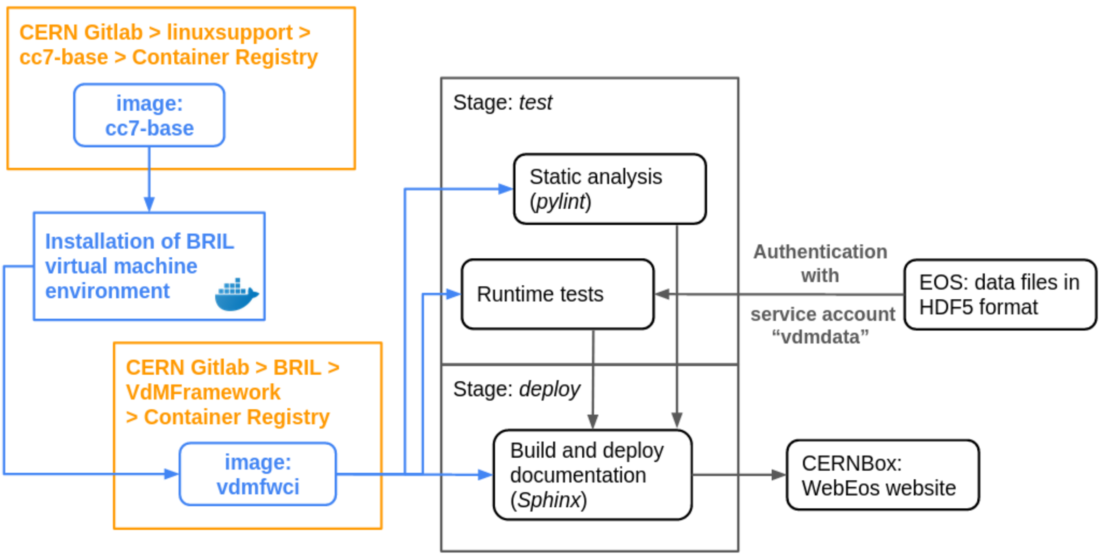

Figure 3.7. *GitLab pipeline of the vdM framework.*

First, the availability of environment variable `CERN_USER` is checked. If this variable is defined, the program has access to required data and can continue. In other cases, the program exits.

The runtime environment is then initialised by pulling a pre-built Docker image from the framework's GitLab page. Building the environment can be done using file *Dockerfile*, which also is included in the project root folder. *Dockerfile* is in this case short and displayed below in it's entirety. Lines starting with # are comments.

```
# Minimal image of CentOS7 to mimic the brilvm enviroment
FROM gitlab-registry.cern.ch/linuxsupport/cc7-base:latest

# Metadata
LABEL Name=vdmframework Version=1.0.0

# Pre-install these packages
RUN yum install -y root xrootd-client git
```

Next, path for Python executable and SSH options for connecting to other CERN machines are initialised, and stage *test* with static analysis is started. A special GitLab runner is reserved by using tag `cvmfs`, which has access to the file system where BRIL Python environment *Brilconda* is located in. Python executable is set to point to this, and additional packages are installed via pip. The additional packages are installed to folder `tmp` alongside other project files in order to keep them separate from the user's local packages. A Python virtual environment was considered to encapsulate the Python dependencies, but this was deemed to be incompatible with Brilconda. Next, static analysis is conducted using script `src/scripts/CICD/doStaticAnalysis.sh`. The static analysis tool can be used also outside GitLab by running this command from the command line. This does not require further authentication besides access to either LXPLUS or CMS machines. Output of static analysis is lastly saved to Gitlab artefacts, which allows storing and inspecting the output in the case of an error being detected. If this is the case, the program does not proceed to the final step *deploy*, but instead exists and a notification about test failure is displayed in the GitLab web page. Failing a static analysed test is at the moment determined by Pylint reporting at least one level "error" fault in the source code. Pylint is capable of reporting also less severe faults but they are at the moment ignored because of the vast amount of "code smells" detected.

A runtime test is performed in parallel with static analysis. After the authentication step, data files are fetched from EOS and copied to a local folder. GitLab runner with cvmfs access can copy files from EOS using XRootD [47], an open source framework commonly used in HEP data access. After data retrieval, the test script `scripts/CICD/doTestRuns.sh` is run in folder `src`. Also this command is possible to be run outside GitLab.

If the two tests are successful, the pipeline proceeds to stage *deploy*: the documentation is built and deployed to a CERNBox website. Material for the documentation is stored in the same repository as source code and can be trivially accessed by the runner. API documentation is created from source code using Sphinx, a widely used software utility for generating documentation from Python. A set of hand-written markdown pages are also included, which contain a tutorial for the framework, as well as an extended reference document. A web page with documentation about the framework is created when script `scripts/CICD/buildDocs.sh` is run in folder `src`. If changes are made to documentation, it is useful to build the document locally using the script to be certain no errors are raised. After the document is successfully built, the resulting folder will be copied to a specific folder in EOS which is exposed to the public, and can be accessed with CERN credentials [48].

3.2 BRIL data acquisition system

The BRIL data acquisition system (BRILDAQ) is a data transfer platform used by all BRIL subsystems. It is responsible for storage and publication of luminometer data, and recording data from numerous other LHC systems published through Data Interchange Protocol (DIP). Minor changes have been made to the program logic related to storing data from vdM scans during LS2. A general description of the current state of the system is described here.

BRILDAQ is implemented using XDAQ software environment and the CMS Run Control and Monitor System (RCMS). XDAQ (read *cross-daq*) is a general framework for distributed data acquisition written in C++, capable of providing near real-time information exchange for several loosely coupled software components using event-driven architecture. RCMS is a collection of software and hardware components responsible for monitoring and configuring the CMS experiment during data taking. RCMS provides a web-interface to configure detectors and data taking, as well as monitor the status of CMS systems. BRILDAQ is built as a separate system from CMS central daq, which allows operation independent from CMS. The BRIL computer cluster contains around 20 running processes, with one process dedicated to monitoring vdM scan status at CMS to trigger scan-specific data taking and logging of the current vdM scan state. The scan state is acquired from CMS central systems using DIP.

The convention of LHC signalling the current scan state was updated during LS2. Most importantly, the path of the DIP subscription was changed from
`dip/acc/LHC/Beam/AutomaticScan` to
`dip/acc/LHC/Beam/AutomaticScanIP<IP number>`, now including separate publications for each IP. The relevant topics of this new publication are displayed in table 3.1.

Table 3.1. *Contents of $dip/acc/LHC/Beam/AutomaticScanIP5$ relevant to vdM analysis and file creation.*

Quantity	Type	Explanation
Acquisition_Flag	bool	Whether the beams are not being adjusted
Active	bool	Whether a scan procedure is ongoing
Experiment_Message	string	Most often a message related to the current data taking period
IP	int	Deprecated (previously used to distinguish between scans at different IPs)
LumiScan_Status	string	Either "STANDBY" (vdM data taking is paused) or "ACQUIRING" (data taking is in progress)
Nominal_Separation	double	Magnitude of beam separation
Nominal_Separation_Plane	string	Name of the scanning plane. Possible values are "CROSSING" (x-plane at CMS), "SEPARATION" (y-plane at CMS), MIXED (beams moved in both planes) and NONE (no scan in progress)
Read_Nominal_Displacement_B1_sepPlane	double	Current displacement of beam 1 in separation plane
Read_Nominal_Displacement_B1_xingPlane	double	Current displacement of beam 1 in crossing plane
Read_Nominal_Displacement_B2_sepPlane	double	Current displacement of beam 2 in separation plane
Read_Nominal_Displacement_B2_xingPlane	double	Current displacement of beam 2 in crossing plane
Step	int	Scan step number
Step_Progress	int	Time in seconds until the end of scan step
acqStamp	long	Timestamp in Unix time

Flag "Active" in the table above was added during LS2 to be a general indication to signal an ongoing scan. BRILDAQ has been adapted to accommodate the new flag, triggering file handling when the flag turns *False*, indicating the end of a scan.

3.3 BRIL data aggregation system

Beside analysing the data collected to measure the luminosity, accessing and visualising a vast amount of information related to vdM scans at CMS was considered to be another challenging task during Run 2 data analysis. The information about the type of data analysed is in fact not stored in a single place that is easily accessible, but rather scattered in multiple independent sources. Moreover, in some cases, qualitative information about the status and history of a given sub-period of data taking was missing. In this section, a new software tool to access vdM scan information is proposed, including information added at human level to record specific features of the data needed to understand them during its analysis. The purpose is to have a rapid and effective understanding of the data and finalise the task of luminosity measurement more rapidly and effectively.

BRIL Data Aggregation System (BRILDAS) provides an effortless way to access the CMS Online Monitoring System (OMS) [49] and notes made by the scan experts at CMS. Relations of systems essential to BRILDAS are described in figure 3.8 and further explained below the figure.

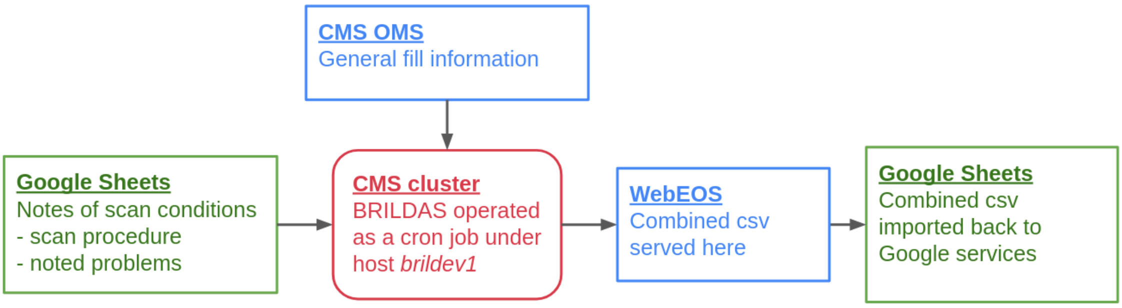

Figure 3.8. *Relations of systems essential to BRILDAS.*

- **Google Sheets**: A commercial spreadsheet editing and distribution service.
- **CMS OMS**: A portal offering information on CMS operation.
- **CMS cluster**: A network of computers running in an intranet exclusive to CMS, with access to data output from CMS subsystems. Hostname *brildev1* refers to a machine designed to run the vdM framework when new data is available.
- **webEOS**: A website hosting interface provided by CERN, where website contents are stored in EOS. [50]

BRILDAS operates by first acquiring information inputed by BRIL operators, which is stored as a .csv file in Google Sheets and represents a database of user added information. This setup was chosen to provide an easily approachable user experience with versatile access management. The file received from Google Sheets contains information listed in table 3.2.

Table 3.2. *Quantities available in the scan database.*

Quantity	Explanation
fill	Fill number
filename	Filename of the H5 file in EOS
name	Identifier for the scan type and number, for example "vdM2"
scan_points	Number of scan points
scan_range_sigma	Scan width expressed in convoluted beam widths
scan_type	List of axes the scan was performed in, most common is "XY"
valid	Boolean flag to notify if the file is unusable, typically because the scan has been split into two files which have been joined into a large, combined file. In this case one should use the combined file for analyses.
colliding_bcids	List of colliding BCIDs
non_colliding_bcids_b1	List of non-colliding BCIDs in beam 1
non_colliding_bcids_b2	List of non-colliding BCIDs in beam 2
notes	Additional notes related to scan
reprocess_directory	Directory name, that indicates the location for an enhanced/corrected version of the file.
folder	Folder where the H5 file is, respective to the data root explained below.

In table 3.2, the H5 files are stored in EOS Open Storage (EOS) system, a CERN data storage infrastructure. The files are saved under path `/eos/cms/store/group/dpg_bril/comm_bril/vdmdata/` in a deterministic way, which allows to infer the absolute path of the original file and derived versions of it using the database. The desired folder structure is `<root>/<year>/<edition>/<fill number>/<H5 file>`. Original data will be stored as `edition` version "original". This path structure can be used in combination with data from the scan table to find a folder with data files corresponding to a specific scan.

The previously described table will be supplemented with info from CMS OMS, to which the scan table is joined using a *right join* operation while using the fill number as the join key. The operation provides the desired table, as there can be several scans in one fill, but a single scan can only belong to one fill. We note that some elements from OMS table may be duplicated, as info for a particular fill can be associated to multiple scans. This redundancy, beside not being a problem, is in some cases inevitable as in order to define the key for accessing the user defined database one has already to add information that can be found in OMS as well. The data fetched from CMS OMS is described in detail below.

Table 3.3. *Quantities available in "Fill Summary" tab of CMS OMS.*

Quantity	Explanation
fill_number	Fill number
first_run_number	First run number
last_run_number	Last run number
intensity_beam1	Beam 1 intensity [10^{11}]
intensity_beam2	Beam 2 intensity [10^{11}]
crossing_angle	Crossing angle [µrad]
start_crossing_angle	Crossing angle in the beginning of the fill [µrad]
stop_crossing_angle	Crossing angle in the end of the fill [µrad]
energy	Target beam energy [GeV]
b_field	Strength of the magnetic field at CMS [T]
beta_star	β* [cm]
beta_star_start	β* at the beginning of the fill [cm]
beta_star_stop	β* at the end of the fill [cm]
peak_lumi	Highest instantaneous luminosity measured during fill [10^{30}cm^{-2}s^{-1}]
delivered_lumi	Integrated stable luminosity delivered by LHC [µb^{-1}]
recorded_lumi	Integrated stable luminosity recorded by CMS [µb^{-1}]
efficiency_lumi	Efficiency by luminosity
era	Name of data taking era
fill_type_party1	Particle type in beam 1
fill_type_party2	Particle type in beam 2
injection_scheme	Identifier telling the amount of bunches are injected and in which IPs they collide at
bunches_colliding	Number of colliding bunches
bunches_beam1	Number of bunches in beam 1
bunches_beam2	Number of bunches in beam 2
efficiency_time	Efficiency by time
downtime	Downtime during fill
start_stable_beam	Time when stable beam was declared
end_stable_beam	Time when stable beam was declared
start_time	Fill start time
end_time	Fill end time

Quantity	Explanation
duration	Fill duration
peak_pileup	Peak pileup (maximum number of concurrent events)

All of the quantities mentioned in the table are given over whole fill.

4. LUMINOSITY MEASUREMENT USING OCTOBER 2021 BEAM TEST DATA

After the maintenance period LS2, the LHC was brought to operation again on 19th of October 2021, when the first pilot beams were successfully injected during the October 2021 beam test. The first test collisions took place a week later, and collisions with a stable beam, used during data taking for physics purposes, were declared on 27th of October [51]. The test period lasted until 1st of November, and contained a total of 15 vdM scans at CMS which were used to estimate the σ_{vis} of the PLT and BCM1F detectors. The HF luminometer was not operative during this period. In this chapter, we discuss the results obtained for the luminosity calibration of which I have been a main contributor.

4.1 The vdM scans

The vdM scan program is summarised in table 4.1. The fill numbers in the table are referring to LHC numbering, which, as we can see, was not necessarily incremented when a new beam was injected. This is, for example, the case for fill number 7515, which technically consists of 2 separate fills, with scan 1 belonging to a different fill than the following two. The column *scan points* refers to the amount of points where the beam overlap is measured and *scan width* is the maximum separation between beam spots. Notation B_i refers to beam i. The last three columns contain info about special circumstances for that specific scan and are elaborated below.

During the first three scans, the timing between beams was off by about 3 ns, which caused the collisions at CMS to be displaced by 12.5 meters from the centre of the detector. The effect was observed by the Beam Pickup Transformer (BPTX), a BRIL subsystem designed to measure beam timing, phase, bunch length and intensity. Timing of the beams was adjusted on October 28, bringing the time difference between beams to 40 ps, corresponding to roughly 1 mm distance from the centre of the CMS detector. The period of adjusting beam timing (*cogging*) is illustrated in figure 4.1.

Incorrect beam timing makes estimation of background rate problematic, and effectively

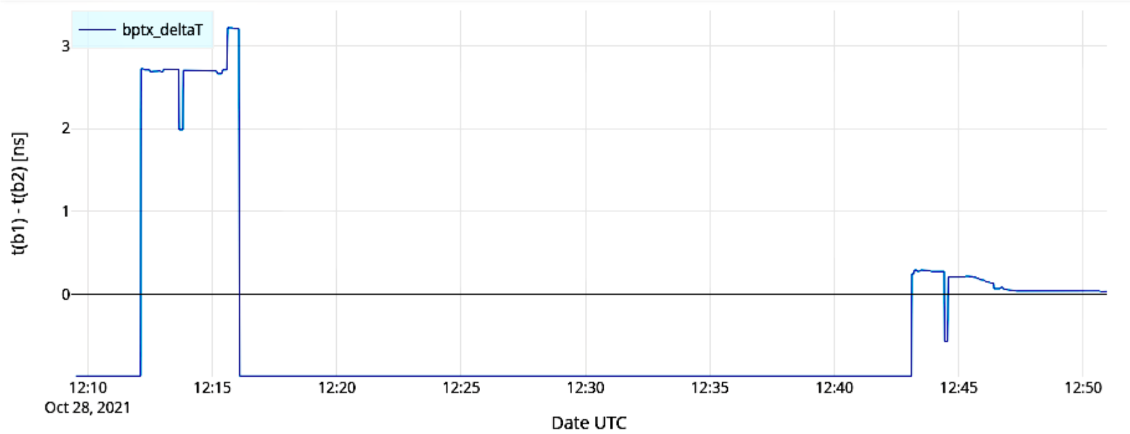

Figure 4.1. *Time difference between beams recorded by the Beam Pickup Transformer during cogging adjustment, viewed from the BRIL web monitor. Value of -0.99 is displayed when no beam is present.*

prevents correcting BCM1F rates used for luminosity measurement against background signal in a way identical to the treatment of other scans. There were also adjustments being done to make properly functioning both BCM1F and PLT detectors during fill 7515, which introduces additional uncertainty to the results. Because of these shortcomings, the first three scans are not considered in this study. Furthermore, fill 7525 did not contain any non-colliding bunches, which prevents background correction with the preferred method.

The scan width was initially 4 σ (four nominal beam widths) but was lowered to 3 σ during fill 7517, because of low perceived hit count on large separations. A low amount of inelastic collisions was expected, as the the filling scheme for beam test consisted only of two to three colliding bunches colliding at a relatively low energy. This is more than fifty times less colliding bunches than in typical van der Meer scans. The scan width of 3 σ was used for the rest of the beam test. The number of scan points was 9 until the last fill, where it was increased to 15 in attempt to improve the quality of the fit to the beam overlap.

4.2 Measurement of visible cross-section for luminosity calibration

Figure 4.2 displays the initial analysis results for visible cross section of BCM1F detector using three different configurations. BCM1F is more prone to background signals than PLT, which introduces a need to address the background contribution. Results received using background corrected rates with a single Gaussian fit function are displayed, as well as results for non-corrected rates with a model that sums single Gaussian + constant value to characterise the background. Both of these provide a method to address the background signal, as the constant term in single Gaussian + constant fit is effectively

Table 4.1. *Scan conditions at the CMS experiment during October 2021 beam test.*

#	Fill	Scan points	Scan width (σ)	Colliding BCIDs	Non-colliding bunches (B_1)	Non-colliding bunches (B_2)	BCM1F issues	PLT issues	LHC issues
1	7515	9	4	1, 1786	895	892	Channel timings	BCID shift	Displaced collision
2	7515	9	4	1, 1786	895	892			Displaced collision
3	7515	9	4	1, 1786	895	892			Displaced collision
4	7517	9	4	1, 1237	895, 2131	1786, 3022			
5	7517	9	4	1, 1237	895, 2131	1786, 3022			
6	7517	9	4	1, 1237	895, 2131	1786, 3022			
7	7518	9	3	1, 1237	895, 2131	1786, 3022		BCID shift	
8	7520	9	3	1, 1237	895, 2131	1786, 3022			
9	7521	9	3	1, 1237	895, 2131	1786, 3022		BCID shift	
10	7525	9	3	1, 892, 1786					
11	7526	9	3	1, 1237	895, 2131	1786, 3022			
12	7527	9	3	1, 1237	895, 2131	1786, 3022			
13	7531	15	3	1, 1237	895, 2131	1786, 3022			FBCT shift
14	7531	15	3	1, 1237	895, 2131	1786, 3022			FBCT shift
15	7531	15	3	1, 1237	895, 2131	1786, 3022			FBCT shift

subtracted from the measurements.

Figure 4.2 shows generally good agreement between the background corrected values and results acquired with a fit function with single Gaussian + constant. Visible cross section obtained with these is generally lower, than non-corrected one. This agrees with the assumption that non-corrected values include some noise. An apparent, unexpected drop in σ_{vis} can be seen between scans 7521 and 7525. This required further investigation, and the suspected cause was deemed to be the detector configuration in combination with timing adjustments. A slight downward trend in σ_{vis} can be seen across fills 7517 and 7531, as luminosity gets lower. These were the only fills apart from 7515, where there was multiple scans conducted in a single fill. This is a sign of non-linear detector response, and it does not seem to be as apparent in corrected results than in non-corrected ones.

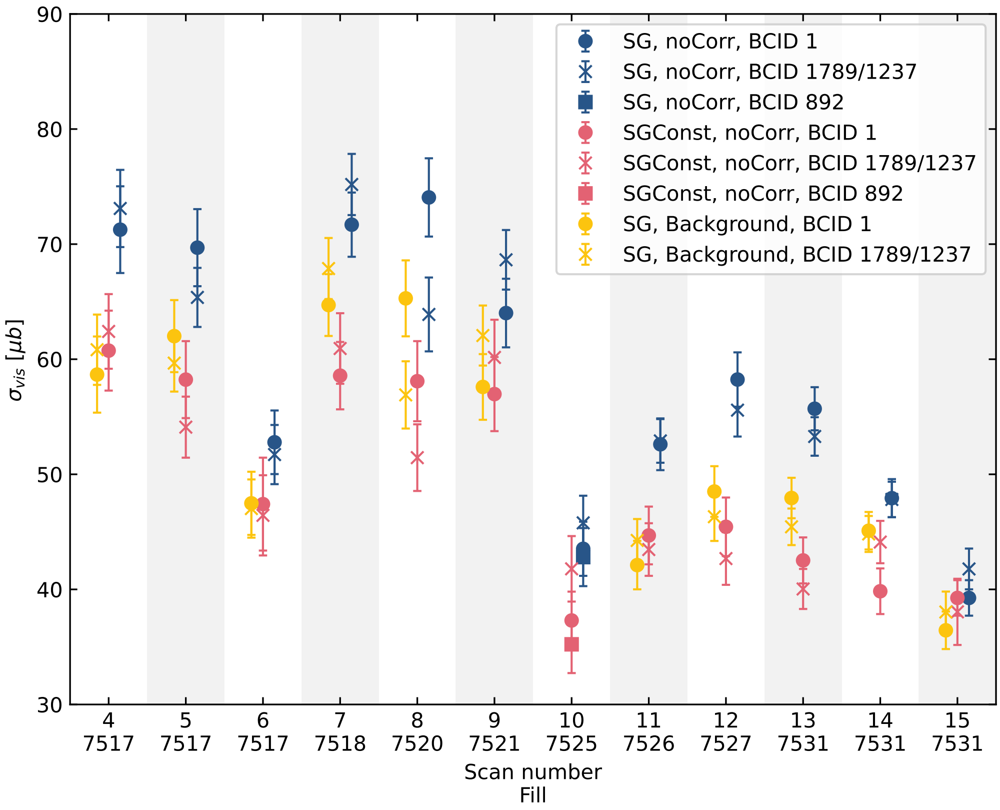

Figure 4.2. *Initial values for the visible cross section of the Fast Beam Condition Monitor.*

Timing of the PLT clock was not correctly synchronised with the corresponding bunch during scans 1, 7 and 9. This required manual operations to the data, as the measured hit rates were assigned to incorrect BCIDs. It was noticed, that the BCIDs with high recorded hit rate (a property of colliding bunches) were at a specific distance from nominally colliding bunches. This indicates that the timing of the PLT detector was off by this amount. The offsets determined by manually inspecting the rates in scans 1, 7 and 9 were 2376, 3168 and 3377, respectively. Correction for this shift was included in the vdM framework, which allowed to determine the visible cross section for the PLT. Without the correction, a value of 0 is obtained as the method used in the framework measures the detector hit rate only from nominally colliding bunches. Figure 4.3 displays the initial results for the PLT, where previously described correction has been applied.

The PLT shows generally the same behaviour as BCM1F, without an apparent drop between scans 7521 and 7525. The lowest recorded luminosity was in fill 7517 which belongs to the "first group", and values determined from scan 13 are approximately in the level of early scans. Detector-specific issues were observed across the beam test, and they are described in following sections.

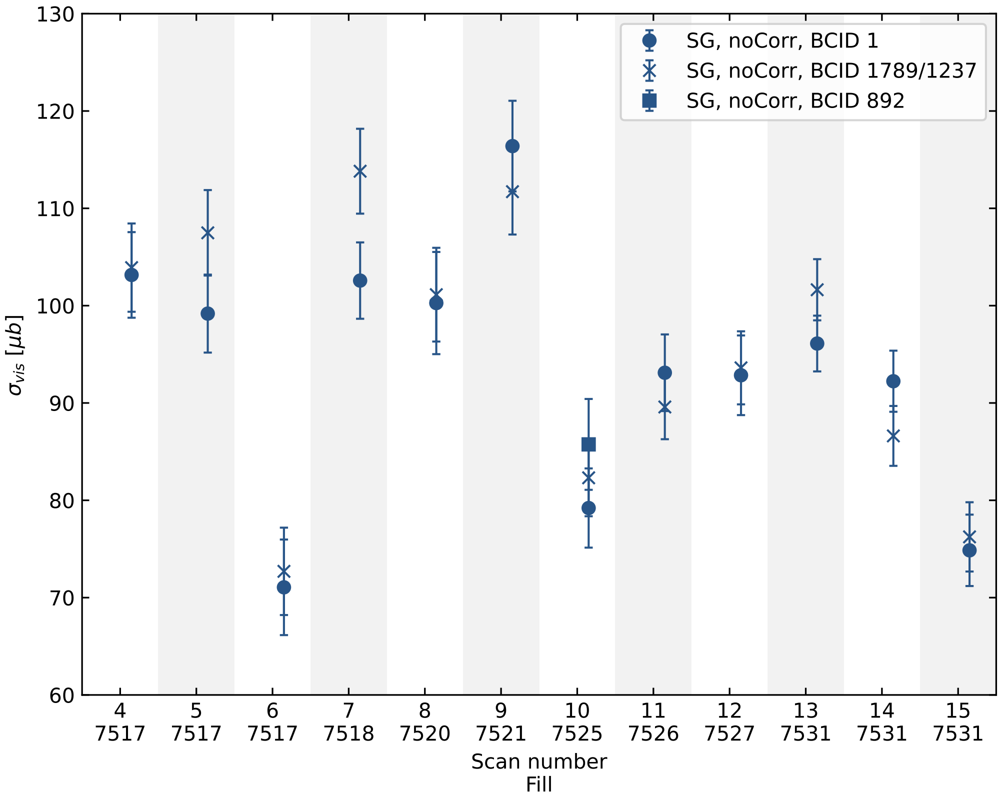

Figure 4.3. *Initial values for the visible cross section of the Pixel Luminosity Telescope.*

4.3 PLT channel timing

Hit rates measured by the PLT are assigned to particle bunches using a clock, which has to be fine tuned to have the correct BCID assigned to the corresponding bunch. Timing is adjusted separately for each channel. Accuracy of channel timing is estimated here by determining the fraction of rate measured in filled bunches compared to rate in all bunches. A possible timing misalignment causes rate to be assigned to an incorrect BCID, lowering this metric. In an optimal situation, the fraction is close to 100%. Certain systematic effects however, like the afterglow effect, introduce a rate reading to unfilled bunches. Afterglow is typically a sub 2-percent effect [52] and reduced by the triple coincidence property, causing it to be insignificant when determining the channel offsets on whole-BCID granularity. Timing of PLT channels was adjusted throughout the beam test, and needs to be compensated when determining the σ_{vis} of an optimally configured PLT. It is worth highlighting, that determining the visible cross section is done using colliding bunches, but actual luminosity is measured using rates of all bunches. Hence, to accurately estimate the luminosity during beam test, the misalignment has to be corrected. Per-channel rates for PLT are stored by BRILDAQ whenever a scan is in progress at CMS, but not during normal physics operation. Fraction of rate in filled bunches (noted here as R_f) for non-corrected beam test data is displayed in figure 4.4. Values are displayed separately for each channel, and an average of them is displayed in the last column.

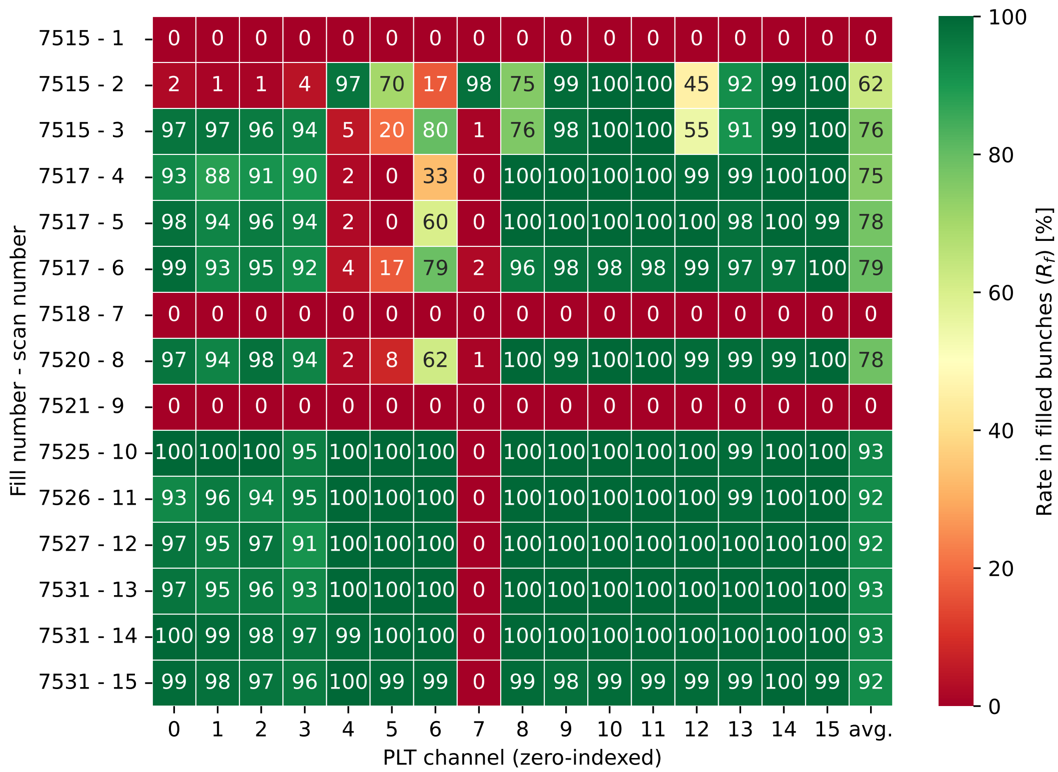

Figure 4.4. *Fraction of hits detected by the Pixel Luminosity Telescope that are produced by colliding and non-colliding filled bunches (R_f).*

It can be seen from the figure, that during some scans the timing of all channels was incorrect, referred to as a *global shift*, which entirely prevents detector being used for per-bunch luminosity measurements. This issue can be compensated by introducing a manual offset of Δi to BCID i when determining the σ_vis, yielding rate R(i +Δi) where R(i) is the measured rate for BCID i. This however does not guarantee all channels to be synchronised, and an offset that provides the highest overall rate for the detector was chosen. Channels should in general be analysed individually, as timing adjustment should be done individually for each channel. The offset can be determined using rate in R_f as a metric to test, if the channels are well synchronised, a large value of R_f meaning the channels are well aligned. This task can be formulated as an optimisation problem

$$\Delta i = \arg\max_{j} \sum_{\text{BCID}=1}^{3564} \mathbf{m}[(\text{BCID} + j) \bmod 3564] \cdot \mathbf{R}(\text{BCID}), \tag{4.1}$$

where mask $\mathbf{m}$ is a row vector of length 3564 with 1 in position m if bunch m is filled and 0 if the bunch is unfilled, and R is a column vector with length 3564 and follows the same convention as described earlier. This definition for offset causes it to be defined as a non-negative number implying the channel to always be behind the optimal timing, even though the channel may in reality be ahead of the correct value. Because of the circular nature of the LHC, it is not possible to make a distinction between shifts of j and $j + n \cdot 3564$, where $j, n \in \mathbb{Z}$ using this method. Assigning the corrected rate to each BCID is however not affected by this phenomenon, as it is apparent from Eq. (4.1).

The BCID mask $\mathbf{m}$ is available in the same H5 files which contain PLT channel rates, making it straightforward to access. The offsets determined using this method are displayed in figure 4.5.

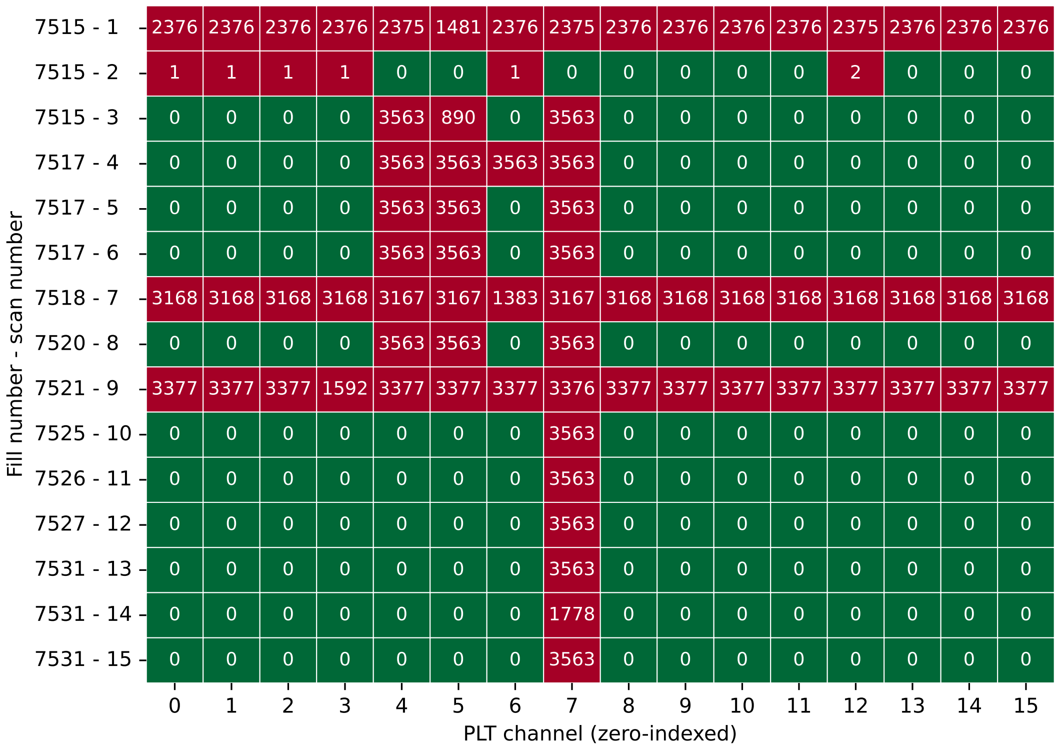

Figure 4.5. *Channel offsets of the Pixel Luminosity Telescope. Channels with a misalignment of least one full BCID are coloured red.*

Knowing the offsets makes it possible to introduce a corrective shift of $-i$, which compensates for misalignment in BCIDs. The resulting values of R_f corrected with this method are displayed in figure 4.6.

It is apparent, that R_f is in many cases far from 100% even after introducing a shift. This only affects certain channels, so it is justified to assume this to be caused by a sub-BCID misalignment, where a fraction of rate of certain bunch is spread to the neighbouring one. Based on this study, the effect is more prominent in the first half of the beam test, where up to 50% of rate is assigned to unfilled bunches after correction. It can be also determined, that the afterglow effect is negligible as $R_f \geq 99.5\%$ in some cases.

There are several approaches addressing a sub-BCID shift when determining the σ_{vis}

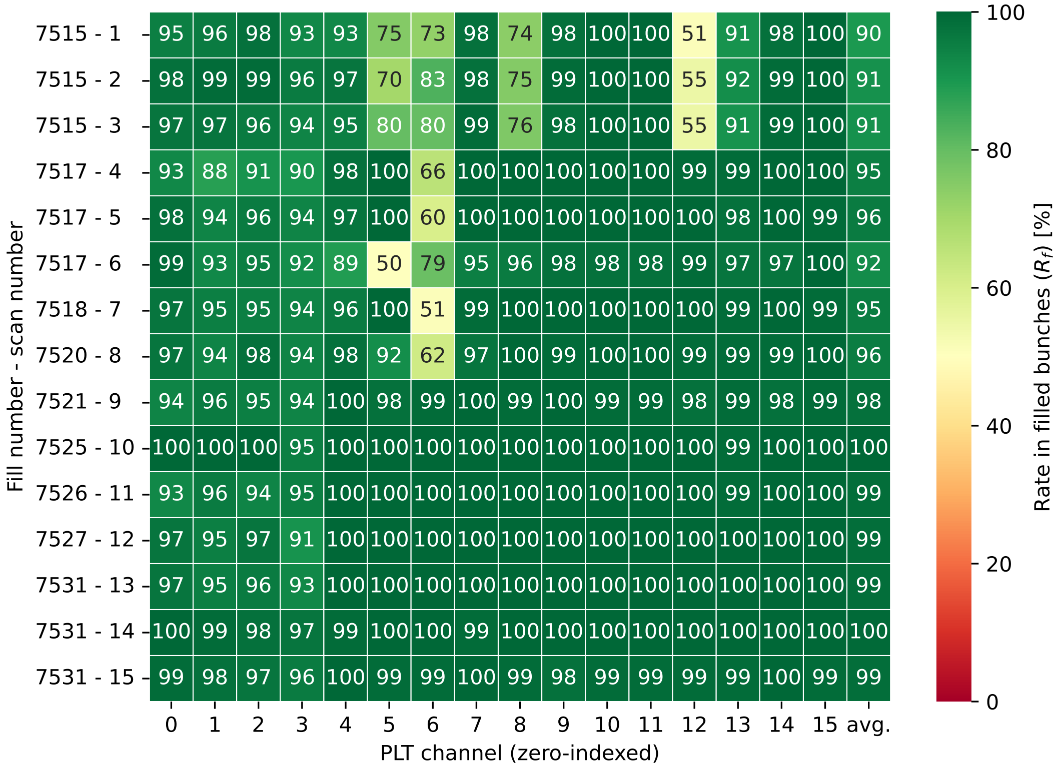

Figure 4.6. *Fraction of hits detected by the Pixel Luminosity Telescope that are caused by colliding and non-colliding filled bunches* (R_{f}) *after correcting channel alignments using algorithm 4.1.*

for a correctly configured detector. A naïve approach is to use values in the average column to assign an efficiency factor with magnitude of $1/\overline{R_f}$. This method provides reasonable results in cases where the offset does not cause the rate of any filled bunch to be assigned to a colliding bunch. This can be verified by comparing the determined offsets with the LHC filling scheme. It is noted, that rate from filled bunches is not assigned to colliding bunches during the beam test. Furthermore, the rate "missing" from colliding bunches is moved to non-colliding ones. This causes a seemingly higher background rate reading, which introduces a bias to background estimation and possible correction to background hit rates. In case of the PLT detector, the triple coincidence property causes the background rate to be minimal making this method viable. The average rate over channels displayed in figure 4.6 shows at least 98.5% of measured rate to belong to colliding bunches in the last six scans, indicating a relatively low background signal as the background rate limits how large the fraction may be. The visible cross section of PLT corrected utilising this approach is displayed in figure 4.7.

It can be seen from the figure, that the corrected visible cross section of PLT is increased for scans in early fills, while the latter scans stay relatively same. It is worth noting, that the third scan of fill 7517 yields results comparable to the last scan of fill 7531. The

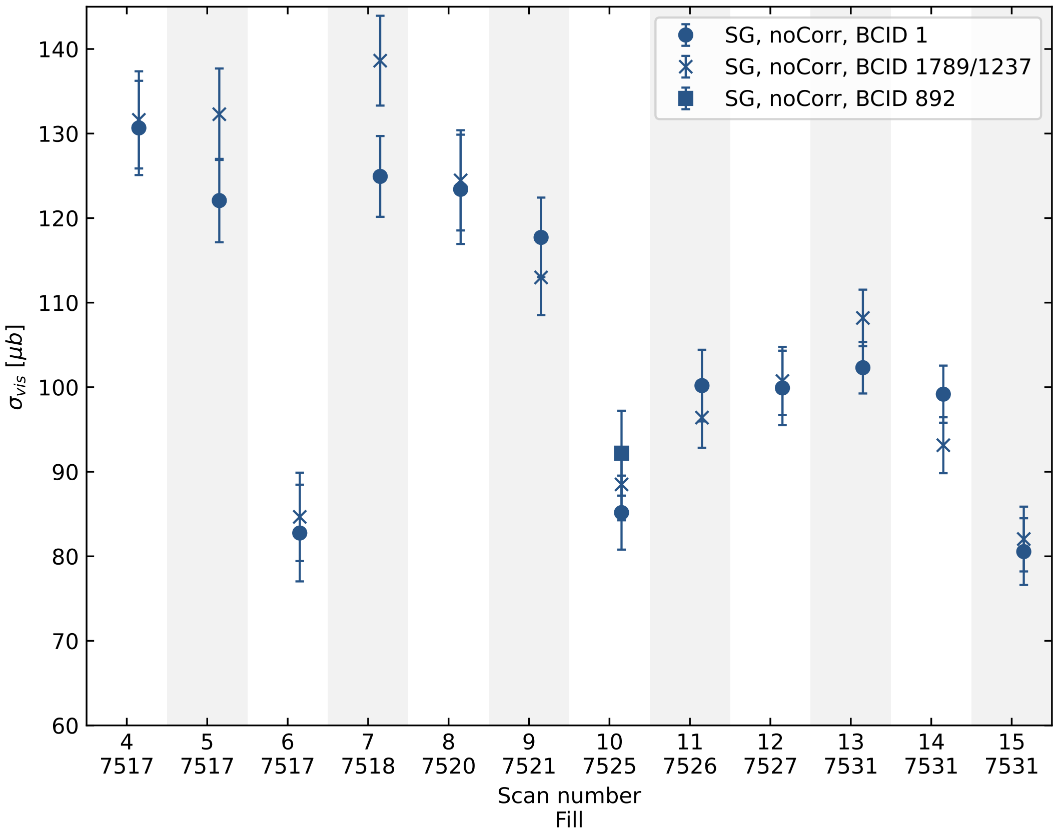

Figure 4.7. *Visible cross section of the Pixel Luminosity Telescope, after correcting for timing misalignment by multiplying the hit rates by the ratio between corrected and uncorrected values of rate in colliding bunches.*

luminosity is notably low during these scans, as they are performed near the end of a fill, which suggests that the change in visible cross section could be caused by scan conditions, rather than the detector.

We note that a method alternative to the one previously described is possible, as one might take the corrected data and add the rate in neighbouring bunches to the rate in filled bunches. The downside of this method is the requirement of access to the corrected data, but it can be applied in case of the rate of a filled bunch being shifted to the place of a colliding BCID. Another downside is the assumption, that background contribution as well as detector afterglow are insignificant.

4.4 BCM1F µTCA commissioning

The µTCA readout of BCM1F was still in commissioning during the beam test period, and two separate challenges were present in both of the BCM1F readout systems during the beam test. Regular data-taking from µTCA back-end system was prevented because of issues with orbit clock, which requires to re-bin the data into correct time slots. The RHU readout depicted an unexplained drop in visible cross section for BCM1F, which was hypothesised to be caused by the read-out system itself. Re-binning of BCM1F data was conducted for scans 8–15 by the detector team and the visible cross sections are compared in figure 4.8 using either single Gaussian fit with background correction or single Gaussian + constant fit without corrections. Re-binning involves great effort and it was not performed for the very first scans, as they are not considered as reliable as the later ones. It can be seen from the figure, that the readout systems agree within uncertainty

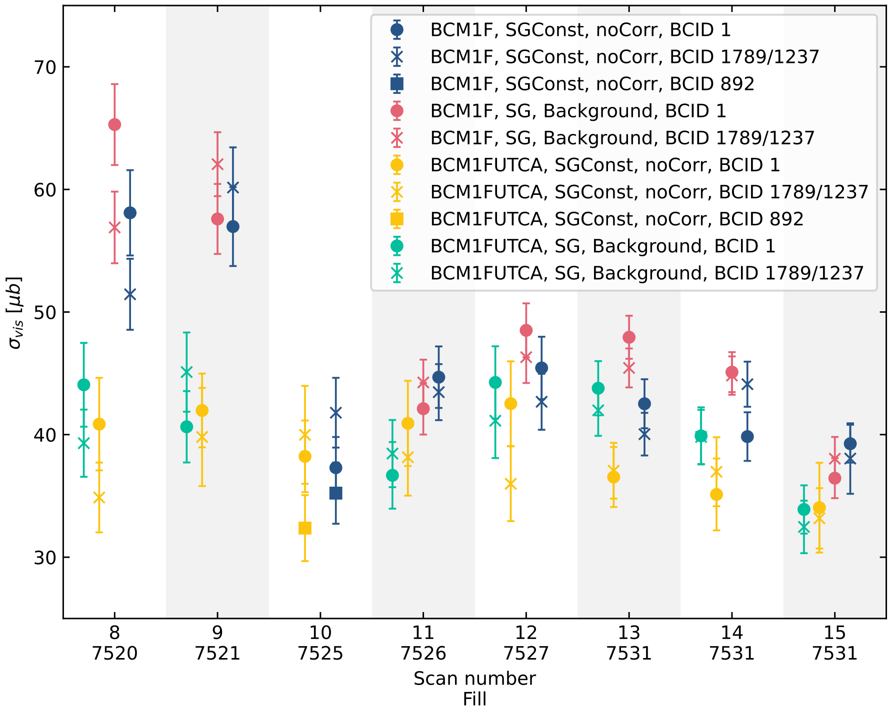

Figure 4.8. *Comparison of the visible cross section of the Fast Beam Condition Monitor, calculated with data from different backend systems. BCM1F stands for the RHU readout system and BCM1FUTCA the μTCA readout.*

for scans 10-15, but not for scans 8 and 9. This indicates a problem within the RHU system. The consistency in later scans demonstrates that the orbit clock misalignment in the µTCA readout can be convincingly overcome by re-binning the data.

4.5 Beam test conclusions

This chapter has summarised the results on sigma visible measurement obtained during the 2021 October beam test. The BCM1F and PLT luminometers were used. Both detectors have been re-built during LS2 and used for the first time. Despite being a commissioning data taking for the new detectors, we were able to finalise the luminosity calibration, benefiting from an improved vdM framework that allowed for an immediate and robust data analysis.

5. TIME EVOLUTION OF CONVOLUTED BEAM WIDTH

A challenge associated with van der Meer scans is the property of measuring convoluted beam widths one plane at a time. This creates a potential source of inaccuracy to the results, as the quantity measured first has a chance to evolve by the time the other one is evaluated. In this chapter, the effect of beam width evolution to σ_{vis}, which I have carried out for the first time for precise luminosity measurement of Run 2 data, is presented. Such luminosity measurements aim to achieve uncertainty below 2%.

5.1 VdM scans used for studying convoluted beam width effect

The study focuses on the data collected during scans in fill 6868. Taken place during Run 2, fill 6868 followed a filling scheme optimised for van der Meer scans and a significant amount of machine time was dedicated to them, which allows data from that fill to be used for high precision luminosity measurements [53]. Several different types of scans were conducted during that fill, and two different types are utilised in this study: *normal vdM scans* and *imaging scans*. A normal van der Meer scan involves scanning the beams simultaneously over each other, whereas during an imaging scan, one of the beams is kept stationary and the other is moved over it. Both of these are appropriate for determining the convoluted beam width.

Time differences between corresponding scan points between the planes in fill 6868 were between 18 and 26 minutes, depending on the scan type used. Inconveniently, the scans designed to extract an accurate value for beam parameters use a higher amount of scan points, which makes them take longer and therefore prone to suffering more from this phenomenon. Scans at CMS during fill 6868 were conducted in two sets, with several hours between them.

5.2 Methods to evaluate the effect

The evolution of quantities is estimated in two different batches. A linear fit is made to the convoluted beam width (Σ) and peak in x and y dimensions separately for the two periods. An example collection of fits estimated from the second period is displayed in figures 5.1 and 5.2, while the complete set of fits can be found in appendix B. Data shown in the figure is measured with the Forward Hadron Calorimeter utilising the transverse energy algorithm (HFET) and a special afterglow correction applied by the HF experts to remove undesired noise. The beam overlap and peak were determined with the vdM framework, applying corrections to background rate 2.6.2, orbit drift 2.6.5, beam-beam deflection 2.6.3, beam β function 2.6.4, position 2.6.6 and peak 2.6.1. Timestamp for each scan is given as the time of the beginning of the scan step with 0 nominal beam separation. This choice of coordinates is arbitrary as long as the same convention is used for all scans, since effects taking place inside a single scan plane are not considered.

Slopes of the fits including corresponding errors are displayed in the upper part of the plots. The black markers show the average over bunches, while red and blue points show the quantities per BCID. Uncertainty in Σ per BCID is displayed, but visibility is limited as the error is typically smaller than the data point marker. Error of the slope of averages is estimated using standard error of the mean $SEM = \frac{\sigma}{\sqrt{N}}$, where σ is the standard deviation of the fit parameter estimated from the covariance matrix and N is the number of samples. Quantities on the right are the average slope and corresponding error, which is determined using propagation of uncertainty

$$err = \frac{\sqrt{\sum^{N} \sigma^2}}{N}, \tag{5.1}$$

where σ, N are similar to the fit on averages, but are now determined from fits to individual BCIDs.

It can be seen from figure 5.1, that values of Σ evolve over time. Furthermore, the trends are in the opposite directions: the convoluted beam width grows in x axis, but decreases in y axis. This reduces the net effect of the phenomenon, as σ_{vis} is calculated from the product of these. A linear fit seems like a reasonable choice, as the uncertainty of the slope is moderately low. Behaviour is studied individually for each bunch, as emittance is affected by the the bunches possibly colliding at some other interaction point [54]. The filling scheme in fill 6868 included bunches, that were colliding also at the LHCb and ALICE experiments.

Peak values presented in figure 5.2 also present a measurable time dependence. The peak value is generally expected to be same in both x and y axes, and dissimilarity between these is considered to be a source of systematic inaccuracy 2.6.1. However, the peak in y-axis displays a larger slope. Evolution of peak is only considered in error

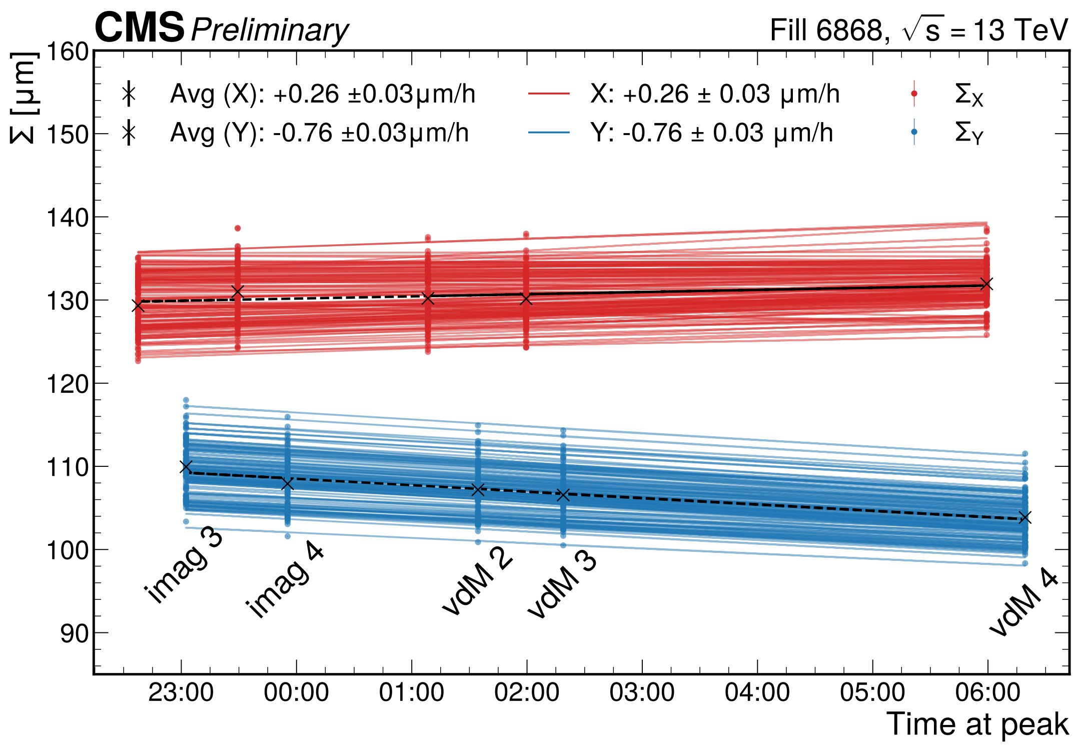

Figure 5.1. *Time evolution of convoluted beam width including linear fits, determined from rates measured using the Forward Hadron Calorimeter utilising the transverse energy algorithm (HFET).*

determination, as the normal procedure for determining σ_{vis} involves taking a mean of peaks, which is equivalent to interpolating the value to the point (t_{mid}) between time of scan in x axis (t_x) and time of scan in y axis (t_y). Instead, the values of Σ are propagated to t_{mid} using the slopes. The resulting σ_{vis} can then be compared to one obtained using the conventional method. Uncertainties of propagated values of Σ are estimated in two ways. First, a statistical uncertainty $\Delta\Sigma(t_{\mathrm{mid}})$ can be determined as the root mean square error (RMSE) between measured Σ and fit on both points t_x and t_y. Second, a systematic uncertainty is determined by comparing the trends of peak and Σ, using the assumption that σ_{vis} is independent of time:

$$\frac{\mathrm{d}\sigma_{\mathrm{vis}}}{\mathrm{d}t} = 0. \tag{5.2}$$

Substituting σ_{vis} with it's definition 2.20, we get condition

$$\frac{\mathrm{d}(peak \cdot \Sigma_x \cdot \Sigma_y)}{\mathrm{d}t} = 0 \tag{5.3}$$

and further

$$\frac{\mathrm{d}(peak)}{\mathrm{d}t} \cdot \Sigma_x \cdot \Sigma_y + peak \cdot \frac{\mathrm{d}(\Sigma_x)}{\mathrm{d}t} \cdot \Sigma_y + peak \cdot \Sigma_x \cdot \frac{\mathrm{d}(\Sigma_y)}{\mathrm{d}t} = 0, \tag{5.4}$$

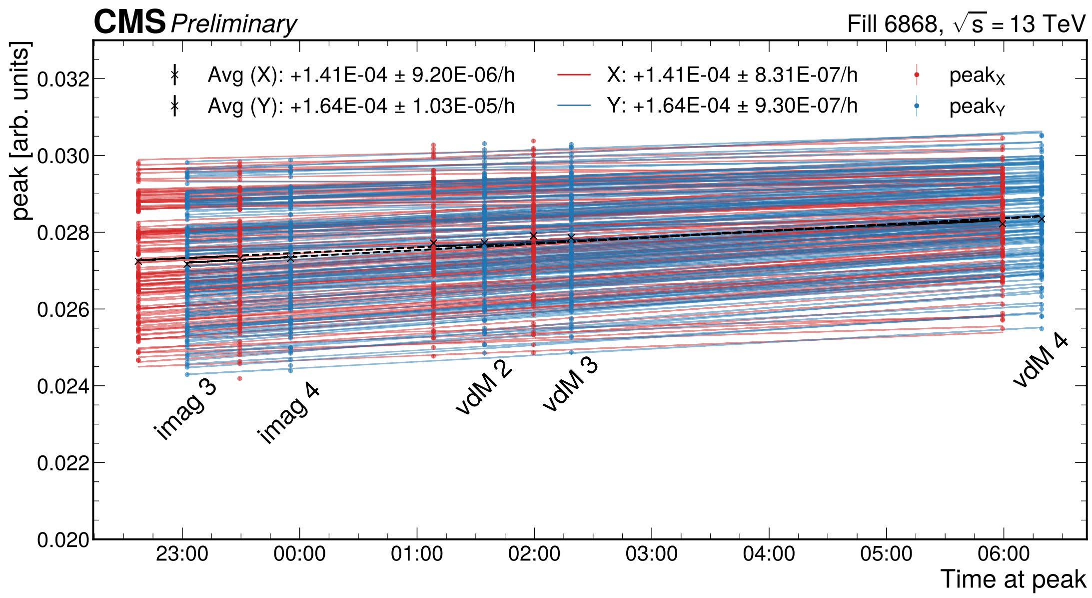

Figure 5.2. *Time evolution of fit peak including linear fits, determined from rates measured using the Forward Hadron Calorimeter utilising the transverse energy algorithm.*

which we can use to get an analytical estimate for peak time evolution (slope)

$$\frac{\mathrm{d}(peak)}{\mathrm{d}t} = -peak \cdot \left[\frac{1}{\Sigma_x} \frac{\mathrm{d}(\Sigma_x)}{\mathrm{d}t} + \frac{1}{\Sigma_y} \frac{\mathrm{d}(\Sigma_y)}{\mathrm{d}t} \right]. \tag{5.5}$$

Disagreement with the measured peak can be treated as a measure for systematical uncertainty by calculating σ_{vis} at both t_x and t_y, using the peak determined from corresponding plane. Discrepancy in the acquired values of σ_{vis} is the systematic error

$$\sigma_{\mathrm{x/y}} = \frac{1}{2} \left| \frac{\sigma_{\mathrm{vis}}(t_x) - \sigma_{\mathrm{vis}}(t_y)}{\sigma_{\mathrm{vis,orig}}} \right|. \tag{5.6}$$

5.3 Results

Table 5.1 contains the original σ_{vis} including statistical uncertainty ("original"), the σ_{vis} obtained by propagating the Σ values to $t = t_{\mathrm{mid}}$ with corresponding uncertainty ("corrected"), systematical uncertainty $\Delta_{\mathrm{x/y}}$ described above and finally the difference between the corrected and uncorrected σ_{vis}. σ_{vis} shown values are the weighted average over BCIDs taken using inverse-variance weighting

$$\hat{\sigma}_{\mathrm{vis}} = \frac{\sum_i y_i/\sigma_i^2}{\sum_i 1/\sigma_i^2}, \tag{5.7}$$

where the corresponding uncertainty is

$$\frac{1}{\sqrt{\sum_i 1/\sigma_i^2}}. \tag{5.8}$$

Weighted average is appropriate to take, as visible cross section of a detector should be independent of bunch shape and size variation.

Table 5.1. *Visible cross section σ_{vis} determined using the vdM framework with all available corrections ("original") and its relative error $\Delta\sigma_{\mathrm{vis}}$ [%], visible cross section obtained by propagating the convoluted beam widths Σ to the mid point between planes ("corrected") and its relative error $\Delta\sigma_{\mathrm{vis}}$ [%], systematical uncertainty in visible cross section caused by peak and Σ evolution discrepancy $\Delta_{\mathrm{x/y}}$, and the difference between the corrected and uncorrected visible cross sections.*

Luminometer	Scan	σ_{vis} [mb] original	$\Delta\sigma_{\mathrm{vis}}$ [%] original	σ_{vis} [mb] corrected	$\Delta\sigma_{\mathrm{vis}}$ [%] corrected	$\Delta_{\mathrm{x/y}}$ [%]	Difference in σ_{vis} [%]
HFET	imag1	2390.91	0.01	2388.05	0.01	0.18	0.04
HFET	vdM1	2380.12	0.01	2377.45	0.01	0.26	0.04
HFET	imag3	2427.30	0.01	2430.27	0.01	0.30	0.19
HFET	imag4	2422.62	0.01	2426.16	0.01	0.20	0.20
HFET	vdM2	2427.32	0.01	2431.00	0.01	0.22	0.20
HFET	vdM3	2426.09	0.01	2428.96	0.01	0.24	0.15
HFET	vdM4	2432.90	0.01	2435.78	0.01	0.29	0.15
HFOC	imag1	775.07	0.01	774.41	0.01	0.17	0.05
HFOC	vdM1	770.59	0.01	769.84	0.01	0.19	0.05
HFOC	imag3	774.53	0.01	775.17	0.01	0.32	0.19
HFOC	imag4	773.33	0.01	774.16	0.01	0.21	0.20
HFOC	vdM2	773.63	0.01	774.45	0.01	0.23	0.20
HFOC	vdM3	773.45	0.01	774.08	0.01	0.30	0.15
HFOC	vdM4	775.42	0.01	775.96	0.01	0.29	0.15
PLT	imag1	260.22	0.05	260.18	0.03	0.35	0.08
PLT	vdM1	258.88	0.05	258.89	0.03	0.50	0.08
PLT	imag3	260.22	0.03	260.68	0.02	0.47	0.19
PLT	imag4	259.59	0.03	260.16	0.02	0.45	0.20
PLT	vdM3	260.38	0.03	260.86	0.02	0.54	0.15
PLT	vdM4	261.17	0.03	261.62	0.02	0.49	0.16

It can be seen from the table, that correcting for time evolution does have effect on the visible cross section: the change in σ_{vis} is up to 0.2 %, which is considered to be significant for a high-precision measurement that aims to order of 1-2% total uncertainty. The systematic error $\Delta_{\mathrm{x/y}}$ is noticed to be relatively large, which may be caused by detector non-linearity. The effect is larger in the PLT than the HF, that is renowned for it's good linearity.

The effect of vdM framework corrections can be estimated by comparing table 5.1 to table C.1 which includes same quantities calculated without framework corrections. No qualitative difference in the effect of time evolution is observed.

Formulating the correction as a multiplicative factor to visible cross section allows the possibility to include time evolution correction to the vdM framework. The corrective factor can be calculated as a ratio between the value at the midpoint of scans and the original value is

$$C = \frac{\sigma_{\text{vis,corr}}}{\sigma_{\text{vis,orig}}} = \frac{\Sigma_{Xc}\Sigma_{Yc}}{\Sigma_{X1}\Sigma_{Y2}}, \tag{5.9}$$

where the corresponding uncertainty estimated with propagation of uncertainty is

$$\begin{aligned}(\Delta C)^2 = &\left[\frac{\partial C}{\partial \Sigma_{Xc}} \cdot \Delta(\Sigma_{Xc})\right]^2 + \left[\frac{\partial C}{\partial \Sigma_{Yc}} \cdot \Delta(\Sigma_{Yc})\right]^2 + \\ &\left[\frac{\partial C}{\partial \Sigma_{X1}} \cdot \Delta(\Sigma_{X1})\right]^2 + \left[\frac{\partial C}{\partial \Sigma_{Y2}} \cdot \Delta(\Sigma_{Y2})\right]^2,\end{aligned} \tag{5.10}$$

the partial derivatives being

$$\begin{aligned}\frac{\partial C}{\partial \Sigma_{Xc}} &= \frac{\Sigma_{Yc}}{\Sigma_{X1}\Sigma_{Y2}}, \quad \frac{\partial C}{\partial \Sigma_{Yc}} = \frac{\Sigma_{Xc}}{\Sigma_{X1}\Sigma_{Y2}}, \\ \frac{\partial C}{\partial \Sigma_{X1}} &= -\frac{\Sigma_{Xc}\Sigma_{Yc}}{\Sigma_{X1}^2\Sigma_{Y2}}, \quad \frac{\partial C}{\partial \Sigma_{Y2}} = -\frac{\Sigma_{Xc}\Sigma_{Yc}}{\Sigma_{X1}\Sigma_{Y2}^2}.\end{aligned} \tag{5.11}$$

Correction to the visible cross section could be extended to being a correction to convoluted beam widths and peak rate, that are used for calculating vdM framework corrections. Correction to the peak would be an improvement to the statistical precision and not systematic effects, whereas the correction to the beam widths addresses a systematic phenomenon. The effect of time evolution is nonetheless considered non-negligible and should be addressed at least by assigning an uncertainty to the results, with the possibility of adding a corrective factor to σ_{vis}.

6. CONCLUSIONS

Determining the luminosity, a quantity related to the amount of collected data, is of utmost importance to all collider physics measurements and searches. Precise luminosity measurement is one of the goals of the upcoming data taking period called *Run 3* (from 2022 on) at the Large Hadron Collider (LHC) and the Compact Muon Solenoid (CMS), which has been brought back to operation after a 3-year upgrade period, known as “long shutdown 2”. During this period, two dedicated detectors for luminosity measurement at CMS have been rebuilt: the Fast Beam Condition Monitor (BCM1F) and the Pixel Luminosity Telescope (PLT). They will operate along the Forward Hadron Calorimeter (HF) to measure the luminosity at the CMS experiment, which is the main aim this thesis contributes to.

The state-of-the-art luminosity measurements at the LHC are performed using the van der Meer (vdM) scan method where the two particle beams are moved over each other producing a way to determine the beam overlap width, which in turn can be used to estimate the visible cross section of a luminometer. The analysis of van der Meer scans is carried out using a software tool called *vdM framework*. Multiple improvements have been made to the analysis software, which increases the efficiency and accuracy of determining the visible cross section of luminometers. The vdM framework is now faster and simpler to use in producing the desired results and information for luminosity measurement. It is thus in a position allowing for distribution to a larger audience, with an improved workflow for a growing group of contributors, which is the ultimate goal of said tool.

The operability of the BCM1F and PLT luminometers has been demonstrated during a beam test period in October 2021 with both detectors being successfully commissioned by the end of the beam test, indicating them being ready for physics data taking. The new back-end system for BCM1F based on the µTCA standard has provided results consistent with the old back-end based on VME/RHU systems, after the old read-out was configured properly and faulty orbit-clock timing in the new system was corrected with post-processing. Having the old readout system operating in parallel was considered to be valuable, as it allowed for cross-comparison between the two systems. The timing of PLT channels has been successfully adjusted by the latter half of beam test, making it correctly working for physics operation.

Beside the upgraded software tool for the CMS collaboration, and the commissioning and initial luminosity measurement during the beam test, a physics case to correct an additional source of inaccuracy during precision luminosity measurements is investigated. The systematic effect caused by time evolution of the convoluted beam width of colliding particle beams during a vdM scan is demonstrated. This effect has not been previously well-studied at the CMS experiment. The impact on the precision of the σ_{vis} measurement has been found to be within 0.2% in a specific fill (fill 6868 in year 2018), which is non-negligible for a luminosity measurement that aims for total uncertainty of below 2%, and has to be taken into account to minimise the uncertainty. Addressing the effect by implementing a new correction to the vdM framework is proposed.

REFERENCES

[1] *LHC long term schedule*. lhc-commissioning.web.cern.ch, Jan. 2022. URL: http://lhc-commissioning.web.cern.ch/schedule/LHC-long-term.htm (visited on 02/13/2022).

[2] Chatrchyan, S., Khachatryan, V., Sirunyan, A., Tumasyan, A., Adam, W., Bergauer, T., Dragicevic, M., Erö, J., Fabjan, C., Friedl, M., Frühwirth, R., Ghete, V., Hammer, J., Hoch, M., Hörmann, N., Hrubec, J., Jeitler, M., Kiesenhofer, W. and Wenman, D. Observation of a new boson at a mass of 125 GeV with the CMS experiment at the LHC. *Physics Letters B* 716 (Aug. 2012), pp. 30–61. DOI: 10.1016/j.physletb.2012.08.021.

[3] Aad, G., Abajyan, T., Abbott, B., Abdallah, J., Khalek, S., Abdelalim, A., Abdinov, O., Aben, R., Abi, B., Abolins, M., AbouZeid, O., Abramowicz, H., Abreu, H., Acharya, B., Adamczyk, L., Adams, D., Addy, T., Adelman, J., Adomeit, S. and Zwalinski, L. Observation of a new particle in the search for the Standard Model Higgs boson with the ATLAS detector at the LHC. *Physics Letters B* 716 (Sept. 2012), pp. 1–29.

[4] Vretenar, M., Vollaire, J., Scrivens, R., Rossi, C., Roncarolo, F., Ramberger, S., Raich, U., Puccio, B., Nisbet, D., Mompo, R., Mathot, S., Martin, C., Lopez-Hernandez, L. A., Lombardi, A., Lettry, J., Lallement, J. B., Kozsar, I., Hansen, J., Gerigk, F., Funken, A., Fuchs, J. F., Dos Santos, N., Calviani, M., Buzio, M., Brunner, O., Body, Y., Baudrenghien, P., Bauche, J. and Zickler, T. *Linac4 design report*. Vol. 6. CERN Yellow Reports: Monographs. Geneva: CERN, 2020. DOI: 10.23731/CYRM-2020-006. URL: https://cds.cern.ch/record/2736208.

[5] Mattei, S. H^- ion source for CERN's Linac4 accelerator: simulation, experimental validation and optimization of the hydrogen plasma. Presented 24 Jul 2017. July 2017. URL: https://cds.cern.ch/record/2277635.

[6] *The accelerator complex | CERN*. home.cern. URL: https://home.cern/science/accelerators/accelerator-complex (visited on 02/13/2022).

[7] Karacheban, O. and Tsrunchev, P. Emittance scans for CMS luminosity calibration. *EPJ Web of Conferences* 201 (Jan. 2019), p. 04001. DOI: 10.1051/epjconf/201920104001.

[8] Chatrchyan, S., Hmayakyan, G., Khachatryan, V., Mousa, J., Adam, W., Bauer, T., Bergauer, T., Bergauer, H., Dragicevic, M., Erö, J. and Romaniuk, R. The CMS experiment at the CERN LHC. *Journal of Instrumentation* 3 (Aug. 2008), S08004.

[9] AC, C. Layout of CMS. Mar. 1998. URL: https://cds.cern.ch/record/39040.

[10] Barney, D. CMS Detector Slice. CMS Collection. Jan. 2016. URL: https://cds.cern.ch/record/2120661.

[11] *The CMS hadron calorimeter project: Technical Design Report*. Technical design report. CMS. Geneva: CERN, 1997. URL: http://cds.cern.ch/record/357153.

[12] The Pixel Luminosity Telescope: A detector for luminosity measurements at CMS using silicon pixel sensors. (July 2021). URL: https://cds.cern.ch/record/2781753.

[13] Lujan, P. J. *The Pixel Luminosity Telescope: a silicon sensor detector for luminosity measurement at CMS*. Tech. rep. Geneva: CERN, Oct. 2021. URL: https://cds.cern.ch/record/2797692.

[14] Kornmayer, A. The CMS pixel luminosity telescope. *Nuclear Instruments and Methods in Physics Research Section A: Accelerators, Spectrometers, Detectors and Associated Equipment* 824 (2016). Frontier Detectors for Frontier Physics: Proceedings of the 13th Pisa Meeting on Advanced Detectors, pp. 304–306. ISSN: 0168-9002. DOI: https://doi.org/10.1016/j.nima.2015.09.104. URL: https://www.sciencedirect.com/science/article/pii/S0168900215011936.

[15] Romeo, F. *Performance of the Pixel Luminosity Telescope for Luminosity Measurement at CMS during Run2*. Tech. rep. Geneva: CERN, Nov. 2019. URL: https://cds.cern.ch/record/2797807.

[16] Kästli, H., Barbero, M., Erdmann, W., Hörmann, C., Horisberger, R., Kotlinski, D. and Meier, B. Design and performance of the CMS pixel detector readout chip. *Nuclear Instruments and Methods in Physics Research Section A: Accelerators, Spectrometers, Detectors and Associated Equipment* 565.1 (Sept. 2006), pp. 188–194. ISSN: 0168-9002. DOI: 10.1016/j.nima.2006.05.038. URL: http://dx.doi.org/10.1016/j.nima.2006.05.038.

[17] Delannoy Sotomayor, A. G. and Wanczyk, J. BRIL LS2 Activity: PLT & BCM1f Integration. CMS Collection. Mar. 2021. URL: http://cds.cern.ch/record/2765247.

[18] Lujan, P. J. *The Pixel Luminosity Telescope: a silicon sensor detector for luminosity measurement at CMS*. Tech. rep. Geneva: CERN, Oct. 2021. URL: http://cds.cern.ch/record/2797692.

[19] Bernardino Rodrigues, N., Hall-Wilton, R., Lange, W., Lohmann, W., MacPherson, A., Ohlerich, M., Ryzhov, V., Schmidt, R. and Stone, R. L. Fast Beam Conditions Monitoring (BCM1F) for CMS. (2008). DOI: 10.5170/CERN-2008-008.259. URL: https://cds.cern.ch/record/1158637.

[20] Zagozdzinska, A. A., Bell, A., Dabrowski, A., Hempel, M., Henschel, H., Karacheban, O., Przyborowski, D., Leonard, J., Penno, M., Pozniak, K., Miraglia, M., Lange, W., Lohmann, W., Ryjov, V., Lokhovitskiy, A., Stickland, D. and Walsh, R. *New Fast Beam Conditions Monitoring (BCM1F) system for CMS*. Tech. rep. Geneva: CERN, Nov. 2015. DOI: 10.1088/1748-0221/11/01/C01088. URL: https://cds.cern.ch/record/2120145.

[21] Delannoy Sotomayor, A. G. and Wanczyk, J. CMS BRIL BCM1F c-shape. CMS Collection. May 2022. URL: http://cds.cern.ch/record/2809025.

[22] Guthoff, M. The new Fast Beam Condition Monitor using poly-crystalline diamond sensors for luminosity measurement at CMS. *Nuclear Instruments and Methods in Physics Research Section A: Accelerators, Spectrometers, Detectors and Associated Equipment* 936 (2019). Frontier Detectors for Frontier Physics: 14th Pisa Meeting on Advanced Detectors, pp. 717–718. ISSN: 0168-9002. DOI: https://doi.org/10.1016/j.nima.2018.11.071. URL: https://www.sciencedirect.com/science/article/pii/S0168900218316802.

[23] Karacheban, O. Luminosity measurement at CMS. 2017. URL: http://cds.cern.ch/record/2294183.

[24] *CMS luminosity measurement using nucleus-nucleus collisions at $\sqrt{s_{\mathrm{NN}}} = 5.02$ TeV in 2018*. Tech. rep. Geneva: CERN, 2022. URL: http://cds.cern.ch/record/2809613.

[25] *HFLumi Readiness review*. URL: https://indico.cern.ch/event/1157582/contributions/4865712/attachments/2441863/4183320/HFLumi%5C_MayReview.pdf (visited on 05/27/2022).

[26] CMS Collaboration. Precision luminosity measurement in proton-proton collisions at $\sqrt{s} =$ 13 TeV in 2015 and 2016 at CMS. *Eur. Phys. J. C* 81 (Apr. 2021). Replaced with the published version. Added the journal reference and the DOI. All the figures and tables can be found at http://cms-results.web.cern.ch/cms-results/public-results/publications/LUM-17-003 (CMS Public Pages), 800. 42 p. DOI: 10.1140/epjc/s10052-021-09538-2. arXiv: 2104.01927. URL: https://cds.cern.ch/record/2759951.

[27] Triossi, A. *The CMS Barrel Muon Trigger Upgrade*. Tech. rep. Geneva: CERN, Nov. 2016. DOI: 10.1088/1748-0221/12/01/C01095. URL: https://cds.cern.ch/record/2252301.

[28] Forkel-Wirth, D., Perrin, D., Scibile, L., Segura, G. and Vojtyla, P. Radiation monitoring system for the environment and safety project. (Nov. 2002). URL: http://cds.cern.ch/record/687619.

[29] Furman, M. A. The moller luminosity factor. *escholarship.org* (Aug. 2003). URL: https://escholarship.org/uc/item/3897k3zp (visited on 02/03/2022).

[30] Meer, S. van der. *Calibration of the effective beam height in the ISR*. Tech. rep. Geneva: CERN, 1968. URL: https://cds.cern.ch/record/296752.

[31] collaboration, T. L. Precision luminosity measurements at LHCb. *Journal of Instrumentation* 9.12 (Dec. 2014), P12005–P12005. ISSN: 1748-0221. DOI: 10.1088/1748-0221/9/12/p12005. URL: http://dx.doi.org/10.1088/1748-0221/9/12/P12005.

[32] Nonfactorization in Van der Meer scans in Run 2. (June 2019). URL: https://cds.cern.ch/record/2681801.

[33] Bassetti, M. and Erskine, G. A. *Closed expression for the electrical field of a two-dimensional Gaussian charge*. Tech. rep. Geneva: CERN, 1980. URL: https://cds.cern.ch/record/122227.

[34] Bambade, P., Erickson, R., Koska, W. A., Kozanecki, W., Phinney, N. and Wagner, S. R. Observation of beam-beam deflections at the interaction point of the SLAC Linear Collider. *Phys. Rev. Lett.* 62 (25 June 1989), pp. 2949–2952. DOI: 10.1103/PhysRevLett.62.2949. URL: https://link.aps.org/doi/10.1103/PhysRevLett.62.2949.

[35] Gąsior, M., Baud, G., Olexa, J. and Valentino, G. First Operational Experience with the LHC Diode ORbit and OScillation (DOROS) System. (2017), MOPG07. 4 p. DOI: 10.18429/JACoW-IBIC2016-MOPG07. URL: https://cds.cern.ch/record/2313935.

[36] Odier, P., Ludwig, M. and Thoulet, S. *The DCCT for the LHC Beam Intensity Measurement*. Tech. rep. Geneva: CERN, May 2009. URL: https://cds.cern.ch/record/1183400.

[37] Gras, J. J., Belohrad, D., Ludwig, M., Odier, P. and Barschel, C. Optimization of the LHC beam current transformers for accurate luminosity determination. (Sept. 2011), 4 p. URL: https://cds.cern.ch/record/1379466.

[38] Alici, A., Anders, G., Bacchetta, N., Balagura, V., Barschel, C., Bravin, E., Burkhardt, H., Ferro-Luzzi, M., Gagliardi, M., Gras, J. J., Heinemann, B., Hopchev, P., Huhtinen, M., Jeff, A., Kozanecki, W., Pagan Griso, S., Panman, J., White, S. and Zuranski, A. Study of the LHC ghost charge and satellite bunches for luminosity calibration. (Feb. 2012). URL: https://cds.cern.ch/record/1427728.

[39] *BRIL/VdMFramework GitLab page*. gitlab.cern.ch, 2022. URL: https://gitlab.cern.ch/bril/VdMFramework (visited on 02/13/2022).

[40] *BRIL/VdMFramework GitLab page*. docs.cern.ch, 2022. URL: https://vdmdoc.docs.cern.ch (visited on 02/14/2022).

[41] Brun, R., Rademakers, F., Canal, P., Naumann, A., Couet, O., Moneta, L., Vassilev, V., Linev, S., Piparo, D., GANIS, G., Bellenot, B., Guiraud, E., Amadio, G., wverkerke, Mato, P., TimurP, Tadel, M., wlav, Tejedor, E., Blomer, J., Gheata, A., Hageboeck, S., Roiser, S., marsupial, Wunsch, S., Shadura, O., Bose, A., CristinaCristescu, Valls, X. and Isemann, R. *root-project/root: v6.18/02*. Version v6-18-02. Aug. 2019. DOI: 10.5281/zenodo.3895860. URL: https://doi.org/10.5281/zenodo.3895860.

[42] Koranne, S. Hierarchical data format 5: HDF5. *Handbook of Open Source Tools*. Springer, 2011, pp. 191–200.

[43] *The new Git default branch name*. URL: https://about.gitlab.com/blog/2021/03/10/new-git-default-branch-name (visited on 05/05/2022).

[44] *Renaming the default branch from master*. URL: https://github.com/github/renaming (visited on 05/05/2022).

[45] *The YAML format*. URL: https://yaml.org (visited on 05/05/2022).

[46] *Sphinx documentation*. URL: https://www.sphinx-doc.org/en/master (visited on 05/05/2022).

[47] *XRootD*. URL: https://xrootd.slac.stanford.edu/ (visited on 04/20/2022).

[48] *the vdM framework documentation*. URL: https://vdmdoc.docs.cern.ch/ (visited on 05/15/2022).

[49] *Presentation layer of CMS Online Monitoring System*. Tech. rep. Geneva: CERN, Nov. 2018. DOI: 10.1051/epjconf/201921401044. URL: https://cds.cern.ch/record/2649402.

[50] *WebEOS Manual*. docs.cern.ch, 2022. URL: https://webeos.docs.cern.ch/ (visited on 04/14/2022).

[51] Agrigoroae, C. *The four LHC experiments are getting ready for pilot beams*. CERN, 2021. URL: https://home.cern/news/news/experiments/four-lhc-experiments-are-getting-ready-pilot-beams (visited on 02/09/2022).

[52] Leonard, J. L. *Luminosity measurement at CMS*. Tech. rep. Geneva: CERN, June 2014. URL: https://cds.cern.ch/record/1969404.

[53] *CMS luminosity measurement for the 2018 data-taking period at* $\sqrt{s} = 13$ TeV. Tech. rep. Geneva: CERN, 2019. URL: https://cds.cern.ch/record/2676164.

[54] Wanczyk, J. *MultiIP simulations of beam-beam corrections*. URL: https://indico.cern.ch/event/950869/#13-multiip-simulations-of-beam (visited on 05/23/2022).

APPENDIX A: OCTOBER 2021 BEAM TEST RESULTS

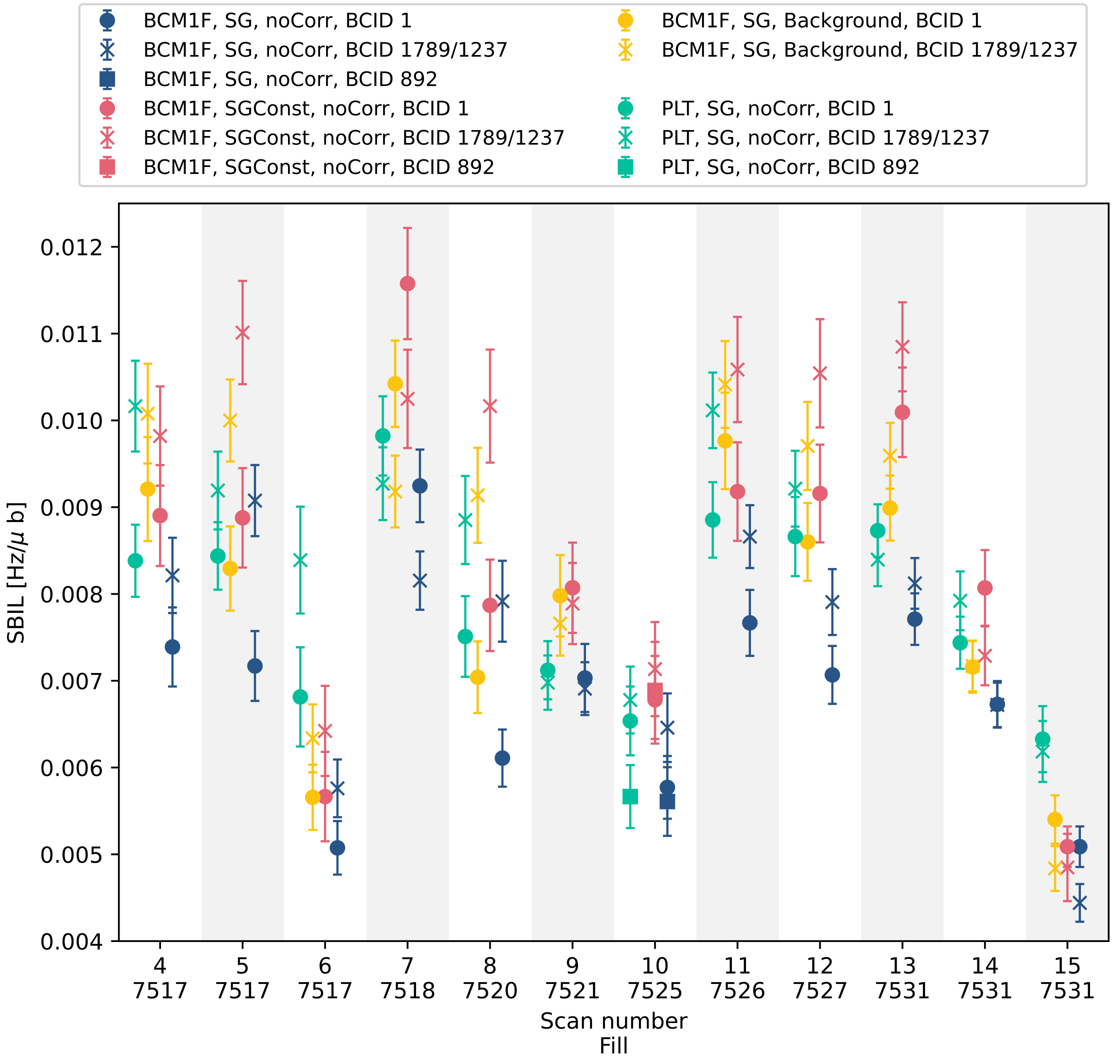

Figure A.1. *Single bunch instantaneous luminosity (SBIL) for the Fast Beam Condition Monitor (BCM1F) and Pixel Luminosity Telescope (PLT).*

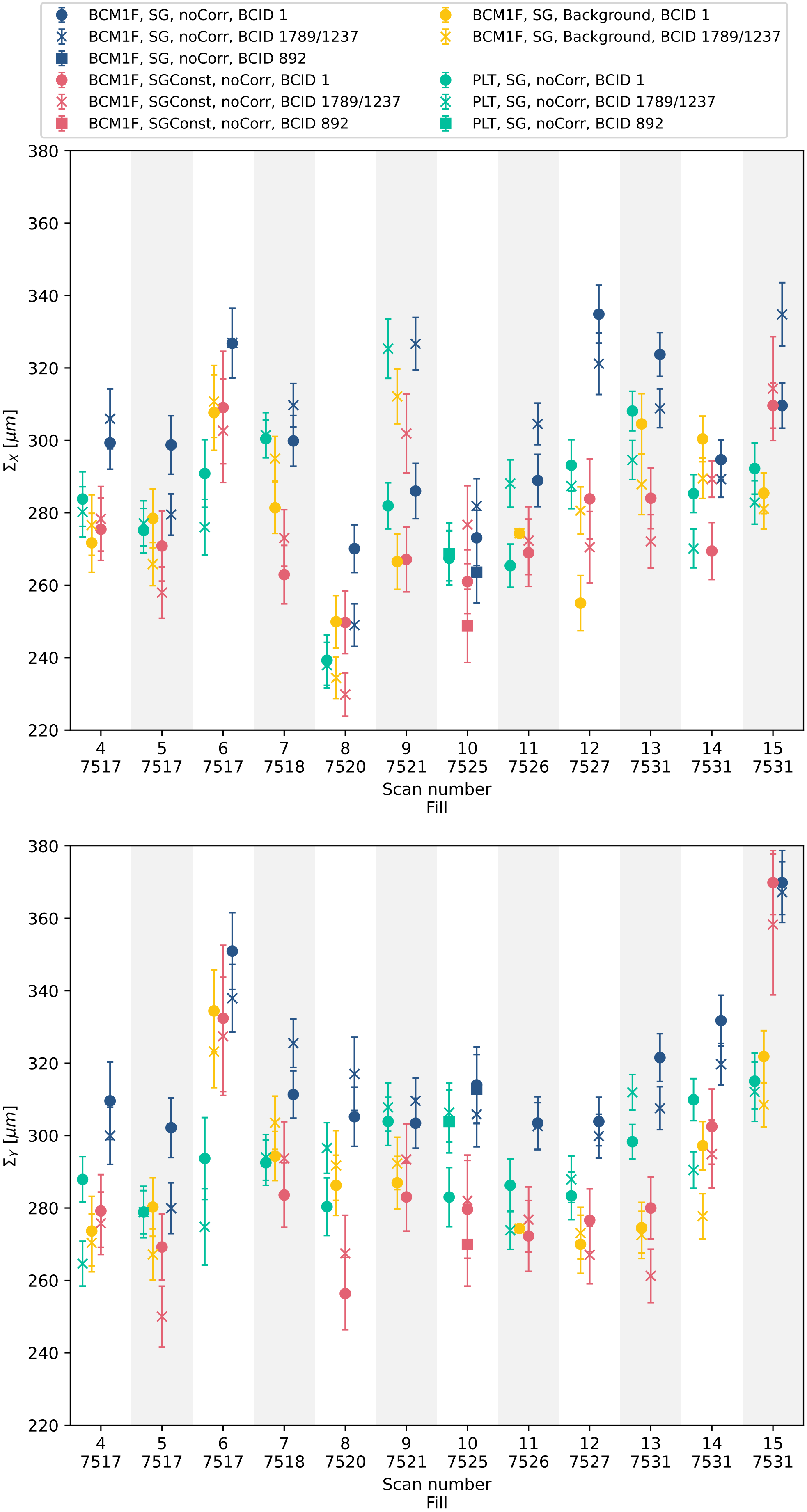

Figure A.2. *Convoluted beam width in x-axis.*

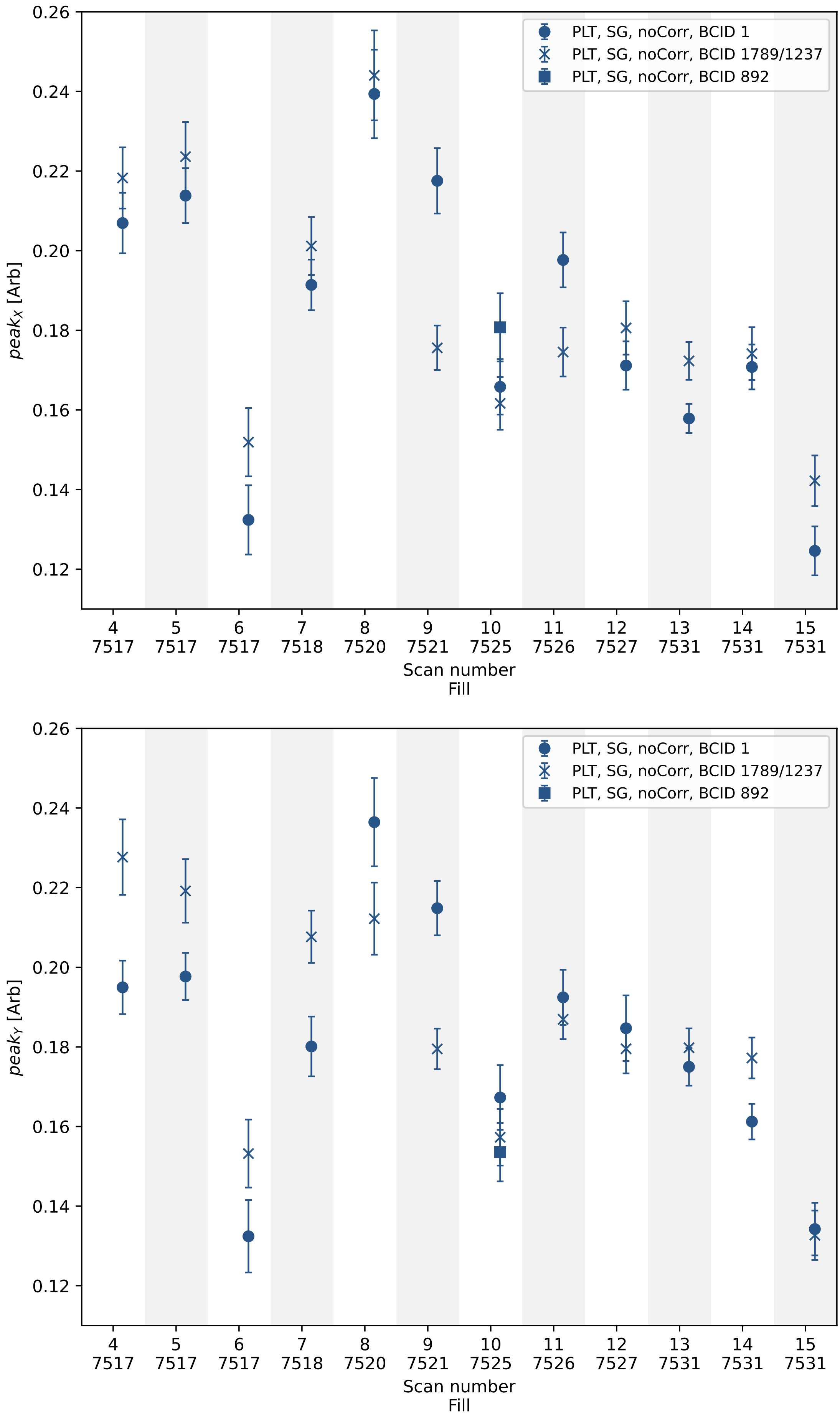

Figure A.3. *Peak of fit for Pixel Luminosity Telescope (PLT).*

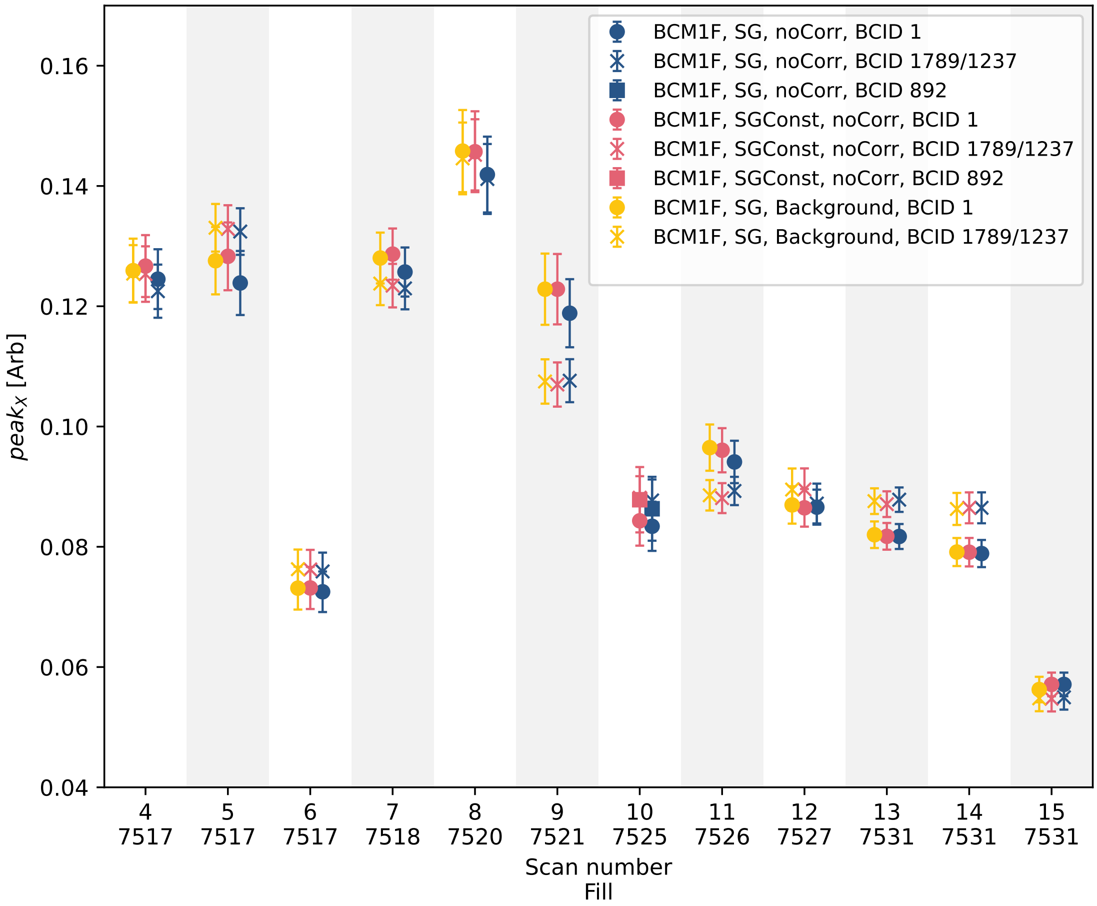

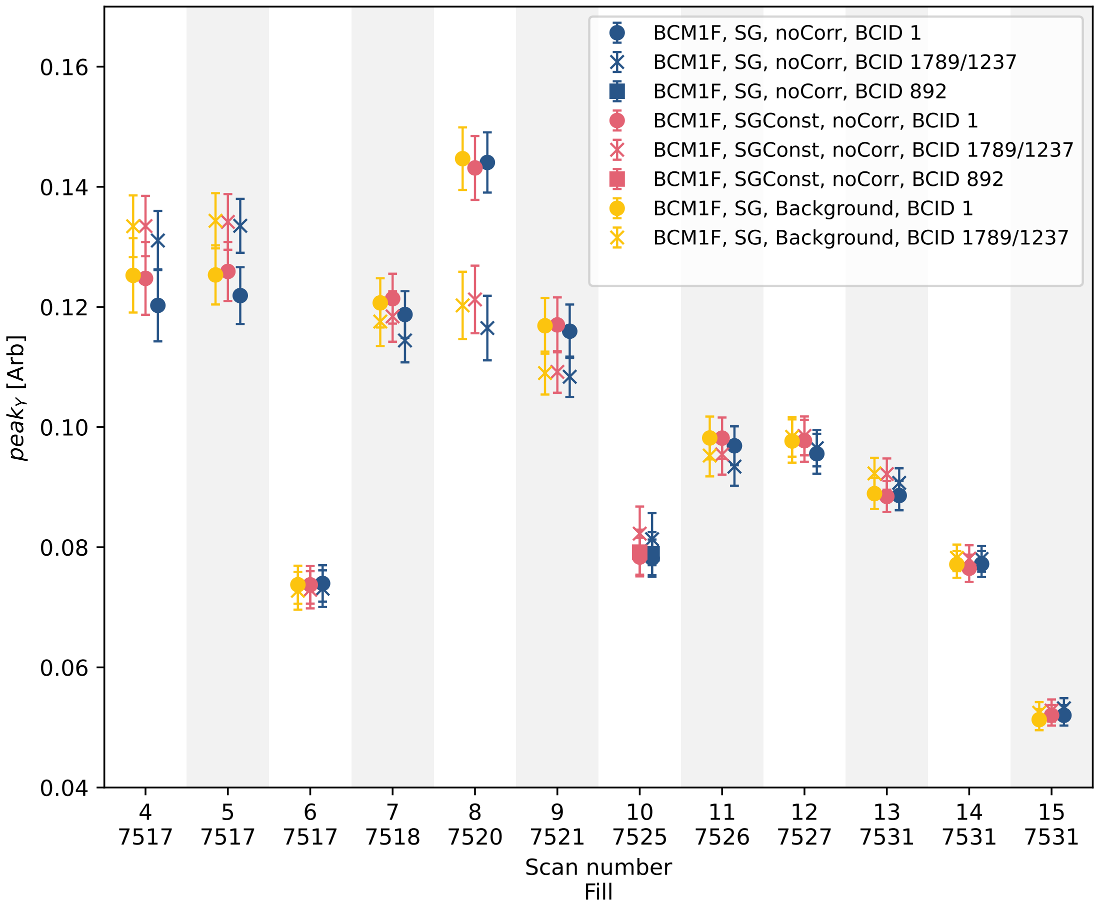

Figure A.4. *Peak of fit for the Fast Beam Condition Monitor (BCM1F).*

APPENDIX B: FITS TO CONVOLUTED BEAM WIDTH AND PEAK OVER TIME

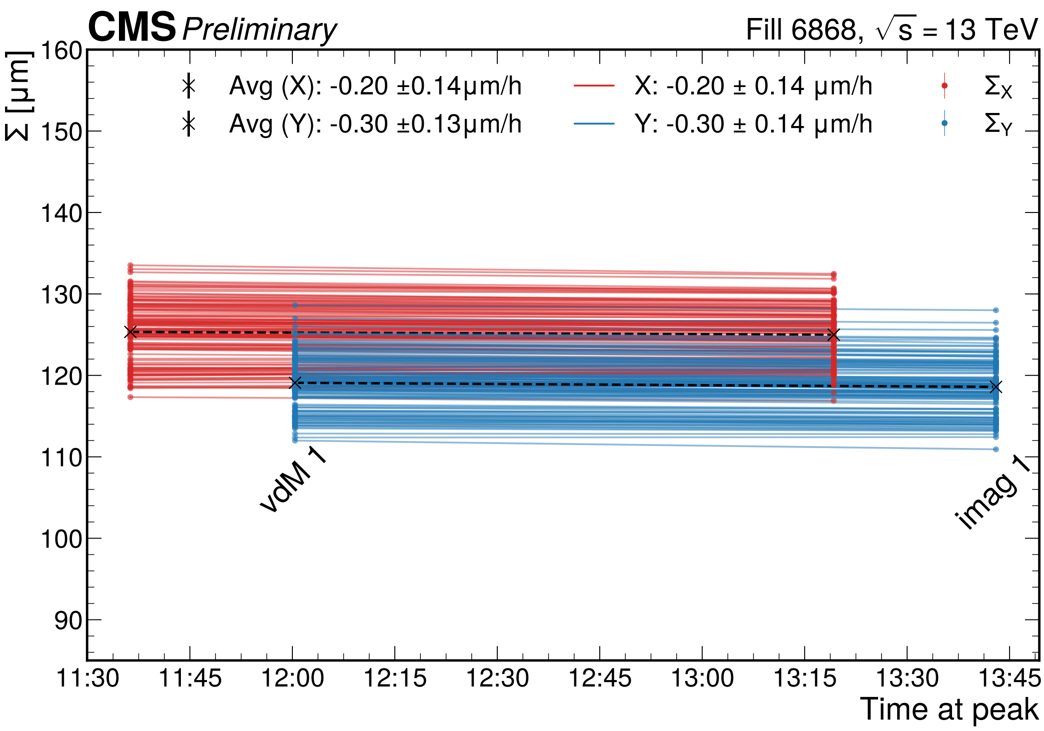

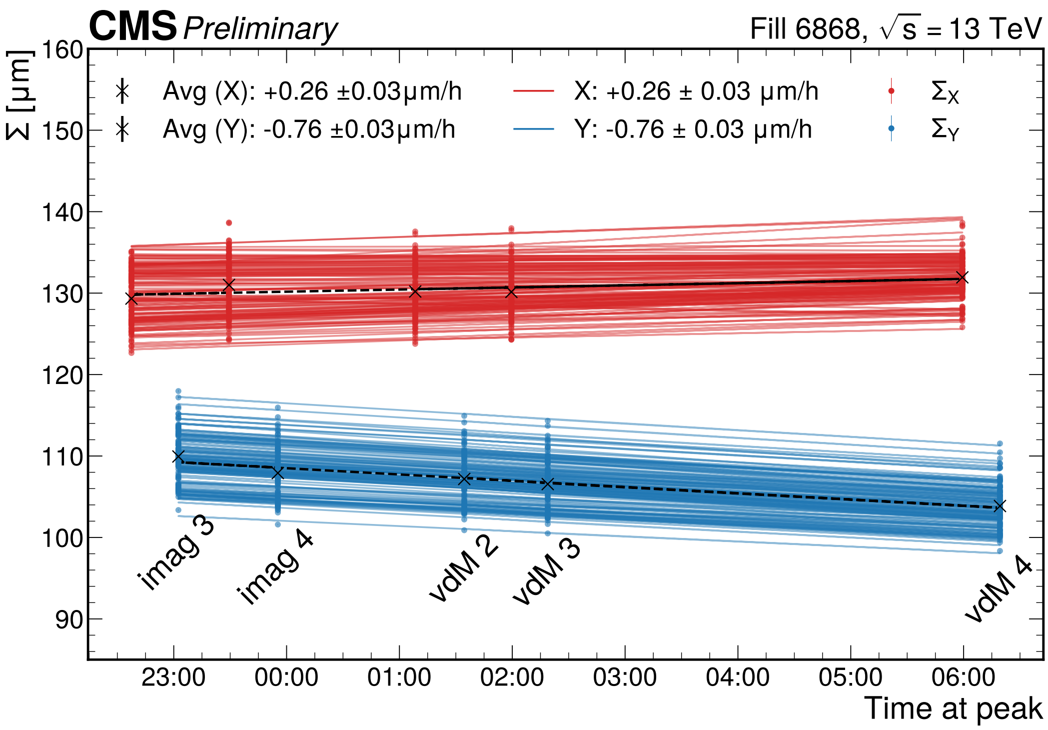

Figure B.1. *Time evolution of convoluted beam width including linear fits, HFET luminometer, all corrections applied.*

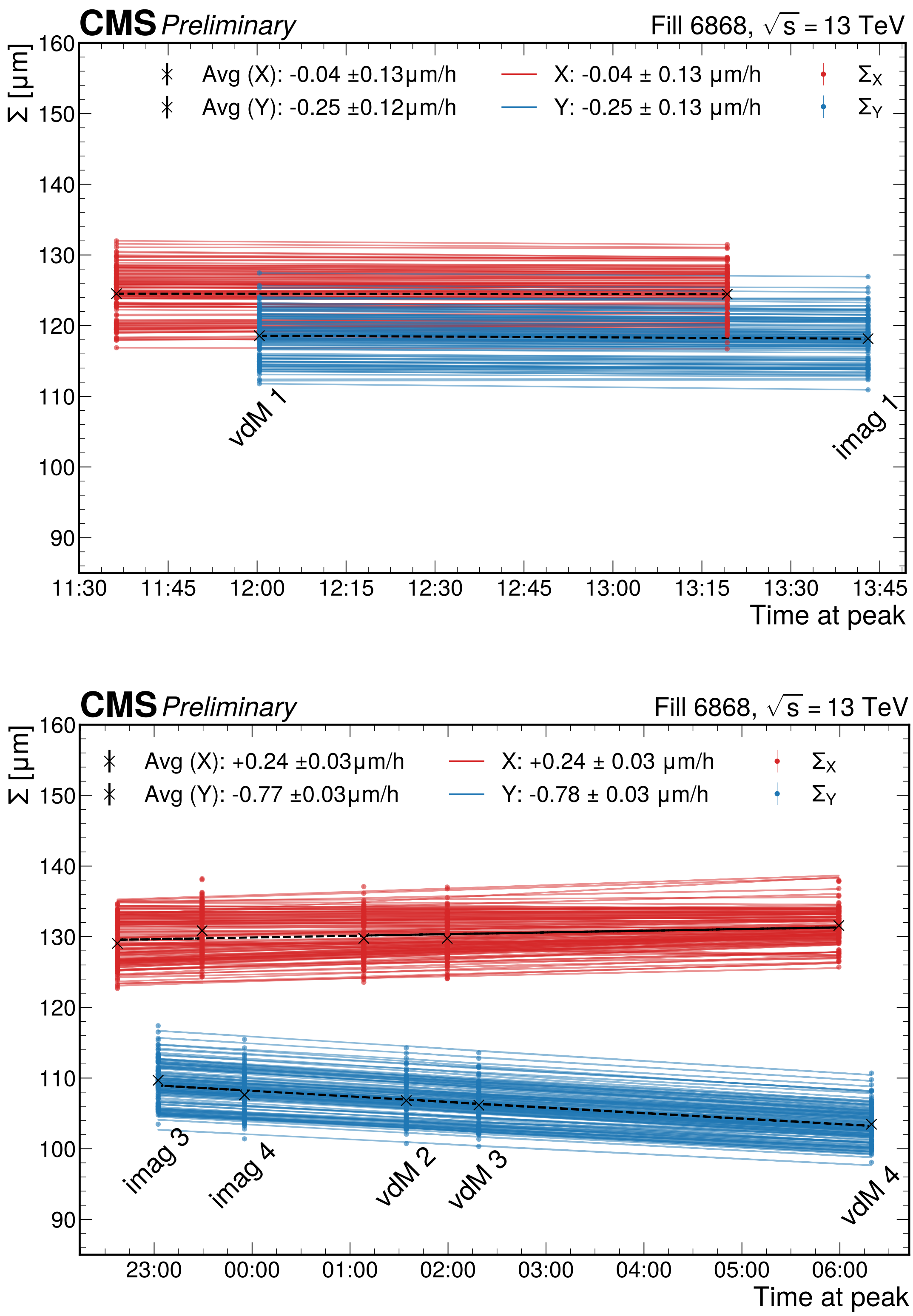

Figure B.2. *Time evolution of convoluted beam width including linear fits, HFOC luminometer, all corrections applied.*

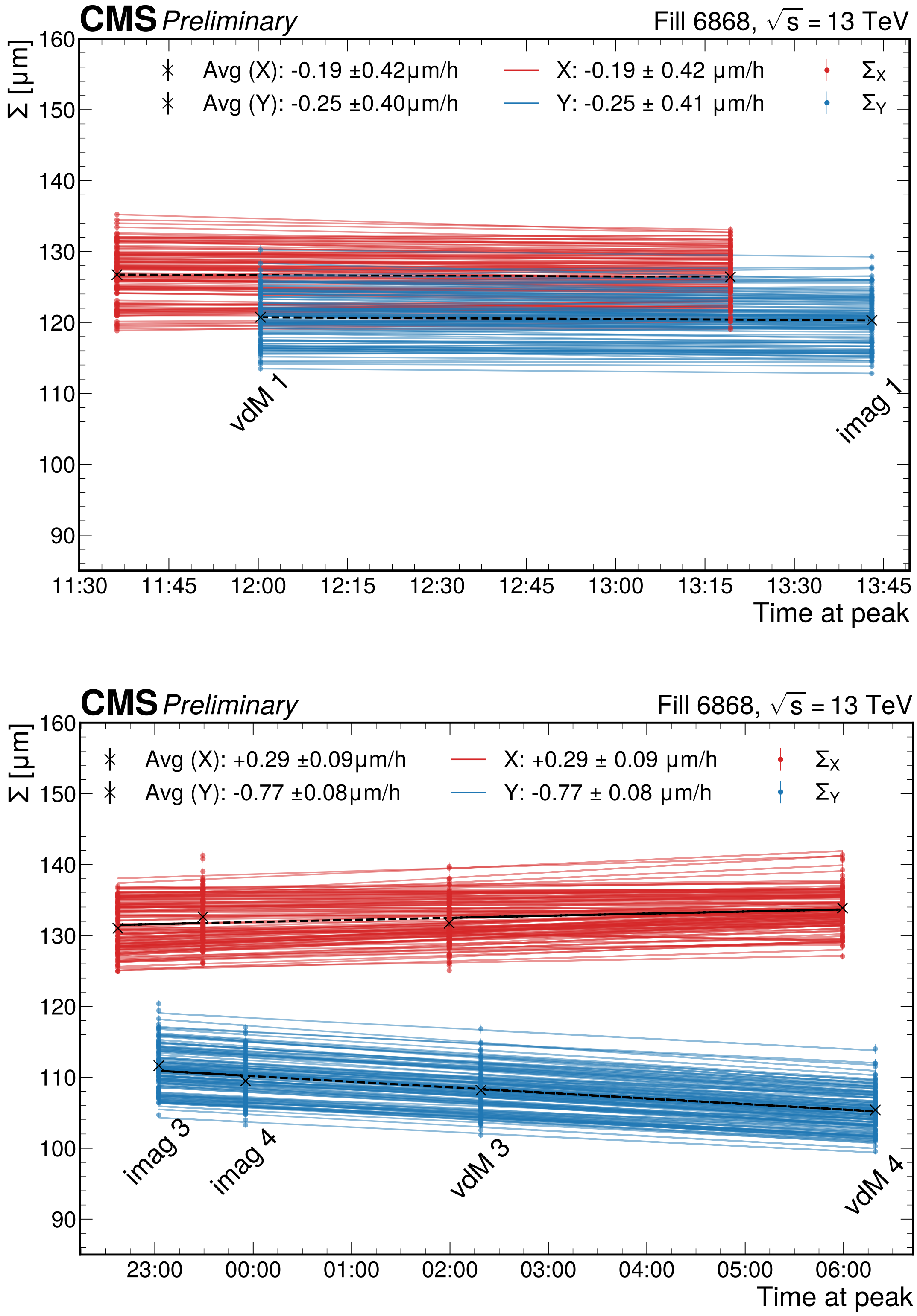

Figure B.3. *Time evolution of convoluted beam width including linear fits, PLT luminometer, all corrections applied.*

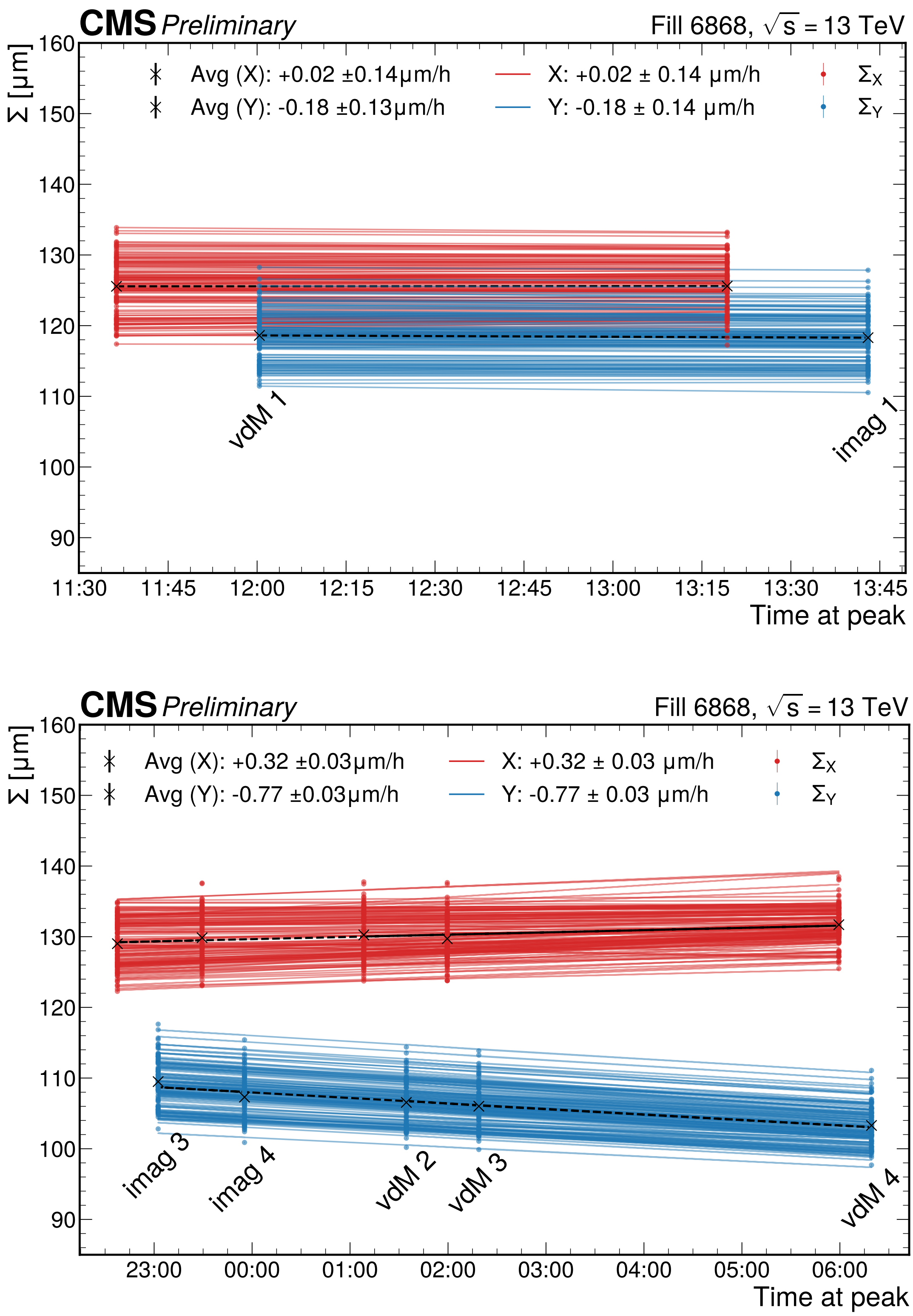

Figure B.4. *Time evolution of convoluted beam width including linear fits, HFET luminometer, no corrections applied.*

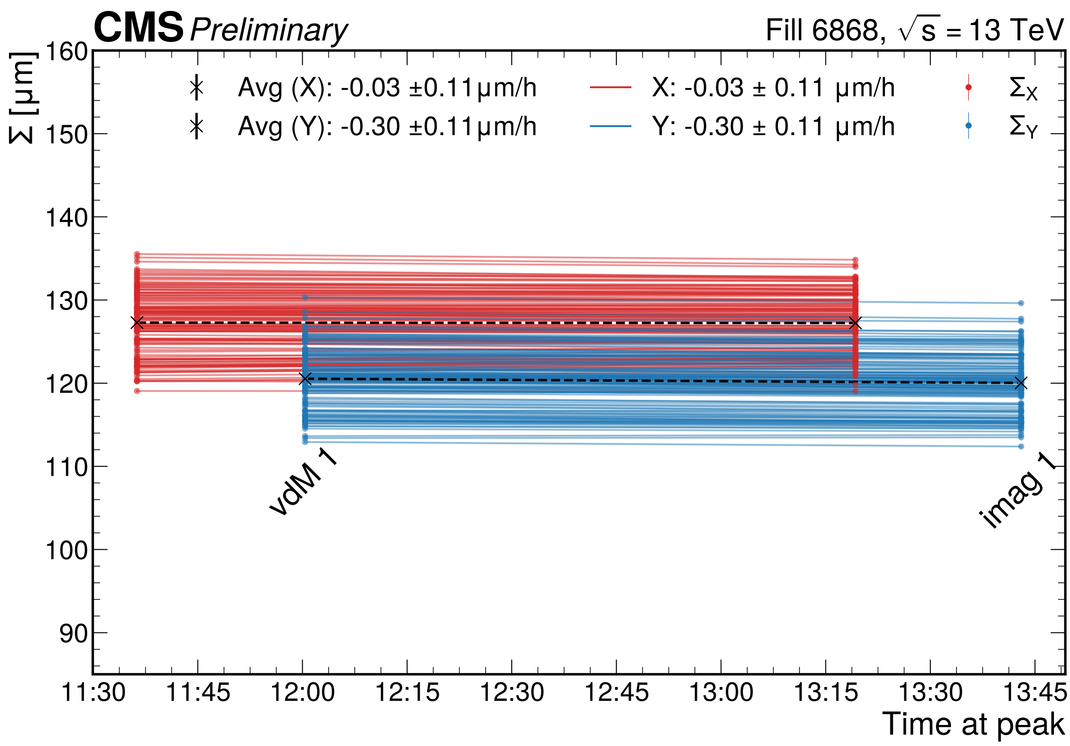

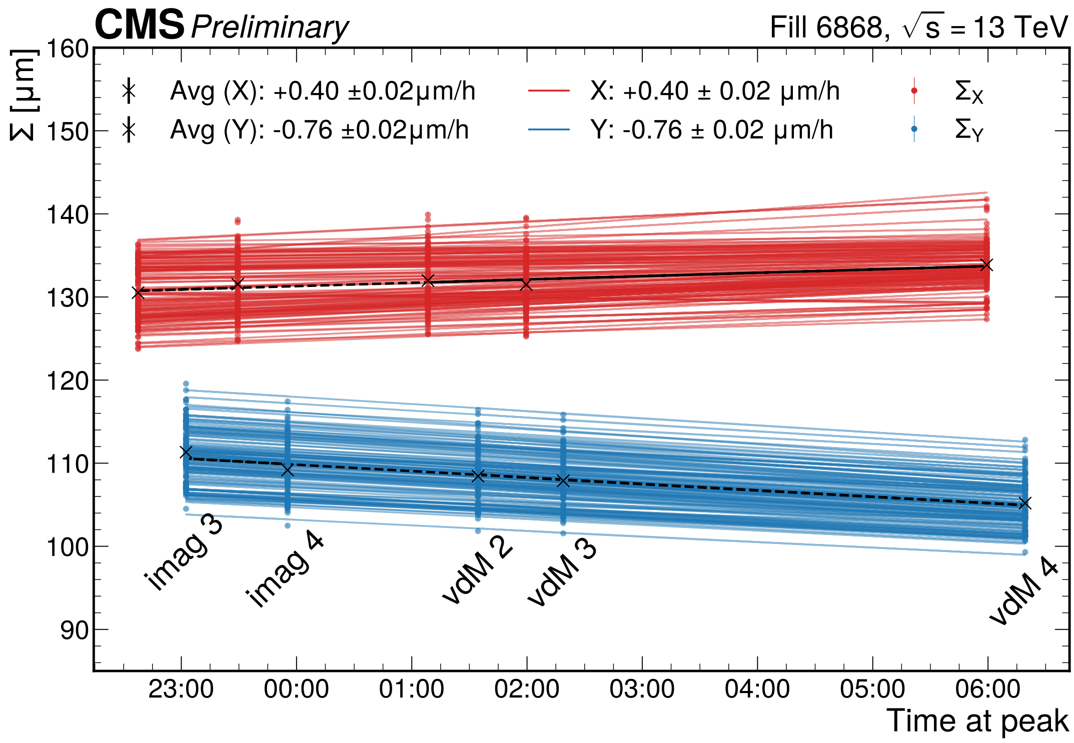

Figure B.5. *Time evolution of convoluted beam width including linear fits, HFOC luminometer, no corrections applied*

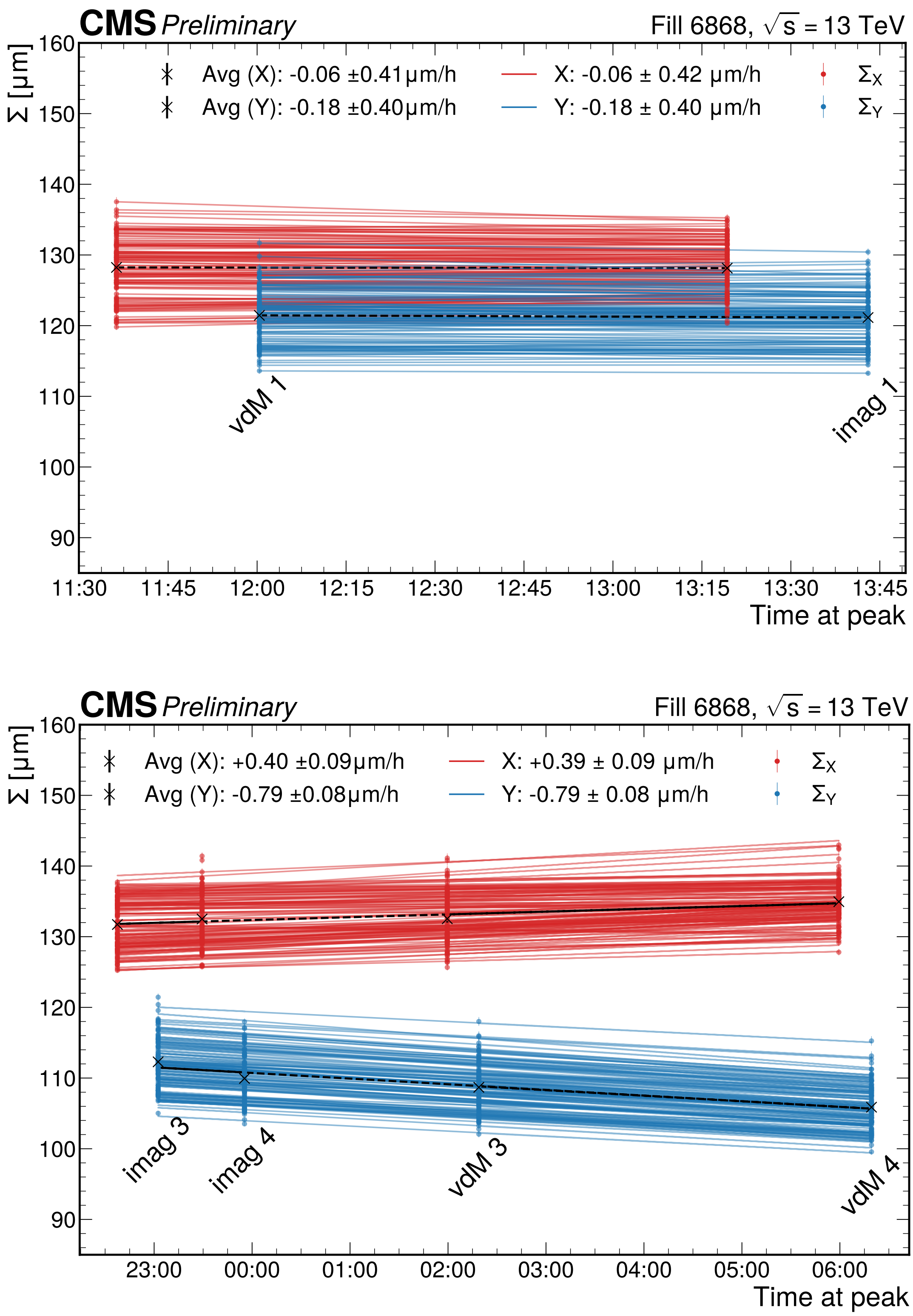

Figure B.6. *Time evolution of convoluted beam width including linear fits, PLT luminometer, no corrections applied.*

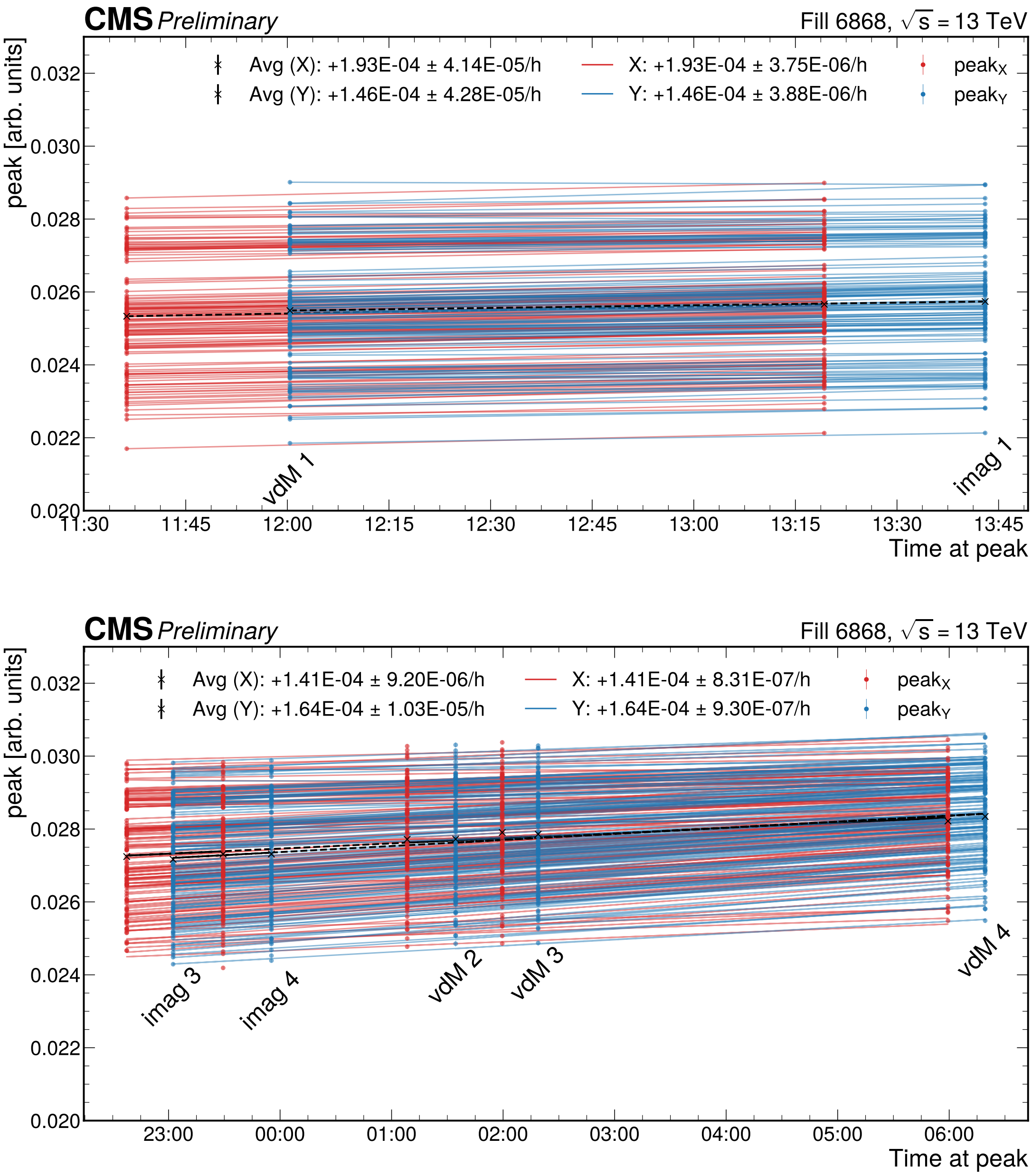

Figure B.7. *Time evolution of peak including linear fits, HFET luminometer, all corrections applied.*

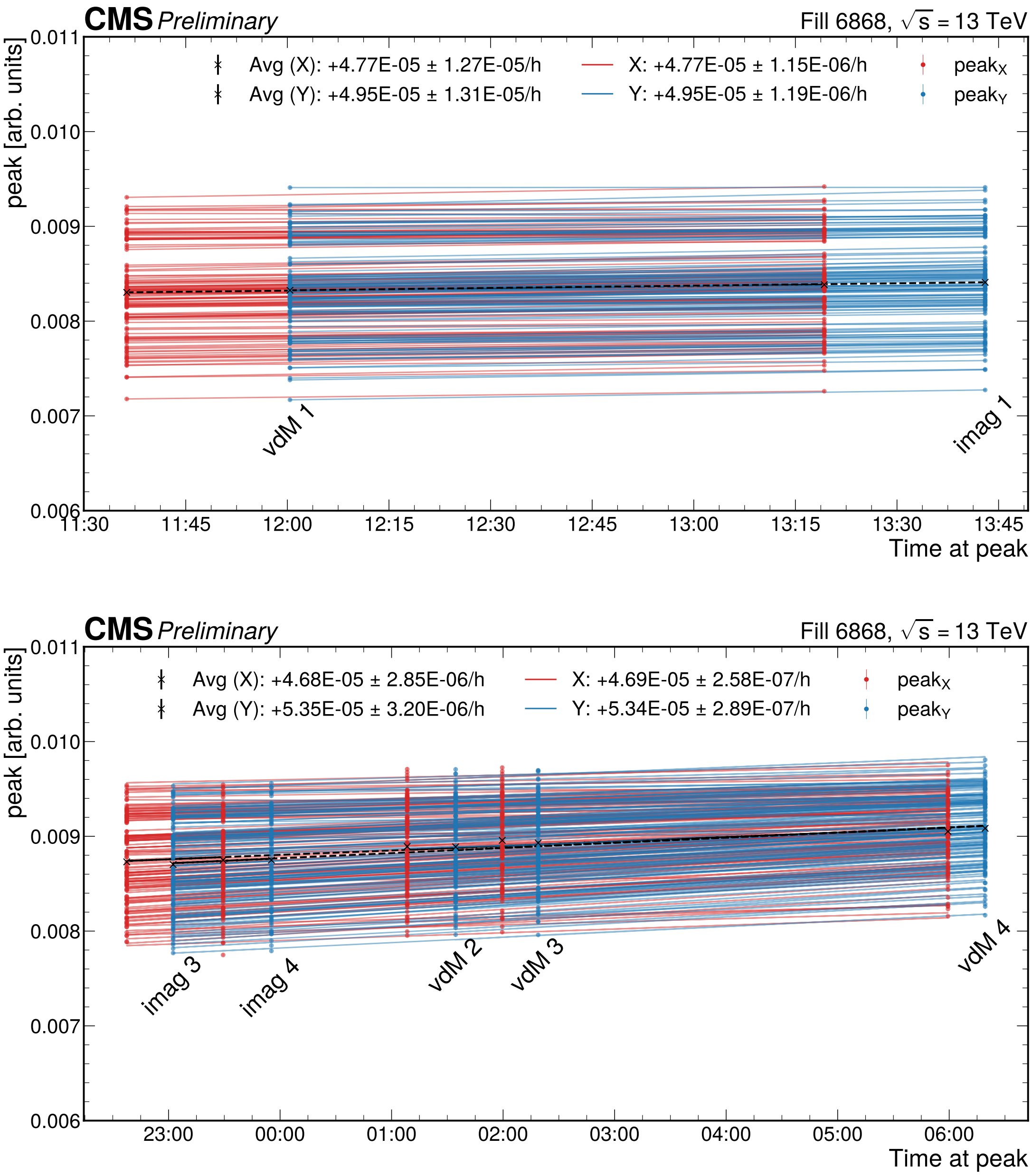

Figure B.8. *Time evolution of peak including linear fits, HFOC luminometer, all corrections applied.*

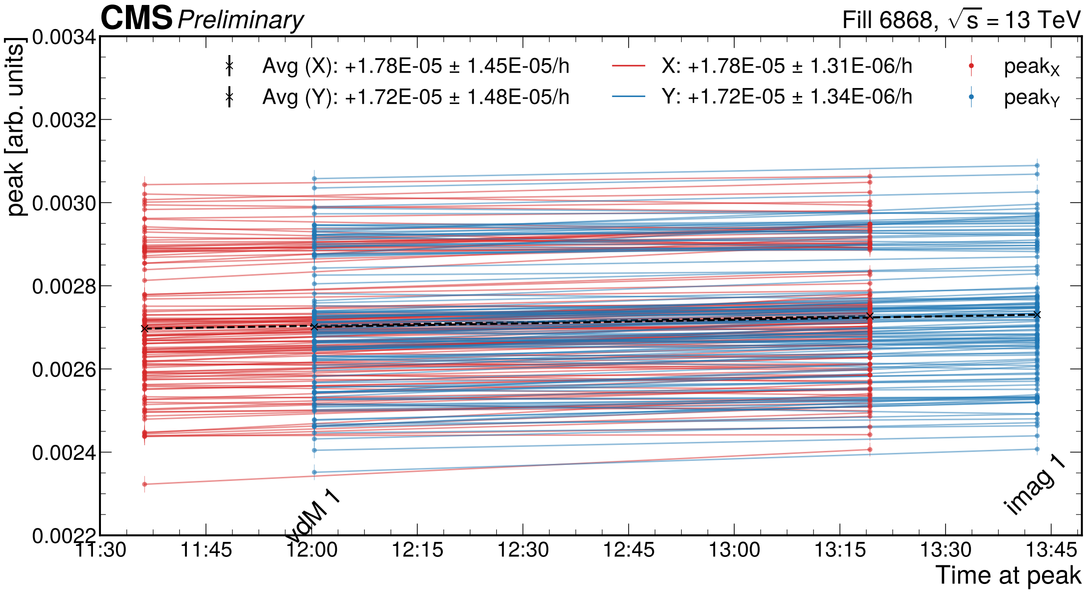

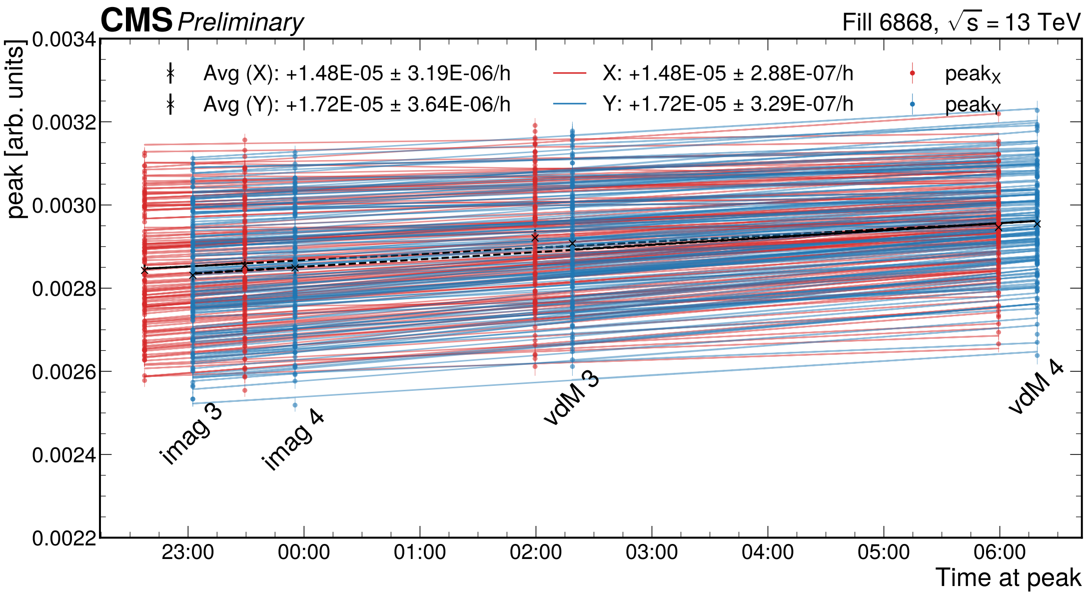

Figure B.9. *Time evolution of peak including linear fits, PLT luminometer, all corrections applied.*

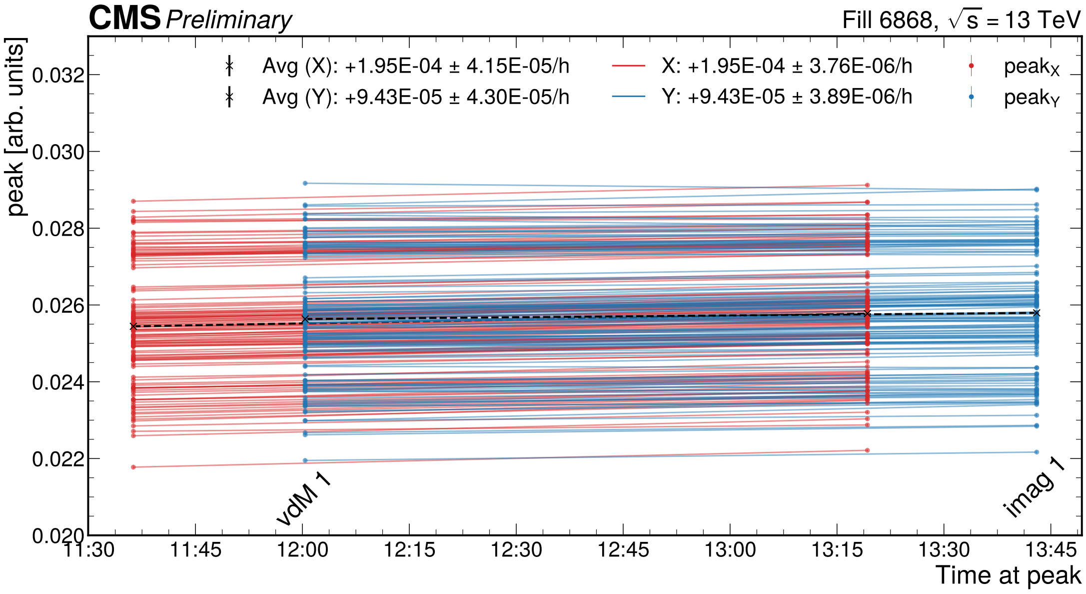

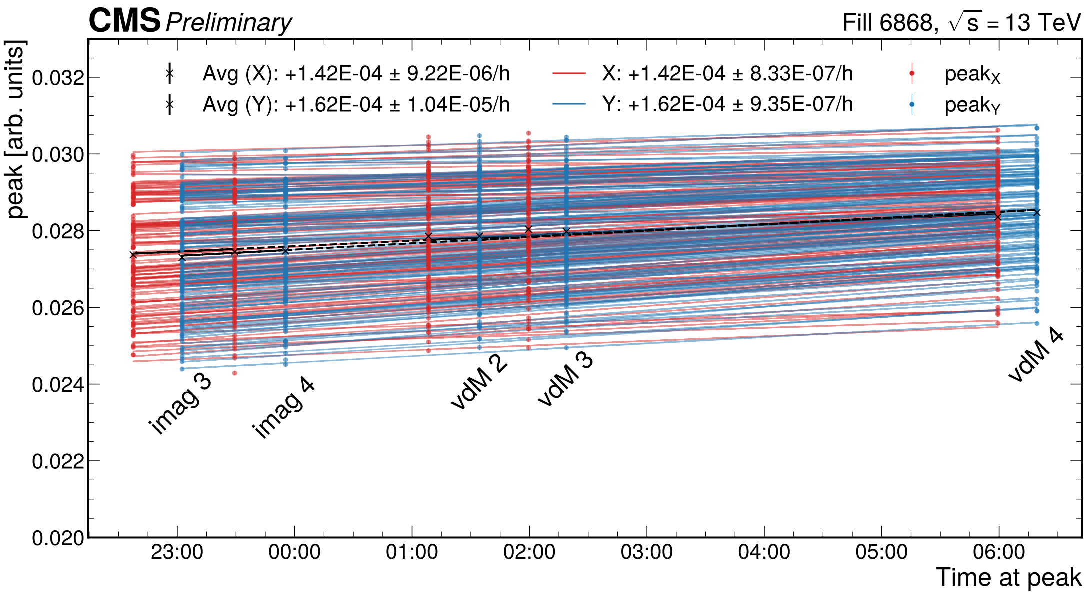

Figure B.10. *Time evolution of peak including linear fits, HFET luminometer, no corrections applied.*

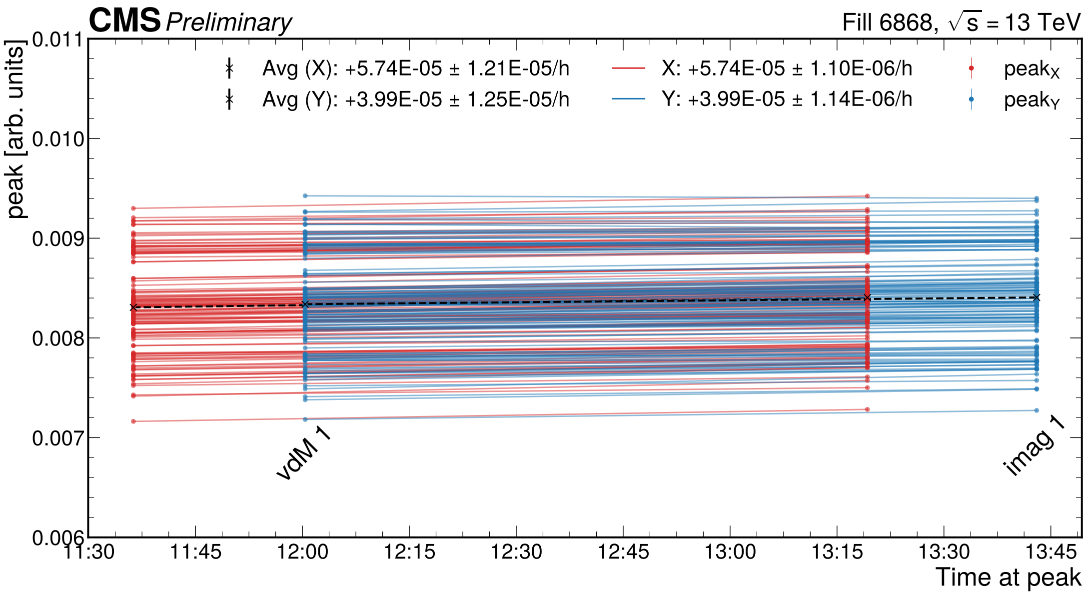

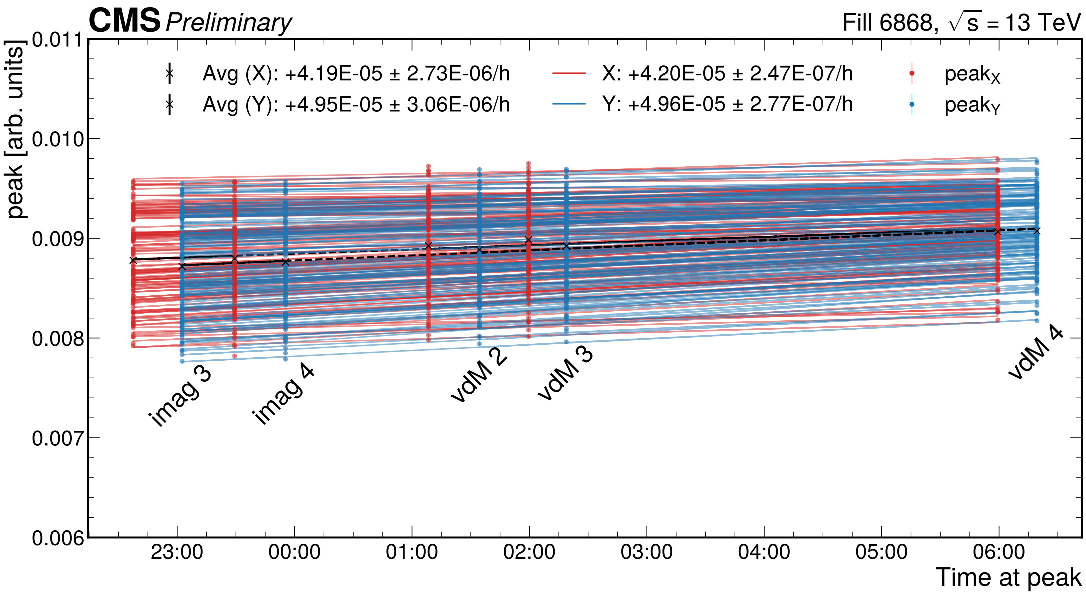

Figure B.11. *Time evolution of peak including linear fits, HFOC luminometer, no corrections applied.*

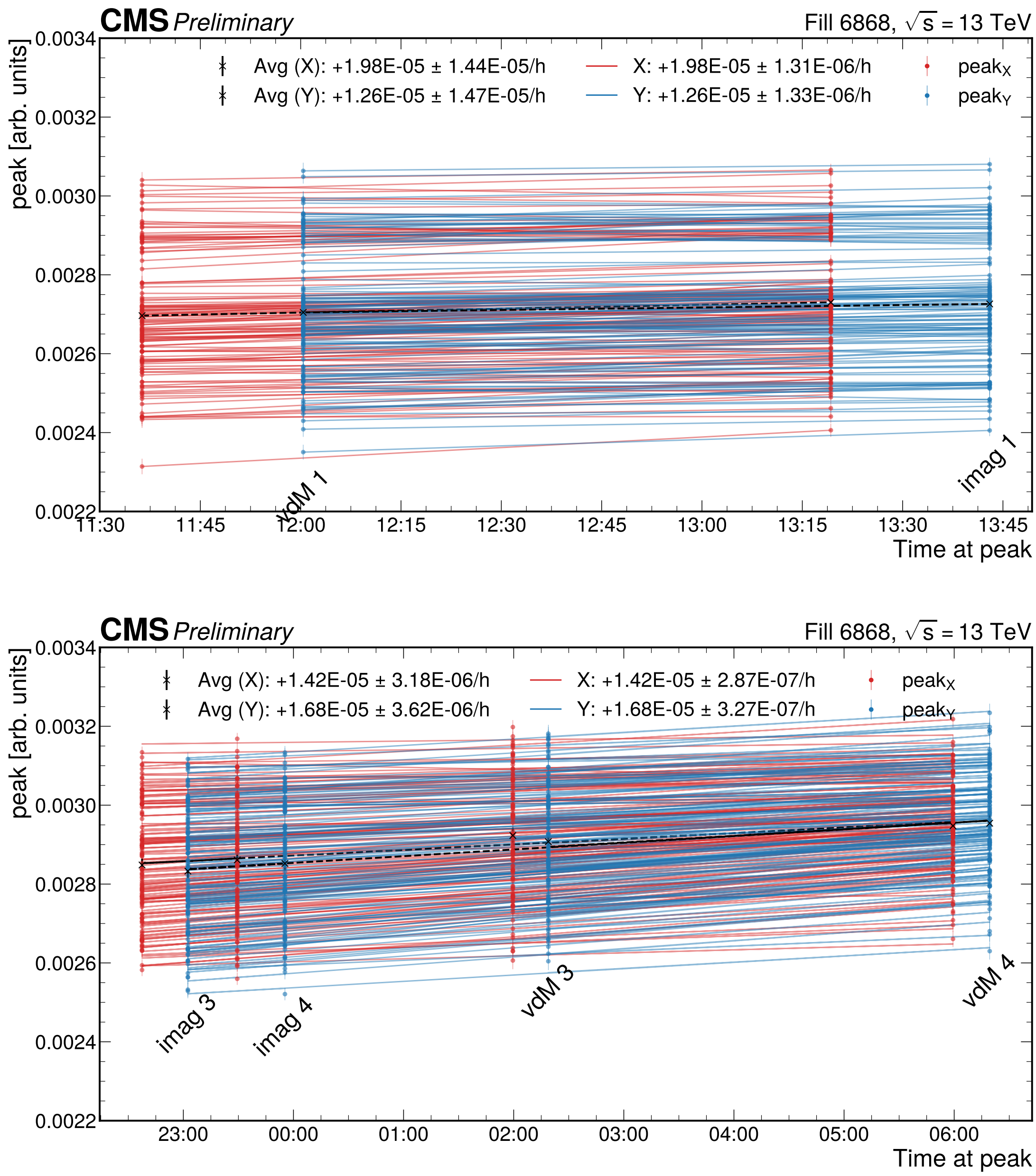

Figure B.12. *Time evolution of peak including linear fits, PLT luminometer, no corrections applied.*

APPENDIX C: EFFECT OF CONVOLUTED BEAM WIDTH TIME EVOLUTION TO VISIBLE CROSS SECTION, NO FRAMEWORK CORRECTIONS

Table C.1. *Visible cross section σ_{vis} determined using the vdM framework with no corrections ("original"), visible cross section obtained by propagating the convoluted beam widths Σ to the mid point between planes ("corrected"), systematical uncertainty in visible cross section caused by peak and Σ evolution discrepancy $\Delta_{\mathrm{x/y}}$, and the difference between the corrected and uncorrected visible cross sections.*

Luminometer	Scan	σ_{vis} [mb] original	$\Delta\sigma_{\mathrm{vis}}$ [%] original	σ_{vis} [mb] corrected	$\Delta\sigma_{\mathrm{vis}}$ [%] corrected	$\Delta_{\mathrm{x/y}}$ [%]	Difference in σ_{vis} [%]
HFET	imag1	2403.95	0.01	2401.96	0.01	0.17	0.05
HFET	vdM1	2386.20	0.01	2384.36	0.01	0.36	0.05
HFET	imag3	2422.56	0.01	2426.24	0.01	0.29	0.20
HFET	imag4	2400.10	0.01	2404.23	0.01	0.19	0.21
HFET	vdM2	2425.81	0.01	2429.85	0.01	0.22	0.21
HFET	vdM3	2416.15	0.01	2419.33	0.01	0.25	0.16
HFET	vdM4	2426.07	0.01	2429.61	0.01	0.29	0.16
HFOC	imag1	804.63	0.01	805.00	0.01	0.20	0.05
HFOC	vdM1	800.15	0.01	800.61	0.01	0.22	0.05
HFOC	imag3	797.15	0.01	798.80	0.01	0.45	0.21
HFOC	imag4	790.42	0.01	792.31	0.01	0.33	0.22
HFOC	vdM2	799.12	0.01	801.07	0.01	0.35	0.22
HFOC	vdM3	796.46	0.01	798.04	0.01	0.44	0.16
HFOC	vdM4	801.34	0.01	802.84	0.01	0.37	0.17
PLT	imag1	265.41	0.04	265.53	0.03	0.37	0.09
PLT	vdM1	263.48	0.04	263.66	0.03	0.53	0.09
PLT	imag3	263.38	0.03	264.02	0.02	0.51	0.21
PLT	imag4	260.76	0.03	261.52	0.02	0.47	0.22
PLT	vdM3	263.14	0.03	263.81	0.02	0.56	0.17
PLT	vdM4	264.44	0.03	265.05	0.02	0.49	0.17